DEVELOPMENT, EVALUATION AND OPTIMIZATION OF IMAGE BASED METHODS FOR MONITORING CRYSTALLIZATION PROCESSES

ZHOU YING

NATIONAL UNIVERSITY OF SINGAPORE

2011

DEVELOPMENT, EVALUATION AND OPTIMIZATION OF IMAGE BASED METHODS FOR MONITORING CRYSTALLIZATION PROCESSES

ZHOU YING

(M.Sc., National University of Singapore,

B.Eng., Dalian University of Technology, China)

A DISSERTATION SUBMITTED

FOR THE DEGREE OF DOCTOR OF PHILOSOPHY

DEPARTMENT OF CHEMICAL AND BIOMOLECULAR ENGINEERING

NATIONAL UNIVERSITY OF SINGAPORE

2011

Acknowledgements

I would like to dedicate this thesis to the memory of my father, Mr. Chuanfu Zhou. No words can express my great respect and reverence to him. I could never have begun this thesis without his endless love, unconditional support and unselfish consideration from his heart and soul.

I would like to express my sincere gratitude to my main supervisor, Prof. Rajagopalan Srinivasan, for his invaluable guidance, encouragement and patience throughout my project. He has offered me precious advice on how to face challenges and supported me to pass through the hardest time both in my work and life. He has spent time teaching me how to write proper research papers and patiently revised my drafts of papers over and over. The experience learnt from Prof. Raj has made me a more independent and confident researcher.

I am especially grateful to my co-supervisor Prof. Samavedham Lakshminarayanan, for his constant instruction, support, valuable comments and suggestions.

Deep appreciation also goes to Mr. Xuan-Tien Doan, Dr. Debasis Sarkar, Dr. Zaiqun Yu, Ms. Jia Wei Chew, Dr. Ann Chow, Dr. Shaohua Feng, Dr. Jie Bu, Ms. Angeline Seo, Ms. Agnes Nicole Phua Chiew Lian and other colleagues and lab-mates, for their efforts and assistance. It is a pleasant experience to work with

them together.

I would also like to acknowledge the National University of Singapore (NUS) for offering me the chance to pursue this degree, and gratefully acknowledge the Institute of Chemical and Engineering Sciences (ICES) for funding the project and providing me with the lab, experimental equipment and very good studying and working environment.

In particular, I would like to thank Rong Xu, Shoucang Shen, Zhan Wang, Feng Gao, David Wang, Shuyi Xie, Jin Xu, Yi Li, Liangfeng Guo, Kian Soon and many other close friends for sharing my joys and sadness, listening to my complaints, giving me advice, and having an unforgettable time together.

Last but not least, I would like to express my deepest gratitude to my family, my mother, Fuqin Liu, my brother, Wei Zhou, my husband, Donglin Shi and my daughter, Yuexin Shi for giving me persistent encouragement and support.

Zhou Ying

May 2011

Table of Contents

Summary

Monitoring and control of particulate processes is quite challenging and has evoked recent interest in the use of image-based approaches to estimate product quality (e.g. size, shape) in real-time and in situ. Crystal size estimation from video images, especially for high aspect-ratio systems, has received much attention. In spite of the increased research activity in this area, there is little or no work that demonstrates and quantifies the success of image analysis (IA) techniques to any reasonable degree. This is important because, although image analysis techniques are well developed, the quality of images from inline sensors is variable and often poor, leading to incorrect estimation of the process state. This thesis studies large-scale size estimation with Lasentec's in-process video imaging system, PVM. It seeks to fill this void by focusing on one key step in IA viz. segmentation. Using manual segmentation of particles as an independent measure of the particle size, we have devised metrics to compare the accuracy of automated segmentation during IA. These metrics provide a quantitative measure of the quality of results. A Monosodium Glutamate seeded cooling crystallization process is used to illustrate that, with proper settings, IA can be used to accurately track the size within ~8% error.

Any image processing algorithm involves a number of user-defined parameters and, typically, optimal values for these parameters are manually selected. Manual

selection of optimal image processing parameters may become complex, time-consuming and infeasible when there are a large number of images and particularly if these images are of varying quality, as could happen in batch crystallization processes. This thesis combines two optimization approaches to systematically locate optimal sets of image processing parameters – one approach is a model-based optimization approach used in conjunction with uniform experimental design; another approach is the sequential simplex optimization method. Our study shows that these two approaches or a combination of them can successfully locate the optimal sets of parameters and the image processing results obtained with these parameters are better than those obtained via manual tuning. Combination of these two approaches also helps to overcome the drawbacks of the two individual methods. Our work also demonstrates that the optimal sets of parameters obtained from one batch of process images can also be successfully applied to another batch of process images obtained from the same system. The in-process video microscopy (PVM) images that are acquired from Monosodium Glutamate (MSG) seeded cooling crystallization process are used to demonstrate the workability of the proposed approach.

List of Figures

List of Tables

List of Symbols

ALD: Axis Length Distribution

ATR-FTIR: Attenuated Total Reflectance Fourier Transform Infrared

B: Binary Image

CCD: Charge-Coupled Device

CLD: Chord Length Distribution

CLD_{Max}: Maximum chord length

CLD_{Min}: Minimum chord length

CMOS: Complementary Metal Oxide Semiconductor

CT: Computerized Tomography

DFT: Discrete Fourier Transform

DOE: Design of Experiments

FBF: Feature-Based Image Fusion

FBRM: Focused Beam Reflectance Measurement (FBRM)

FDA: US Food and Drug Administration

GP: Genetic Programming

IA: Image Analysis

MIA: Multivariate Image Analysis

MSG: Monosodium Glutamate

NIR: Near-Infrared

PAT: Process Analytical Technology

PIA: Particle Image Analysis

PSD: Particle Size distribution

PVM: In-Process Video Microscopy

RBF: Region-Based Image Fusion

S: Structuring Element (in morphology operation)

SSO: Sequential Simplex Search

UD: Uniform Design

$C(x,y)$: Canny edge detected image

C_i : concentration of solute i, [g/g or %]

C_i^* : equilibrium concentration of solute i, [g/g]

ΔC : concentration difference, [g/g]

C_R: contracted vertex to reflection side in SSO

C_W: contracted vertex to W side in SSO

$d(\ell_i, \ell_j)$: Euclidean distance between two pixels

E : cumulative error

E_i: expanded coordinate of the i^{th} parameter in SSO

E_G : median error of particle size estimation for one image

ER : ratio of M_A to E

$G(x,y)$: Gaussian filter mask

$I(x,y)$: original image

$\tilde{I}(x,y)$: enhanced image

$\tilde{\tilde{I}}(x,y)$: filtered image

$I_{\text{Ref}}(x,y)$: reference image

$I_{\max}$: maximum image intensity

$I_{\min}$: minimum image intensity

ΔI : image intensity range

ℓ_i : coordinates of the i^{th} outline pixel

M : Canny edge magnitude

M_A : extent of matching

N: the next-to-the-worst vertex

o : ordered coordinates (2-d) pixels of particle's outline

$\hat{o}$: centroid position calculated from particle's outline

$\|o\|$: maximum chord length calculated from particle's outline

P_i: centroid point of the i^{th} parameter in SSO

R_i: reflected coordinate of the i^{th} parameter in SSO

S: supersaturation ratio

S_i: step size in SSO

T_k: user-defined threshold value for image intensity range

$T_{\min}$: user-defined threshold value for minimum image intensity

$v_{i,j}$: value of i^{th} parameter in j^{th} vertex

W: the worst vertex in SSO

X_i: initial guess of the i^{th} parameter in SSO

$(\hat{X}, \hat{Y})$: coordinate position of object in image

(r_i, θ_i): signature curve of object's outline

σ: standard deviation of the Gaussian smoothing filter

ϕ: Canny edge direction

δ: user-defined threshold value to identify same particle from different segmentation

ε_p: error in particle's length estimation

Chapter 1. Introduction

Crystallization is a critical process in pharmaceutical, fine chemical, petrochemical, food, and semiconductor manufacturing industries. In crystallization operations (Myerson, 2002; Quirk & Serda, 2002; Yu & MacGregor, 2003), particle size and shape are important specifications of product quality that need to be well-controlled. For a pharmaceutical product, the dissolution rate, bioavailability and therapeutic effects depends significantly on the particle size and shape. A narrow particle size distribution with specific particle shape is often indicative of good product quality.

Real-time monitoring and control of the crystallization process is important to ensure that the desired final product quality is achieved. Traditionally, the control of crystallization processes has relied extensively on empirical experience. Complex chemistries, non-availability of detailed models, and the lack of in situ sensors to directly measure product quality have been the main reasons for this state of affairs. The lack of in situ sensors is felt in other particulate processes such as filtration, drying and granulation as well. Although technologies for offline particle size and shape measurements such as microscopy have been available and widely used, it is but recently that in-line measurements are

becoming possible. Technologies such as Focused Beam Reflectance Measurement (FBRM) and In-Process Video Microscopy (PVM), both from Lasentec / Mettler Toledo, are widely used in manufacturing units to monitor particle size distribution and shape variation. With the advances in real-time imaging hardware and the concomitant developments in image analysis technology, there is an opportunity to monitor crystallization processes by processing in-situ images.

Section 1.1 will discuss the challenges in processing in-situ images. Our main contributions will be summarized in Section1.2. The thesis structure will be introduced in Section 1.3.

1.1 Challenges in In-Line Imaging for Crystallization

The numerous benefits of extracting product, process, and phenomena characteristics from in-situ images are conditional on accurate assessment of the particle size and shape from the images. Although, the various steps of image analysis are well-established and have been used in several crystallization systems, it is widely acknowledged (Patience et al. 2001; Braatz, 2002; Larsen et al. 2006a) that the extraction of information from in-situ images remains a challenging task for several reasons:

- The in-process video offers a 2-d image of 3-d objects with the consequent loss of information.

- Unlike the images used in classical image analysis literature where the objects of interest change slowly, crystallization involves stirred solutions, and particles move at high speeds (vis-à-vis the field of view and the imaging rate). As a corollary, even with tens of images per second, the same particle cannot be guaranteed to be present in contiguous images. This precludes noise cancellation by averaging across samples (images). Further, the usual complications in capturing images of objects in motion occur including random orientations, and out-of-focus objects.

- In situations where classical image analysis is widely applied, the 'background' can be considered stationary in space and time with respect to the objects of interest. In crystallization systems, the background is a stirred solution – therefore, images suffer from various aberrations such as background noise, bubbles, time-changing intensity and contrast, etc.

- Currently, there is no image processing algorithm that can perform well under varying image qualities. The algorithms have been largely customized to specific applications – both the specific image processing steps and their

parameters would need adjustment for a given crystallization system. Even within one system, there may be significant intra-run variability in the background and the quality of images. This makes it difficult to apply any one method or one set parameters to process all the images from different process stages. During a batch crystallization run, the solid concentration typically increases as the crystals nucleate and grow. The imaging system thus acquires blank images (of the background) at the beginning, and images with many overlapping crystals in a high solid-concentration background towards the later stages. As the run proceeds, the contrast of the images varies with time and the capability to extract information reliably from the images deteriorates considerably. As an additional complication, at high solid-concentrations, the crystals may aggregate or agglomerate, making accurate particle segmentation even more challenging.

- Finally, to effectively track the process in real-time, the image-processing algorithm must not only be accurate and robust, but also capable of matching the speed at which images are acquired. The current rate of image acquisition is up to 30 images/second for charge-coupled device **(**CCD) camera and 10 images/second for PVM.

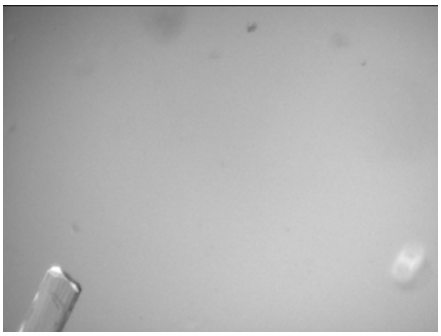

(a) Partially imaged particle

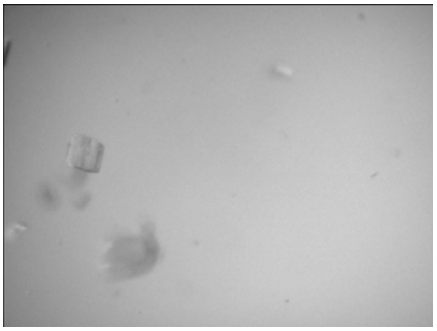

(b) Out of focus particle

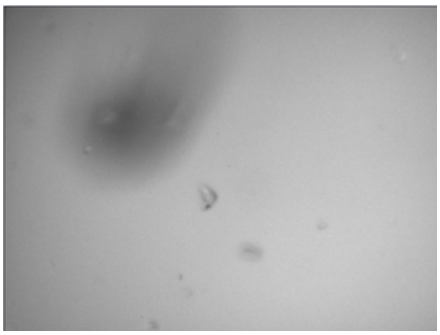

(c) Uneven background

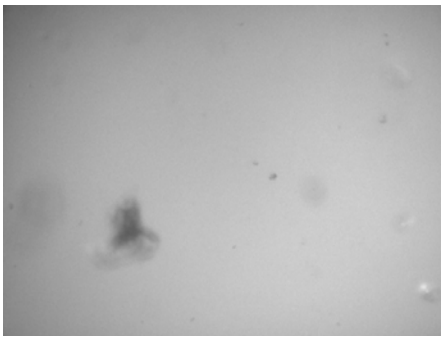

(d) Particle not clearly imaged

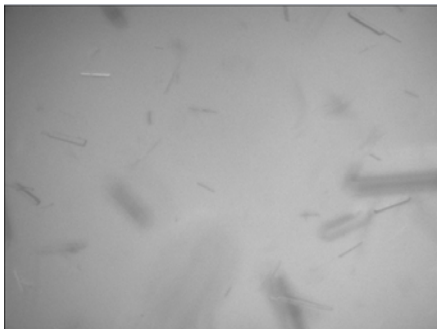

(e) Far-away big particles are imaged as small ones

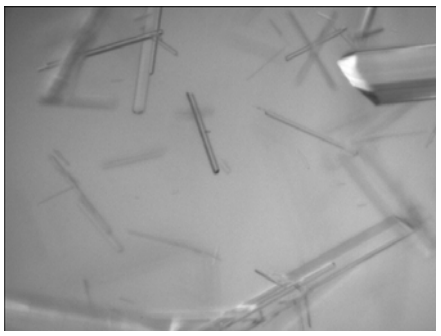

(f) Long particles overlap and partially imaged

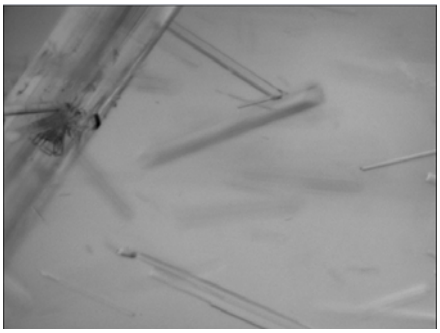

(g) Uneven background and out of focus particles

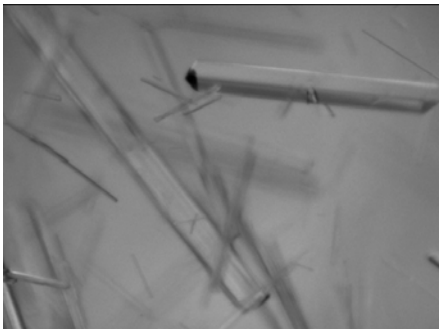

(h) High aggregation of long particles

Figure 1.1. Problems with in-line imaging system.

Fig. 1.1 demonstrates the common problems that may be encountered with in-line imaging systems. Since the lens has limited field of view, long particles should be at the center of the image to be fully imaged. The longer a particle grows, the higher the possibility that the particle would only be partially imaged. Fig. 1.1(a), (f) and (h) show partially imaged particles. Random imaging of moving particles in a stirred slurry may also cause further problems of unclearly imaged particles (Fig. 1.1 (b) and (d)), uneven background (Fig. 1.1 (c)) and far away big particles may be imaged as small particles (Fig. 1.1 (e)). With the progress of crystallization process, more and more particles nucleate and grow bigger. Consequently, the solid concentration increases and particles aggregate, as shown in Fig. 1.1 (f), (g) and (h). With these common problems, it is not easy to precisely segment particles and characterize particle size and shape from in-line process images. Because of these challenges, it is important develop specific improvements targeted at PVM images.

1.2 Objectives and Main Contributions

Direct observation is now believed to be the best way to monitor particle shape and size (Yu et al., 2004). Process images can provide more realistic two-dimensional information on particle shape and size and help us better understand the process (Scott, 2005; Scott & McCann, 2005; Li et al., 2006). However, there is still a gap between the information obtained from advanced

imaging sensors and the knowledge required for in-line monitoring of crystallization process. In this thesis, we aim to circumvent these challenges by using in-process video imaging (PVM in particular) for determining particle shape and size distribution for the purpose of process monitoring. Three main contributions will be presented in this thesis.

1) We develop an image analysis (IA) methodology to automatically extract the maximum possible information from in situ digital PVM images, and apply it to a Monosodium Glutamate (MSG) seeded cooling crystallization processes to monitor particle shape and size distribution in-line.

2) To study the accuracy of PVM imaging system and IA methodology, we evaluate the PVM imaging system with off-line microscopy measurements and evaluate the IA methodology with manual image segmentation. Two experiments are studied for comprehensive evaluations. The first experiment, five sets of sea sand in DI water, involves no variation of particle size and shape during the process time. The second experiment involves particle growth with process time during a seeded batch cooling crystallization of MSG,.

3) Instead of manually tuning the complex combinations of IA parameters, optimization methods are developed to automatically locate their optimal

values. The developed optimization methods integrate model-based optimization with simplex search optimization. It is possible to locate all possible optimal IA parameters in the entire parameters' space. The obtained optimal IA parameters are robust not only to the images acquired from the same batch of process, but also to the images acquired from other batches.

1.3 Thesis Structure

The rest of the thesis is organized as follows: Chapter 2 introduces the important specification of product quality in crystallization process, summarizes current in-situ instruments for crystallization process monitoring and control, and reviews the current state of the image-based techniques. In Chapter 3, our proposed IA methodology is described in detail. Chapter 4 demonstrates the experimental setup and the detailed experimental procedures. In Chapter 5, the metrics for evaluating PVM imaging system and IA methodology are introduced, and evaluated with sea sand images by microscopy measurement and manual image segmentation. In Chapter 6, the developed IA methodology is validated and applied to MSG seeded cooling crystallization process to monitor particle growth in real-time. Chapter 7 demonstrates an optimization method to automatically locate optimal IA parameters. Finally, conclusions and future work are discussed in Chapter 8.

Chapter 2. Real-Time Monitoring and Control of Crystallization Processes

Monitoring and control of particle shape and size distribution in real-time is a challenge faced by the traditional pharmaceuticals and fine chemicals industries. This is due to the lack of sufficient process knowledge and in-situ sensors. With regulatory initiatives such as the US Food and Drug Administration's (FDA) Process Analytical Technology (PAT) program for the pharmaceutical industry and the ongoing improvements in real-time imaging hardware (exemplified by FBRM and PVM, both from Lasentec) concomitant with the developments of image analysis techniques, there is a fast growing interest in the pharmaceutical and chemical industries as well as the research community to develop advanced in-line control technologies for particulate processes using advanced imaging equipments.

A number of studies (Yu et al., 2004; Birch et al., 2005; Barrett et al., 2005; Calderon De Anda et al., 2005a, 2005b, 2005c; Larsen et al., 2006a, 2006b, 2007, 2009; Li et al., 2006, 2008; Ma et al., 2007; Patience et al., 2001, 2002; Qu et al., 2006; Sarkar et al., 2009; Simon et al., 2009a, 2009b, 2010a; Wan et al., 2009;

Wang, 2006; Wang et al., 2007, 2008; Zhou et al., 2007, 2009) have highlighted the success of implementing of such imaging sensors to gain insights into the crystallization process thereby providing extra capability for in-line process control.

Section 2.1 introduces the important specifications of product quality in crystallization processes, including the basic concepts and the factors affecting the formation of crystals. Section 2.2 reviews current in-situ sensors and corresponding measurements that facilitate the monitoring and control of crystallization processes. Section 2.3 introduces the concept of process imaging and reviews the available processing technologies in characterizing particle size and shape. Section 2.4 summarizes the major image analysis steps. Conclusions will be given in Section 2.5.

2.1 Important Specifications of Product Quality in Crystallization Processes

Particle size, shape and size distribution are the main indicators of product quality in crystallization processes. Usually, a relatively big particle size, a narrow particle size distribution and a specific particle shape are specified as targets of product quality in crystallization operations. If the product has a small mean particle size, it can cause problems in further downstream processing, such as

centrifuging, washing and packaging. A broad particle size distribution is generally not desired because it will lead to different dissolution times thereby affecting their subsequent usage (e.g. medical applications). Particle shape can significantly affect physical and chemical properties of powder material, such as fluidity, solubility and the electromagnetic characteristics.

In early stages of drug development, it is important to characterize the API crystals of pharmaceutical powders, so as to ensure that the particles in powder materials have expected function. It is also critical to monitor the crystallization process to ensure that the produced particles can meet the specified requirements on particle size and shape.

2.1.1 Important Specifications for Crystallization Process

Crystallization is a phase change process. It involves the generation and growth of crystals from liquid solutions. Hence, the important specifications of crystallization include the solubility of solute, supersaturation, nucleation, growth and polymorphs of crystals. The details of these important specifications will be introduced below.

Solubility and Supersaturation

At a given temperature, *solubility,* also called *equilibrium concentration* or

saturation concentration, is defined as the maximum amount of solute dissolved in a given amount of solvent. This makes the solution saturated. The variation of solubility with temperature determines the particle yield. For a given species i, when the solute concentration c_i is less than, equal to, or greater than the equilibrium concentration, c_i^*, the system could be defined as *undersaturated*, *saturated*, or *supersaturated* respectively.

Supersaturation, S, is the thermodynamic driving force of crystallization and is the necessary condition for the occurrence of crystallization. Supersaturation is defined as the amount of solute concentration exceeding the saturation concentration. Several expressions for supersaturation exist in the literature and some are provided in Eq. (2.1) to (2.3).

- Concentration driving force:

$$\Delta C = C_i - C_i^* \tag{2.1}$$

- Supersaturation Ratio:

$$S = \frac{C_i}{C_i^*} \tag{2.2}$$

- Dimensionless concentration difference

$$\sigma = \frac{C_i - C_i^*}{C_i^*} = S - 1 \tag{2.3}$$

Crystal Nucleation and Growth

A supersaturated solution is not at equilibrium state. In order to move it toward

equilibrium, the solute molecules will be transferred from liquid phase to solid phase in the form of crystals. This is indicated as *nucleation*, a phase separation step in which new crystals are formed.

Supersaturation is necessary for nucleation. However, supersaturating certain amount of solute into the saturated solution will not necessarily cause nucleation, because nucleation needs extra molecules to form a critical sized cluster (Myerson, 2002). This supersaturated state is *metastable*. The maximum amount of solute that can be supersaturated into the solution without triggering the instantaneous nucleation is called *metastable limit*, or *spinodal cruve*. The zone between the solubility curve and metastable limit is indicated as *metastable zone*. Traditionally industrial crystallizations are carried out within this zone.

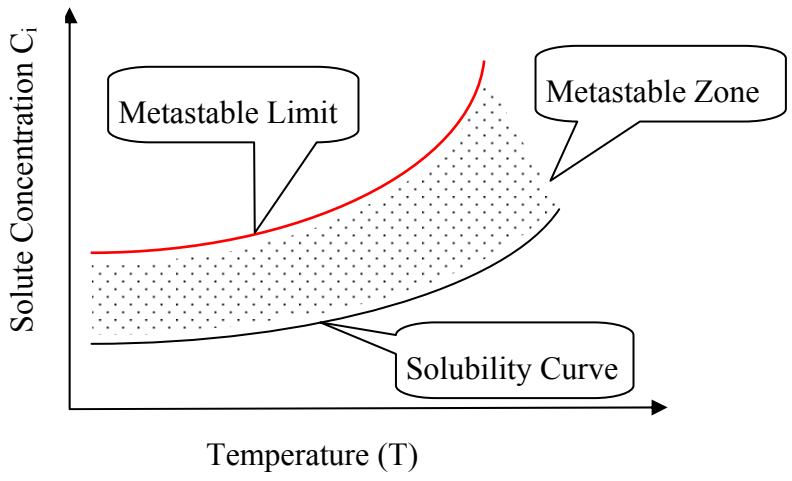

Figure 2.1. Definition of metastable zone.

Fig. 2.1 demonstrates the relationships between metastable limit, metastable zone

and solubility curve. When the solution concentration is above metastable limit, the spontaneous nucleation that occurs is defined as *primary nucleation*. Primary nucleation is unstable and hard to control - so it is often avoided. Adding a small amount of parent crystals, such as seeds, into the supersaturated solution will decrease the supersaturation needed for nucleation. This kind of nucleation is termed as *secondary nucleation*.

Primary nucleation generates the smallest sized crystals. Subsequently, the solute molecules will be transported from supersaturated solution to these nuclei and crystal growth occurs in 3 dimensions with repeating periodic structure, (this step is defined as *crystal growth*). With different conditions, crystals could grow at different rates with different crystal habits. Crystal nucleation and growth occur simultaneously in crystallization process, the relation between the degree of nucleation and growth rate will determine the particle size and size distribution.

Polymorphs

Pharmaceutical powders usually exist as crystalline or amorphous solids forms. In a crystalline pharmaceutical powder, the structural units are repeated in a regular order, a well-defined three dimensional structure, which is also known as crystal lattice. An amorphous pharmaceutical powder does not have such obvious crystal lattice.

A crystalline powder can have more than one possible crystal structure. This phenomenon is known as polymorphism. The same substance with different crystal structure is termed as polymorphs (Myerson, 2002), which are represented as different physical and chemical properties. Typically, only one polymorph can be stable at a certain temperature and pressure. Hence, the most thermodynamically stable form is chosen as the final dosage form (Bugay, 2001). The polymorphs of a pharmaceutical powder have the identical chemical nature but their physical properties, such as morphology (or shape), color, density, heat capacity, melting point, thermal conductivity, optical activity etc., can vary from one polymorph to another (Myerson, 2002). These differences are commonly caused by the difference in the crystal lattice. The polymorphs also affect pharmaceutical properties, such as stability, dissolution, and bioavailability (Haleblian & McCrone, 1969).

2.1.2 Factors Affecting Crystallization Process

Crystallization is a complex process. In addition to the nucleation and growth steps, crystal agglomeration and breakage may also occur. *Agglomeration* occurs when two or more particulates collide and aggregate into a big particle. Usually, three steps are involved in agglomeration: (i) collision of particles, (ii) adhesion, and (3) solidification of agglomerate. Agglomeration does not contribute to the phase transfer from liquid to solid, but it distorts the shape of PSD. *Breakage*

occurs when a big single crystal or agglomerate is broken down into many smaller fragments. Breakage can also be considered as a type of secondary nucleation. Both the agglomeration and breakage can affect particle size and size distribution, thereby affecting product usage its properties.

Selecting a correct solvent is very important, since solvent can thermodynamically and kinetically affect the nucleation and growth of crystals. For example, the solubility and metastable zone of a solute may vary a lot in different solvents. This will lead to different crystallization conditions for different solutions and may result in crystals with different shapes and qualities.

A small amount of impurity could dramatically influence crystal growth, morphology and nucleation, and result in products that are quite different from those obtained from pure solvents. Both the solvent and impurity effects on crystallization can be explained in terms of intermolecular interactions. For example, the solubility of solute varies with different solvent system. That is because the collision frequency among solute molecules necessary to form molecular clusters changes with solvents, which is caused by the changes in diffusivity of solute and solid-liquid interfacial tension.

Furthermore, operating conditions such as the cooling rate, temperature profile, agitation speed of the stirrer, size of seeds, seeding time and vessel scale have an

influence on the crystallization process and lead to variability in the product quality.

2.2 Current In situ Instruments for Crystallization Process Monitoring and Control

The FDA's PAT initially brings in the application of new and efficient engineering expertise into the pharmaceutical industry. To ensure the optimal process state and desired product quality, a few typical in situ PAT instruments for crystallization process would be reviewed here. Attenuated Total Reflectance Fourier Transform Infrared (ATR-FTIR) is used for measuring solution concentration and supersaturation; FBRM measures particle chord length and chord length distribution (CLD); Raman and near-infrared spectroscopy (NIR) are applied to identify particle polymorphs; In-process video imaging system together with specific image processing techniques can be used to characterize particle size and shape.

2.2.1 Attenuated Total Reflectance Fourier Transform Infrared Spectroscopy

ATR-FTIR has been widely applied for in situ measurement of supersaturation, solubility and metastable zone in all kinds of crystallization processes (Lewiner et

al., 2001; Togkalidou et al., 2002; Fujiwara et al., 2002; Liotta & Sabesan, 2004; Pollanen et al., 2005; Yu et al., 2006a , 2006b; Alatalo et al., 2008; Borissova et al., 2009; Chen et al., 2009). These studies demonstrated that ATR-FTIR could be successfully applied for in situ measurement of the solute concentration in solutions with solid particles present.

An ATR-FTIR probe is shown in Fig 2.2. It could be directly inserted into crystallizer. A specific ATR crystal (ZnSe) is fixed at the tip of the probe and is in contact with the slurry in crystallization. FTIR generates a laser beam and directs it to ATR crystal. Part of this laser beam is reflected while the other part propagates into the liquid solution and is absorbed.

Figure 2.2. Photo of ATR probe.

The frequencies of absorbed infrared light indicate the chemical species that are detected in the solution and the corresponding absorption magnitude shows the concentration of each species. Since different compounds in the solution will have

different frequencies of absorption, the collected spectra can be correlated with the solution concentration of more than one compound. Once the collected spectra are calibrated with known composition of multi-component mixture using chemometrics, it is possible to estimate the concentration of each composition in situ.

In situ measurement of the concentration of each composition in a multi-component mixture and the insensitivity of measurements to the presence of solid particles are the main advantages of ATR-FTIR over other concentration measurement techniques. It is a suitable PAT instrument for monitoring and control of multiple solute concentrations in crystallization processes.

2.2.2 Focused Beam Reflectance Measurement (FBRM)

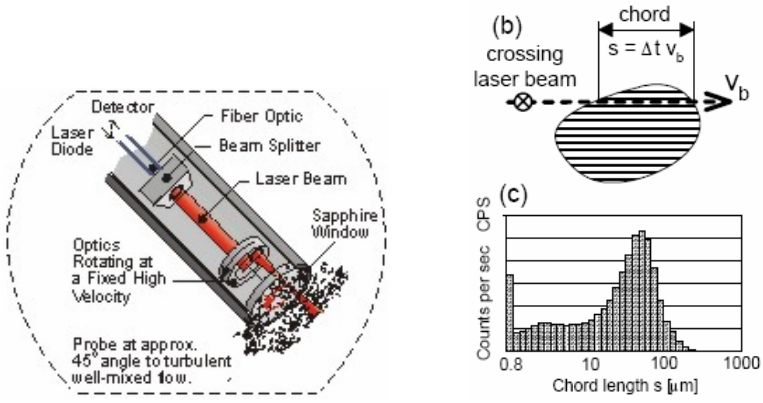

Figure 2.3 Structure diagram of FBRM.

FBRM is a popular in-line instrument to monitor particle size distribution in

current pharmaceutical manufacturing. As shown in Fig. 2.3, the principle of FBRM is that an infrared laser beam rotated at high-speed is reflected back when it hits a particle. The particle size is calculated based on the rotation speed of the laser beam as well as the time taken by the beam to pass through the particle. The measured particle size is termed as chord length.

Using the measured number of particles and chord length distribution, different weighting is applied to get an estimate of the actual particle size. The weighting given to each channel emphasizes the changes in one region of the distribution while de-emphasizing changes in another part of the distribution at the same time. This is done by applying a channel-specific weight, w_i to count, n_i. The weighted channel count, y_i are obtained by

$$y_i = w_i n_i \quad \text{for channels } i = 1, 2, \ldots, N \tag{2.4}$$

The weight w_i is obtained from channel midpoint M_i by

$$w_i = \frac{M_i^{\gamma}}{\sum_{j=1}^{N} M_j^{\gamma}} \cdot N \quad \text{for channels } i = 1, 2, \ldots, N \tag{2.5}$$

Different types of channel weights can be determined by varying γ as given in Table 2.1:

Table 2.1 : Parameters for Various Weights of FBRM Measurements

Method	γ
1/Length Weight	-1
No Weighting	0
Length Weight	1
Square Weight	2
Cube Weight	3

FBRM has the advantage that its sensor probe can be inserted directly into the solution without the need for sampling lines. It can be used in high temperature, high pressure and high solid concentration situations (Ruf, Worlitschek & Mazzotti, 2000). The measured chord length and chord length distribution are reliable and permits the user to track the trends as the crystals evolve. However, the measured CLD is not the actual particle size distribution (PSD), since the rotated laser beam of FBRM may randomly hit any portion of a particle and pass through it in any angle. The one-dimensional measurement is just a chord length across any two edge points – in the general case, it does not connect directly to geometrical shape descriptors such as the length or width of the particle. Furthermore, FBRM does not indicate the particle shape, and thus cannot fully represent the two- or there-dimensional particle size information, especially when the particles are non-spherical.

As mentioned above, FBRM measurements cannot reflect the actual PSD. Some researchers (Heath *et al*., 2002) try to restore the PSD from CLD. Empirical methods assign different chord weightings to different ranges of particle size, while analytical methods usually assume the particles to be of spherical shape or ellipsoid shape (Hukkanen & Braatz, 2003). A mathematical model is built to correlate CLD and PSD (Worlitschek, 2003) and numerical methods have to be applied to correlate the CLD and PSD for highly non-isotropic particles (e.g. octahedral-shaped or needle-shaped particles). Some researchers have also proposed correcting to the correlation by considering the effect of particle orientation (Nere *et. al,* 2007). Limiting particle size to specific ranges for selecting good values of weighting parameters is not applicable, especially when dealing with long needle shaped particles and when the CLD is quite broad. Generating some common theoretical models is also not generally applicable due to the complexity of crystallization processes. The three-dimensional crystals in different molecular structures and shapes make it difficult to fully recover 3-dimensional information from the one-dimensional FBRM data. Even if it is reasonable, crystal growth, polymorph transitions, particle breakage and agglomeration may occur at the same time in the crystallization process. This means that single particles in different symmetric shapes and particle clots in irregular shapes may coexist in the solution. Since FBRM cannot recognize the shape of particles or particle clots, it is hard to control the process of particle growth, polymorph transition or prevent particle aggregation.

2.2.3 Raman and Near-Infrared Spectroscopy

Both Raman and near-infrared (NIR) are able to characterize the structure of crystals in-situ at the early stage of drug development. They enable the monitoring and control of crystal polymorphs, thereby ensuring that the required form of product is produced.

NIR spectroscopy detects the light absorption of near-infrared region by vibrating the molecules. It is conducted in reflectance mode to measure the chemical information of solid samples. NIR spectroscopy is sensitive to crystal lattice and the changes in hydrogen band, which allows them to be used to analyse solid pharmaceutical powders. They can identify (Aldridge et al., 1996) and quantify the polymorphs (Stephenson et al., 2001; Luner et al., 2000), as well as determine the crystallinity (Hogan & Buckton, 2001) .

Raman Spectroscopy detects the frequency shifts of scattered light. Frequency shift means the frequency differences between the scattered light and the incident beam. Raman spectroscopy can detect the symmetric vibration modes and has been applied to distinguish the forms of pharmaceutical powders (Langkilde et al., 1997; Findlay & Bugay, 1998; Campbell Roberts et al., 2002; Al-Zoubi et al., 2002; Moynihan & O'Hare, 2002; Franco et al., 2003, Morel & Adar, 2005), quantify polymorphs (Pratiwi et al., 2002; Pelletier, 2003), and in situ monitoring of polymorphic transitions (Starbuck et al., 2002; O'Brien et al., 2005; Ono et

al., 2004; Wikstrom et al., 2005; Ramtanen et al., 2005). Raman imaging also be used to detect the API distribution of a tablet (Webster & Baldwin, 2005a, 2005b; Sasic et al., 2005).

The major advantages of Raman spectroscopy can be listed as below (Bugay, 2001; Findlay & Bugay, 1998; Al-Zoubi et al., 2002; Pelletier, 2003; Murphy et al., 2005; Adar et al., 2004; Vehring, 2005; Wall et al., 2005; Yu et al., 2004):

1) When low power is selected, Raman spectroscopy is non-destructive. It will not destroy or affect the sample during measurements. However, high power Raman Spectroscopy measurement will burn the samples.
2) Raman spectroscopy only requires simple sample preparation and can directly measure gas, liquid and solid samples through plastic or glass packages.
3) Raman spectroscopy is not affected by water and it can directly measure the aqueous suspensions.
4) Raman spectroscopy can be used as in-line and non-invasive measurements if it is coupled with fiber optic probes.
5) Raman spectrum can provide sharp features and contains a large amount of chemical information. This enables it to identify the constituents of complex mixtures and leads to the understanding of the process at a molecular level.
6) The samples can be as small as individual particles with a mass of only a

few nanograms.

Both Raman and NIR spectroscopy measure the vibrational mode, but Raman measures the changes in polarizability while NIR measures the changes in dipole moment. In general, Raman measures the symmetric vibration while NIR mainly measures the asymmetric vibration. Furthermore, Raman can measure the sample of aqueous suspension while NIR can detect an extremely large feature of water (Webster & Baldwin, 2005a, 2005b).

2.2.4 Real-Time Imaging System for Crystallization

In industry, most of the commercially available imaging sensors, such as the QICPIC Particle Size and Shape Analysis System from Sympatec, the Malvern Morphologi G3-ID Particle Characterization with Raman Chemical ID, and the Particle Shape & Size Analyzers from Occhio, are for off-line or on-line characterization of particle size and shape. These systems usually require preparation of samples or dispersion of the samples. There is a need to develop real-time on-line or in-line imaging systems.

Four types of imaging systems have been reported in literature: (i) on-line microscope imaging system, (ii) non-invasive in-line imaging system, (iii) invasive in-line imaging system, and (iv) on-line imaging system for 3-D particle size measurements.

On-line Microscope Imaging System

Microscope is a common instrument for process imaging which can be used not only in an offline fashion, but also in an online mode as well through a suitable sampling scheme (Patience, 2002; Patience & Rawlings, 2001),. The sampled solution from the crystallizer is placed in front of the lens of a microscope through which it is imaged. In this arrangement, the solution is not in continuous flow, but is stationary when photographed. Thus, the images are clear and can be processed automatically using image analysis software to identify particle size and shape for the purpose of on-line monitoring and control. However, several important questions arise when the on-line sampling scheme, which forms the bedrock of this stop-flow microscopy, has to be deployed in large-scale real-life settings: (i) does the sampled solution accurately represent the current process state? (ii) does the sampled solution affect the process when it flows back to the crystallizer? and (iii) does sampling aggravate the time delay associated with state identification? For these reasons, in situ measurements are now preferred and is the focus of this work.

In-situ and high speed are the common requirements for video microscopy of real-time imaging systems. In the literature, two other types of real-time video microscopy have been reported for in-line imaging of crystallization processes: non-invasive and invasive.

Non-Invasive In-Line Imaging System

High-speed CCD camera based non-invasive video microscopy is usually operated in synchrony with a strobe light source and fixed to an observation window on the external wall of crystallizer. Scientists at the pharmaceutical manufacturer GSK developed a special-purpose, non-invasive video imaging system for interrogating pharmaceutical crystallization (Wilkinson et al., 2000). An imaging system that includes a high-speed Sony XC55 CCD camera, a stroboscopic light source and video acquisition PC is used to monitor crystallization processes inside a glass reactor. In this setup, the camera is positioned perpendicular to the jacketed glass reactor and focused to its inner wall. A flat glass plate is attached between the camera and the outer wall of reactor to correct the distortion caused by the curved wall of the reactor. Roberts, Wang and coworkers have applied this kind of video microscopy to the crystallization of (L)-glutamic acid. They studied the polymorphic transformation (Calderon De Anda, et al., 2005a, 2005b), multi-dimensional growth rates (Ma et al., 2007; Wang et al., 2007), and also performed modeling and control of particle shape (Li et al., 2006; Wang et al., 2008; Wan et al, 2009). Rawlings and coworkers have also employed the GSK video microscopy to characterize the particle size distribution (PSD) of rod-like crystals in pharmaceutical crystallization (Larsen et. al., 2006a, 2006b, 2007, 2009). Simon et al. (2009b, 2010a) introduced another kind of bulk video imaging method, which is based on Sony video camera and Pinnacle TV capture card, to detect nucleation and to

identify the width of the metastable zone for the batch cooling suspension crystallization of the model pharmaceutical compound caffeine. They have also applied it to the highly viscous crystallization from melt of palm oil. In these studies, the non-invasive in-situ video microscopy could acquire process images at a speed of up to thirty images per second. The typical pixel resolution is 480 x 640 with a broad field of view from 140μm to 16mm. The advantage of non-invasive type video microscopy is that there is no problem related to sensor fouling and contamination. However, the shortcomings of this kind of imaging system are obvious. Since the camera is installed at the external wall of the jacketed reactor, an imaging window and a strobe light source are required to balance the convexity effect of crystallizer wall and to provide enough illumination respectively. This imaging setup requires high transparency of both bath fluids and the walls of crystallizer. The sampling is always in a fixed position of the crystallizer. These shortcomings limit its usage, especially for most of the cooling crystallization processes at low temperature where the condensate on the crystallizer wall will certainly worsen the image quality.

Invasive In-Line Imaging System

An invasive probe type design overcomes these shortcomings. It can be directly inserted into the solution, does not require any sampling, and so does not have the problems associated with microscope imaging. With a built-in illumination system, the probe can be inserted into any position inside the crystallizer,

permitting the monitoring of any location inside the vessel. Furthermore, it does not have strict requirements for the transparency of solution and bath fluids. Lasentec provides such an in situ camera for In-process video microscopy, called the PVM (shown in Fig. 2.4). PVM can be directly inserted into the solution to take real-time process images at a speed of up to 10 images/second. In a PVM system, six independent laser sources illuminate a fixed area and the light scattered back to the probe produces an image with the embedded CCD elements. The latest model of PVM (V819) has 1075μm x 825μm field of view of, with a resolution of 2μm. The PVM probe is now longer and slimmer (about 400mm in length and 19mm in diameter), which allows it to be more flexible to be inserted into vessels. PVM can be operated at pressures from vacuum to 150psi, and temperatures from -80^{o}C to +120^{o}C.

Figure 2.4. Structure of PVM System.

In a PVM system, the probe is connected to the control computer which also houses the control software. This makes it easy to store the captured images. No extra illumination equipment is needed since the probe contains six adjustable

laser diodes. Because of this probe design, issues such as on-line sampling and transparency of crystallizer wall are not significant. Barrett and Glennon (2002) describe the use of PVM to measure the meta-stable zone of a compound with human observation and decision making being an integral part of the operation. PVM is commonly used to monitor the process variables (Scholl et al., 2006a, 2006b) and qualitatively infer the process state. In this thesis, the reliability of in-line PVM measurement has been validated with off-line microscope measurements, and successful application to on-line monitoring of MSG seeded batch cooling crystallization has been demonstrated.

Qu et al. (2006) have applied another type of invasive in-line imaging system, named particle image analysis (PIA) 400 LUT video microscope, to analyse the effect of two potassium salt additives on the batch cooling crystallization of potassium dihydrogen phosphate. PIA is probe type that can be directly inserted into a crystallizer, but requires an extra tube to fix its sensor head. This means two tubes need to be inserted together into crystallizer, one tube is for sensor and another tube is to fix the sensor head. Thus, PIA requires more space inside the crystallizer as well as at its opening, which makes it especially difficult for experimental setups involving small scale crystallizers.

Another invasive probe type video microscopy is the *in situ* particle viewer (Li et al., 2008). This probe is 1.8m long and is suitable for large scale crystallizers. It

has a fixed field of view (about 8mm x 6mm) with a resolution of 40μm. This particle viewer has the similar design as PIA and it needs an extra tube to fix its sensor head and stroboscopic light source. This increases the probe dimension to 50mm x 30mm. It has been effectively applied to a 20-L batch crystallizer to characterize the polymorphic phase transformation processes of L-glutamic acid. Simon et al. (2009a) applied endoscopy as an in-situ probe for bulk video imaging to identify the metastable zone of potash alum hydrate in a small scale calorimeter.

All these studies demonstrated that invasive probe type in-situ video microscopy can help to monitor the crystal size and shape during crystallization. It can be installed even on sealed and covered reactors. The probe type is easy to install and has the flexibility to be inserted into different positions inside the crystallizer. Applying multiple probe-type in-situ video microscopes to one crystallization process will help to fully understand the process state, such as the mixing state. The obvious drawback of the invasive type video sensors is sensor fouling and contamination. In addition, it may require special opening and sealing for certain processes, where high pressure reactions or volatile chemicals are involved.

On-Line Imaging Systems for 3-D Particle Size Measurements

Irrespective of whether non-invasive or invasive in-situ video microscopy is applied, the above mentioned studies characterized particles from 2-D process

images from which it is hard to obtain reliable 3-D particle size. However, several studies presented recently have successfully characterized 3-D particle size and shape. Bujak and Bottlinger (2008) reconstructed 3-D particle shape of free-falling particles by simultaneously taking three images from three orthogonal directions. In their experimental setup, the 3 CCD-cameras and 3 light sources had to be precisely placed at certain positions. The particles freely fall between cameras and light sources and the projection of a particle could be registered by image capture in diffuse illumination. Similarly, Kempkes et al. (2010) tried to reconstruct the 3-D shape of particles in a suspension passing through flow channel. In this work, they did not apply multiple cameras for multiple images of the same particles. Instead, they arranged two mirrors at specific positions, so that the camera can take photos from the two mirrors at the same time. Thus, an image that shows a particle from two aspects is generated, and the particles' 3-D shape can be reconstructed. Darakis et al. (2010) employed digital holography to reconstruct 3-D particle shape. It is pointed out that holography has no issues related to focusing - this is its unique advantage over classical imaging techniques.

All these studies could successfully characterize 3-D particle shape, but they are on-line measurements and not in-situ instruments. In addition, all these designs need the particles or suspension to be with desired solid density to move through a fixed flow cell, so that the particles can be well imaged.

2.3 Process Imaging in Characterizing Particle Size and Shape

Process imaging is a relatively new technology to monitor and control industrial processes by 'seeing inside' what's happening in the process. Process imaging "refers to the use of image-based sensors, data processing concepts, and display methods for obtaining information about the internal state of industrial processes" (Scott & McCann 2005; Carlsohn, 2005). The obtained process information could be used for process monitoring and process control.

The process images may be represented differently depending on the sensor type. They may be black-and-white presented by 256 gray levels, color images represented by 3 RGB (Red, Green, Blue) values, images directly taken by CCD or Complementary Metal Oxide Semiconductor (CMOS) cameras, process tomography taken by x-ray, gamma-ray, microwave, acoustic and ultrasonic methods such as the Computerized Tomography (CT) x-ray scanning systems that is commonly used in medical diagnostics.

No matter how a digital image is obtained, it has to go through image processing steps so that one may extract as much process information as possible. The common image processing steps include image enhancement and object segmentation, etc. Image enhancement is usually the first step in image processing. The purpose of this step is to enhance the contrast of objects to

background and make the objects of interest to stand out in the image. The commonly used image enhancement methods include histogram analysis (Zuiderveld, 1994), gray-level transformation (Bovik, 2000), spatial filters for image smoothing or sharpening (Gonzalez & Woods, 2001) and image enhancement by frequency domain processing (Bovik, 2000). Object segmentation is the most important step in image processing and currently there are many available methods for this purpose. Examples imclude detecting the object's edges by edge detection methods (Canny, 1986), detecting straight lines through Hough transform (Duda & Hart, 1972), labelling the object's region through gray-level thresholding or region growing methods (Hojjatoleslami & Kittler, 1998), or generating pseudo images through multivariate statistical methods (Zhou, et al., 2007). Depending on the type of image and the different requirements of image processing, appropriate segmentation methods may be applied or combined together to process the digital images.

To satisfy the requirements of digital process monitoring and control, each segmented object should be quantitatively represented by shape and size. This may involve fitting the segmented object area into a circle which has the same area or perimeter of the object, or using a rectangle bounding box to include the object, or using some predefined shape factors (Wanibe & Itoh, 1998). The quantitative representation could accurately describe process states, which is further used for process monitoring and control.

The obvious advantage of process imaging is that it can really 'see inside' processes. The obtained 2-dimensional images contain much more information than traditional measurements. For example, in order to monitor the temperature of fire flame in furnace, the traditional measurements can only show one temperature value at one particular time and sample point, while process imaging may show the temperature value distribution of a region at one same sampling time. The abundant information provided by process imaging would help to determine process state more accurately and rapidly. The information may also be used to develop new products and processes.

2.3.1 Image Analysis Based Approach for PSD Estimation

With the rapid development of in-situ high-speed imaging systems, the acquired process images can qualitatively show the crystallization process state in real-time. To further quantify particle size and shape, the image processing methodologies should be fast, accurate and reliable. They must be able to isolate each particle and subsequently characterize each particle's size and shape. The biggest challenge of accurately isolating each particle is in clearly identifying each particle's outline, i.e. precise particle segmentation. Some studies (Calderon De Anda et al. 2005a, 2005b, 2005c; Qu et al., 2006) segmented particles with a multi-scale image analysis technique, where particles were segmented by

combining the results of two Canny edge detections (at different scales). This was followed by morphological operation to obtain the area of each particle. This technique is successfully applied to study nucleation kinetics and on-line monitoring of the polymorph transition of crystallization process.

Mazzotti and coworkers applied similar multi-scale image analysis techniques (Kempkes et al., 2008) to obtain the evolution of 2-D axis length distribution (ALD) in real-time. They then went on to restore 2-D PSD from 2-D ALD based on a genetic algorithm (Eggers et al., 2008). This technique was applied to monitor particle size and shape during cooling crystallization of ascorbic acid (Eggers et al., 2009). More, they developed a procedure to construct 3-D PSD with the innovation of their experimental setup (Kempkes, 2010).

For long needle-shape particles that have high-aspect-ratio, Larsen et al. (2006b) advocated using line detection followed by clustering to segment crystals from images, instead of edge detection and morphology operations. The hallmark of this method is that straight lines are detected from images and then grouped together to get a high-aspect-ratio rectangle representing the particle. No morphological operations are performed. The method was demonstrated to be robust and efficient for monitoring processes with moderate solid concentration. However, this method is only specific to needle-shaped systems. Applications to other high-aspect ratio systems would need further refinement/extension. Even for

systems where the particle has a needle shape, at early stages of the crystallization, other shapes such as cubes or ellipsoid (that do not have high-aspect-ratio) may persist. The performance of the method for such shapes has not been established. Larsen et al. (2007) further refined the approach by grouping the straight lines according to pre-defined models of particle shape The improved method is more accurate, robust and reliable to suspend solutions with high solid concentration. In some crystallization processes, agglomeration may occur soon after nucleation, resulting in particle clots of random shapes. These cannot be easily handled even in the revised scheme.

Hungerbuhler's group detected nucleation and identified metastable zone of crystallization using process images. They used the mean gray intensity method to convert endoscopy images into 8-bit gray format, which were further processed with background subtraction, thresholding and noise elimination steps to detect the nucleation of the first crystal (Simon et al., 2009a, 2009b). Recently, they also developed a multivariate image analysis method, which is based on image feature descriptors, to perform on-line monitoring of nucleation (Simon et al. 2010a).

Applying image analysis techniques to on-line process images not only provides the opportunity to monitor the particle size and shape (Kempkes et al., 2008), but additional factors that reveal the underlying crystallization kinetics can also be deciphered – for instance, the growth rates of each face of a particle (Ma et al.,

2007; Wang et al 2007) can be obtained. Similarly, population properties of different morphologies can be estimated since particles of different shapes can be segregated from the measured features. Zhou et al. (2007) showed that the aspect ratio is usually above 1.5 for long needle shape MSG crystals and in the range of 1 - 1.3 for cubic salt particles. Additional 3-dimensional particle information (Wang et al., 2008) can also be extracted.

2.4 Major Image Analysis Steps

PVM images offer a snapshot of the process state. Each image may contain several particles – small and large, some distinct and others overlapping together. The objective, irrespective of the contents of the image, is to extract the size and shape of each particle from which the process state – particle shape and size distribution – can be calculated. The isolation of each particle from the image is termed as particle segmentation. IA techniques seek to automatically perform particle segmentation. Most publications in IA for PSD have used the same broad steps. In this section, we review these major steps and summarize the challenges in IA when applied to PVM images of crystallization systems.

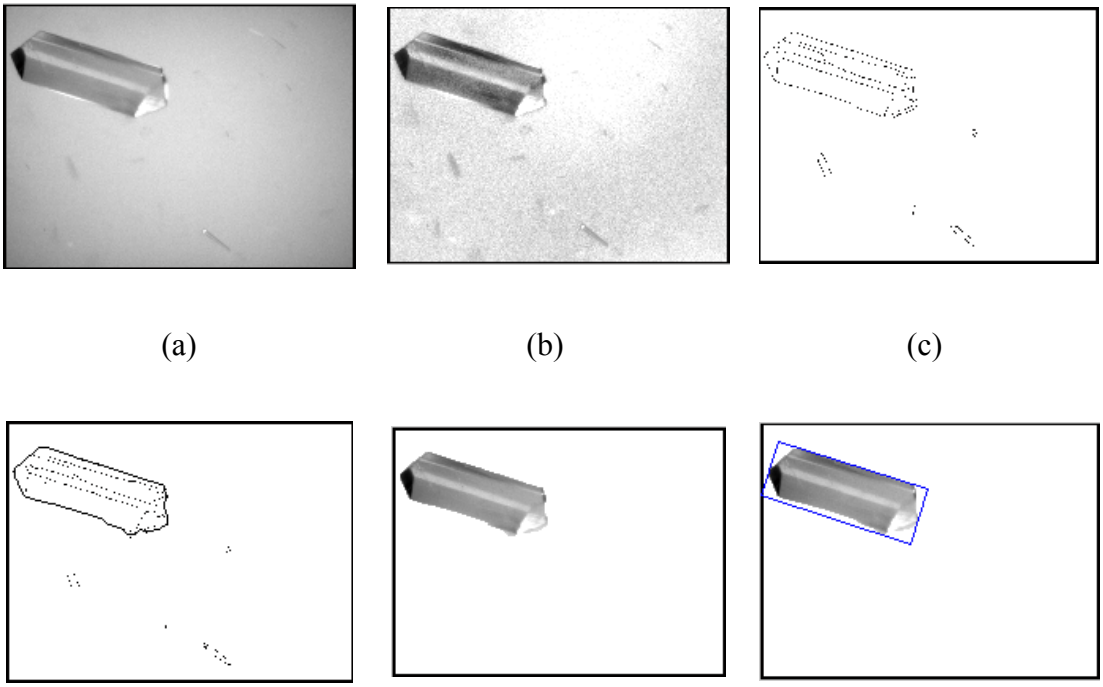

(a) (b) (c)

(d) (e) (f)

Figure 2.5. Steps in image analysis.
(a) original PVM image (b) enhanced image (c) edge detection (d) morphology operation (e) isolated particle (f) feature extraction

Each image $I(x,y)$, as shown in Fig. 2.5 (a), is a matrix of pixels. Each pixel at position (x,y) has an intensity value I ranging from 0 to 255, which corresponds to the pixel color changing from black $(I=0)$ through grey to white $(I=255)$. The size of the matrix (and the image) depends on the equipment and its setting. We use 640x480 pixels as the typical size for images, although the PVM can also be set at 320x240 pixels and 1280x960 pixels. The first step in particle segmentation is to detect the outlines in the image. For this purpose, the raw image I may be first enhanced through background subtraction or other transformations to obtain an enhanced image $\tilde{I}$, as shown in Fig. 2.5 (b).

2.4.1 Edge Detection

The operation of edge detection is a critical step that is intended to find the edges of objects of interest in the image. The most popular edge detectors are Sobel edge detector (Gonzalez & Woods, 1992), Prewitt edge detector (Pratt, 1991), Robert edge detector (Rosenfeld & Kak, 1982), and Canny edge detector (Canny, 1986). The edge detectors compute the gradient magnitude of pixel intensity values, and find the edges when the gradient magnitude is greater than a threshold value. Canny edge detection is employed in this thesis since it detects both edge magnitude and edge direction.

Canny edge detection consists of four steps. The first step is to filter the enhanced images with a Gaussian filter mask,

$$\tilde{\tilde{I}} = \tilde{I}(x, y) * G(x, y) \tag{2.6}$$

where,

$$G(x, y) = \frac{1}{2\pi\sigma^2} e^{-\frac{x^2+y^2}{2\sigma^2}} \tag{2.7}$$

and σ is the standard deviation of the Gaussian smoothing filter. Next, the edge magnitude and direction of each pixel are calculated by calculating the first derivative of the Gaussian filtered image $\tilde{\tilde{I}}$. At each pixel, the two partial derivatives c_x and c_y, in the x and y directions corresponding to the vertical and horizontal slope respectively, are obtained.

$$C(x,y) = \begin{bmatrix} c_x \\ c_y \end{bmatrix} = \begin{pmatrix} \frac{\partial \tilde{\tilde{I}}(x,y)}{\partial x} \\ \frac{\partial \tilde{\tilde{I}}(x,y)}{\partial y} \end{pmatrix} \tag{2.8}$$

The edge magnitude defined as

$$M = \sqrt{c_x^2 + c_y^2} \tag{2.9}$$

and edge direction defined as

$$\phi = \tan^{-1}\left[\frac{c_x}{c_y}\right] \tag{2.10}$$

can be obtained.

The third step is to find all the local maximum magnitudes along gradient direction, and mark these pixels as edge pixels. This step results in thinned edge line. The last step applies hysteresis thresholding to mark the final edges. In this step, two threshold values T_1 and T_2 (T_1<T_2) are used. An edge pixel is defined as a strong edge if its magnitude is greater than T_2. If the edge magnitude is between T_1 and T_2, the pixel is marked as a weak edge. Weak edge pixels are incorporated into strong pixels if they are 8-connected. Edge pixels are linked to form an edge line. Edge detection thus converts the original gray-level image *I(x,y)* into a binary image *B(x,y)*, where the edge points are labeled as 1 and background points as 0.

Canny edge detection thus requires three parameters to be specified – the T_1 and T_2 threshold values and the standard deviation of the Gaussian filter, σ. The

threshold values define the strong edge and weak edges and connect them together to denote the edge. The choice of σ also has a significant effect on the processed image. A high value of σ leads to a wider distribution and blurs the image, so that only the most prominent edges are detected. A small value of σ leads to a narrow distribution and flags not only the prominent edges but also the less prominent ones, as shown in Fig. 2.5 (c).

2.4.2 Morphology Operation

The objective of morphology operations is to extract objects of interest from the image. Dilation and erosion are fundamental morphological operations. These operations are performed by letting a predefined binary window of structuring element S slide across the binary image B. Dilation is the union of S and B - this means any elements belonging to either S or B will belong to the new dilation set, i.e., Dilation=OR[S,B]. Dilation operation fills in small holes and expands the object boundaries. The erosion operation generates the new set by finding all the elements that belong to both S and B, i.e. Erosion=AND(S,B). The erosion operation shrinks the object boundary (Bovik, 2000).

Morphological closing and opening combine the operations of dilation and erosion. Image closing involves use of erosion followed by dilation. Closely adjacent objects are first merged together. Image filling is subsequently used to

fill the holes in the closed objects' area and to make the objects smoother. Morphological opening, which involves the operation of dilation followed by erosion, is then performed to remove small isolated pixels. The operation of morphological closing followed by image filling and opening removes imperfections such as holes from the particle without affecting its shape or size.

The predefined structuring element S, which gives the shape information of interest, is an important factor that affects the shape of the object obtained through morphology operations. When the binary structuring element S slides across the binary image B, S must overlap with at least one 1-valued pixel of B. Therefore, the shape of S affects the objects' outline in image B. There are a lot of choices to define S. For example, it could be defined as a disk, line, rectangle, diamond, square or octagon. Even for a given shape, various sizes and orientations can be used. As stated earlier, the shape and size of the structuring elements have to be pre-specified, and will affect the final outline and area of the segmented particles.

After the morphology operations, as shown in Fig. 2.5 (d), all small objects with pixel area less than a pre-specified threshold are removed. Similarly, objects that touch the image border are eliminated from further consideration. Fig. 2.5 (e) demonstrates the isolated objects. The outlines of the remaining objects are obtained as n-point pairs in Cartesian coordinates $[x_1, y_1; x_2, y_2; \ldots; x_n, y_n]$ in clockwise or counterclockwise direction. Particle features are then extracted from

the outline.

2.4.3 Feature Extraction

There are several methods to measure the size of the particle from the outline (Wang, 2006). Two common methods are based on the maximum chord length and the best-fit minimum-area rectangle, as shown in Fig. 2.6. Both these methods are rotation-invariant. The maximum chord length method calculates the distance between any two points of a particle's outline as a particle chord length. The maximum chord length is defined as the particle length.

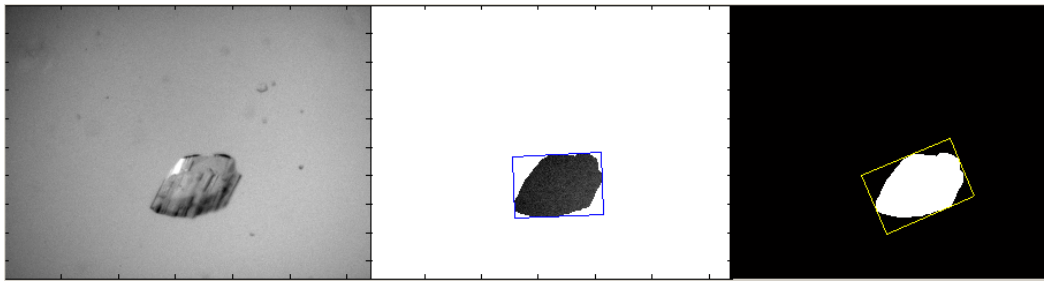

(a) (b) (c)

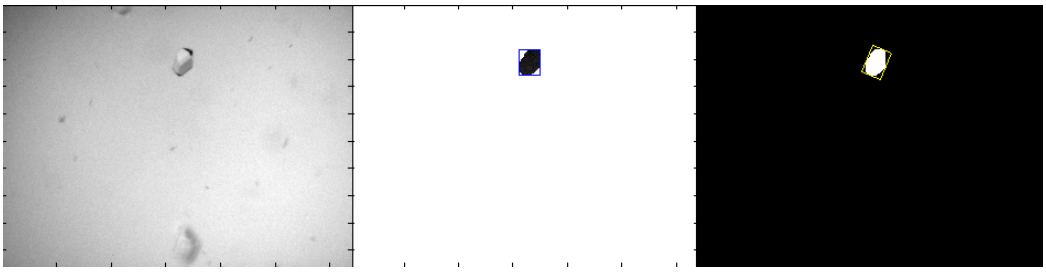

(a') (b') (c')

Figure 2.6. Comparison of two kinds of bounding box.
(a) and (a') are original PVM images; (b) and (b') show the minimum area bounding boxes, (c) and (c') show the bounding boxes obtained from major axis.

The particle width could be defined as the maximum chord length that is perpendicular to the particle length, as shown in Fig. 2.7. Alternatively, it can be defined as the width of a rectangle that has the same area as the segmented particle. In the best-fit minimum-area rectangle method, each extracted object is fit into a minimum-area rectangle using the rotating calipers method (Toussaint, 1983; Pirzadeh, 1999; Chaudhuri & Samal, 2007), as shown in Fig. 2.5 (f). The particle size and shape is based on this rectangle. Once the particle length and width have been obtained, other derived features such as the aspect ratio (ratio of particle length to width) can also be calculated.

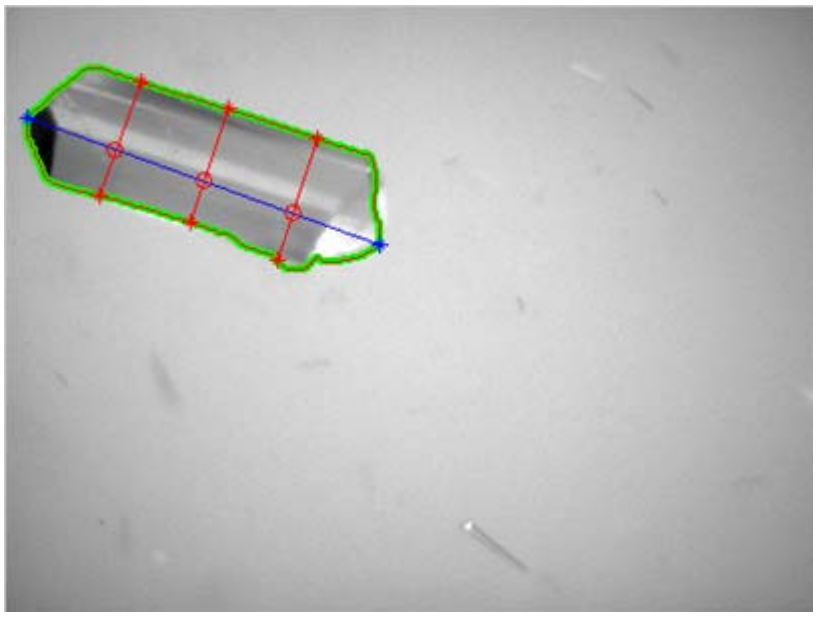

Figure 2.7. Feature extraction of segmented particle.
Particle length is defined as the maximum chord length; particle width is defined as the maximum chord length that is perpendicular to the particle length.

2.5 Conclusions

Desired particle shape and uniform particle size are the common requirements for good quality of crystallization product. The currently available in-situ PAT instruments are able to characterize particles in real-time. ATR-FTIR predicts the concentration of solution, FBRM measures CLD, Raman and NIR detect structure and PVM characterizes particle size and shape. These measurements and characterizations make it possible to monitor and control the crystallization processes.

With the advancement of process imaging, there is a surge in interest to study crystallization process. The literature studies show that process imaging technology is capable to characterize particle size and shape in real time. It provides industry with more opportunities to monitor and control particle growth, understand polymorph transition, characterize metastable zone, etc.

Chapter 3. Development Of New On-Line Image Analysis Methodologies

In order to automatically characterize particle size and shape from in-line process images, certain image analysis steps are required to process images that are acquired from specific crystallization systems. This chapter will extend the basic image analysis steps reviewed in Section 2.4 and develop an image analysis (IA) methodology. These extensions are in image selection, image pre-processing and particle selection steps and account for the specific characteristics of PVM images, as described next.

3.1 Image Selection

The PVM takes images of particles as they come into the field of view. These in-process images may contain not only particles, but also bubbles and other aberrations caused by inadequate lighting. When the vessel contains no particles, the images merely show the background. While the developed method is fast and accurate enough for quantifying particles from images containing clear particles, significant computational time is entailed while identifying objects in blank or

poor quality images. Therefore, while dealing with processes that evolve from low (or no) solids concentration to high solids concentration, the first step is to automatically select good quality images. Since particles and background usually have different intensity values in the image, it is obvious that the intensity histogram of images containing clear particles would differ substantially from those without. Thus promising images can be identified quickly based on their intensity range ($\Delta I = I_{\max} - I_{\min}$).

$$\text{If} \begin{cases} \Delta I \geq T_k \ \& \ I_{\min} \leq T_{\min} & \text{Image has particles} \\ \text{Else} & \text{Image does not have particles} \end{cases} \tag{3.1}$$

where T_k and $T_{\min}$ are user-specified thresholds. Images which match this criterion are selected for subsequent analysis.

This is further demonstrated in Fig. 3.1 and 3.2. For the image in Fig. 3.1 (a), the maximum and minimum intensities are $I_{\max} = 238$ and $I_{\min} = 121$ respectively, and the intensity range is $\Delta I = I_{\max} - I_{\min} = 117$. On the other hand, for the image in Fig. 3.1 (e), the maximum and minimum intensities are $I_{\max} = 231$ and $I_{\min} = 17$ respectively, and the intensity range is $\Delta I = I_{\max} - I_{\min} = 214$. Hence it is easy to see that thresholds of intensity range (T_K) and minimum intensity threshold ($T_{\min}$) should exist. Let us say for this set of images, only the images with intensity range greater than 150, i.e., $T_K = 150$ and minimum intensity less than 100, i.e., $T_{\min} = 100$ will be selected for further analysis.

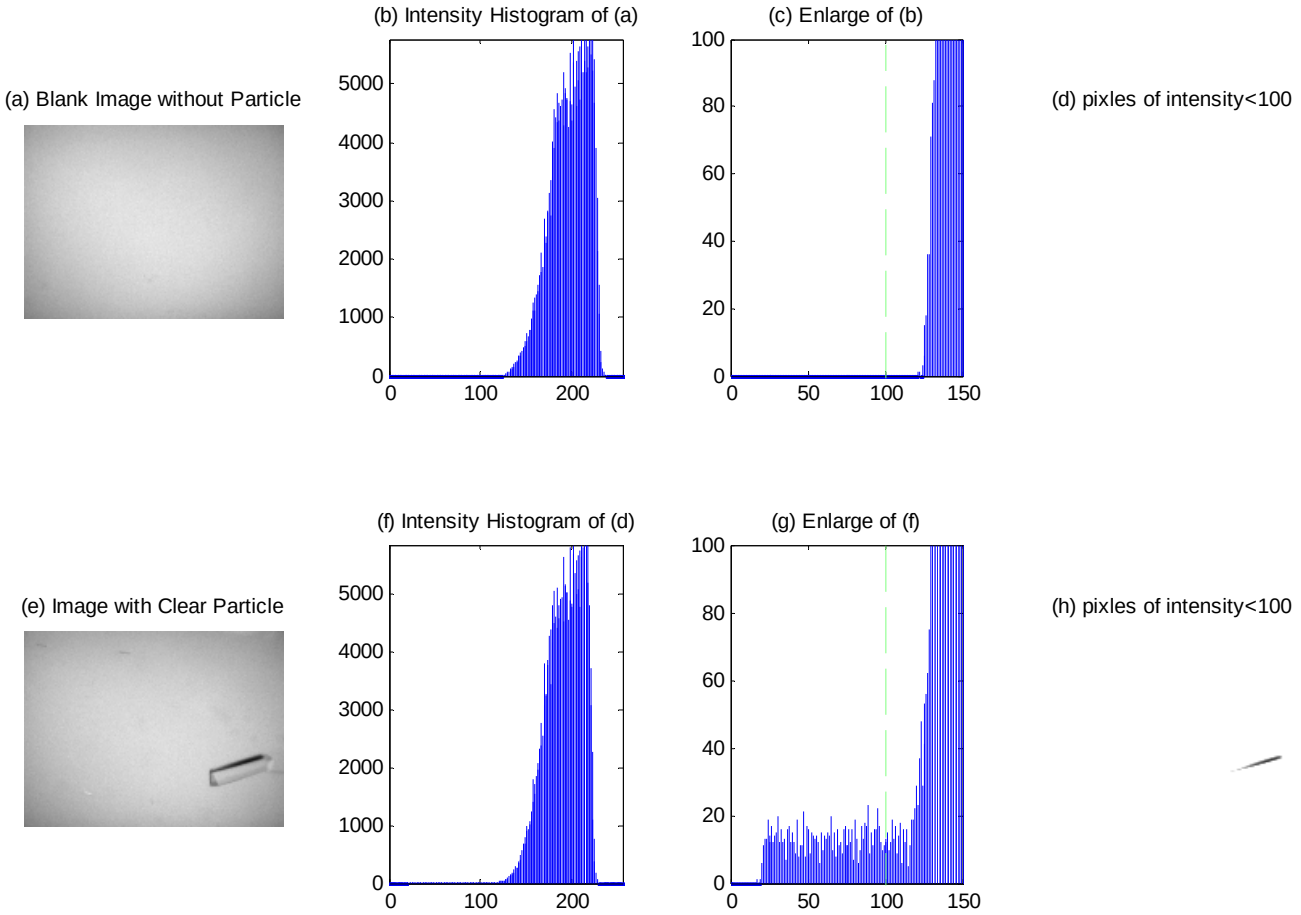

Figure 3.1. Comparison of the intensity histogram of images with and without MSG particles inside.
(a) original image without particle; (b) the intensity histogram of image (a);
(c) enlarge (b) at the intensity ranged from 0 to 150; (d) pixels of intensity <100 in (a); (e) original image with clear particle; (f) the intensity histogram of image (d); (g) enlarge (e) at the intensity ranging from 0 to 150; (h) pixels of intensity <100 in (e).

Even for process images in which the object-to-background contrast is not very high, this selection criteria works well. Fig. 3.2 demonstrates the process images of silica gel. In Fig. 3.2 (a), the image does not contain any particle. It has a $I_{\max} = 166$ and $I_{\min} = 87$. The intensity range is $\Delta I = I_{\max} - I_{\min} = 79$. The image in Fig. 3.2 (e) has particles. Its $I_{\max} = 239$, $I_{\min} = 47$, and $\Delta I = I_{\max} - I_{\min} = 192$. Similarly, the thresholds of $T_K = 100$ and $T_{\min} = 70$ could be set for image selection.

3.2 Image Enhancement

PVM images usually have systematic variation in the intensity across the image – the center is much brighter than the edge – due to the nature of illumination source in the probe. This systematic variation complicates threshold selection in the various IA steps. For example, if a high pixel value is used as threshold, the four corners will be considered as objects in the binary images, while a low threshold value will blank out the particle objects as well. Fig. 3.3 demonstrates this problem, where both the crystal and the four corners are transferred into black color in the binary image.

To eliminate this, a reference image without particles $I_{\text{Ref}}(x, y)$, as shown in Fig. 3.4, is taken at the beginning of each experiment. All subsequent images are normalized by subtracting this reference image, i.e., $\tilde{I}(x, y) = I(x, y) - I_{\text{Ref}}(x, y)$.

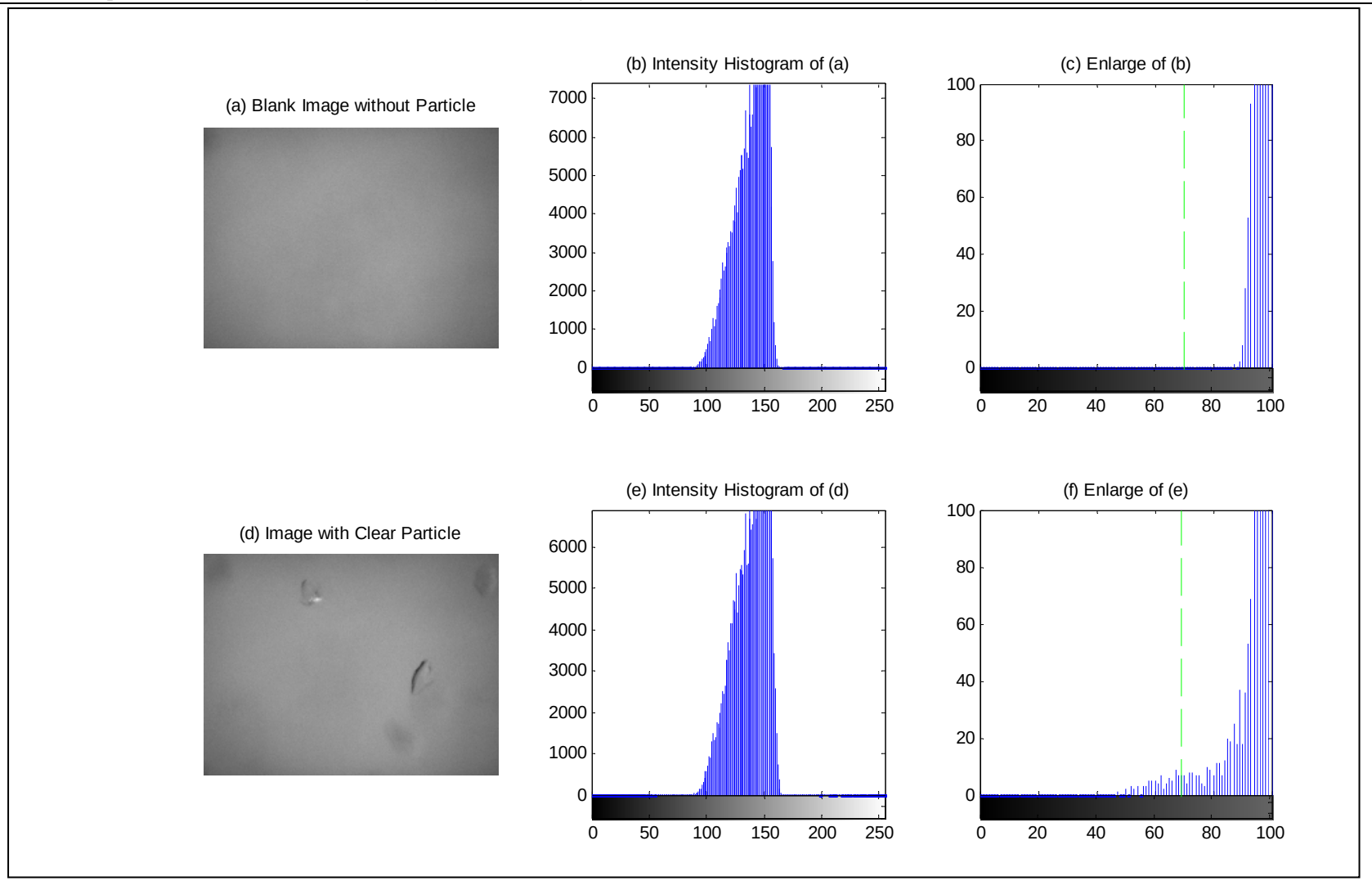

Figure 3.2. Comparison of the intensity histogram of images with and without silica gel particles inside.
(a) original image without particle; (b) the intensity histogram of image (a); (c) enlarge (b) at the intensity ranging from 0 to 150; (d) original image with clear particle; (e) the intensity histogram of image (d); (f) enlarge (e) at the intensity ranging from 0 to 150.

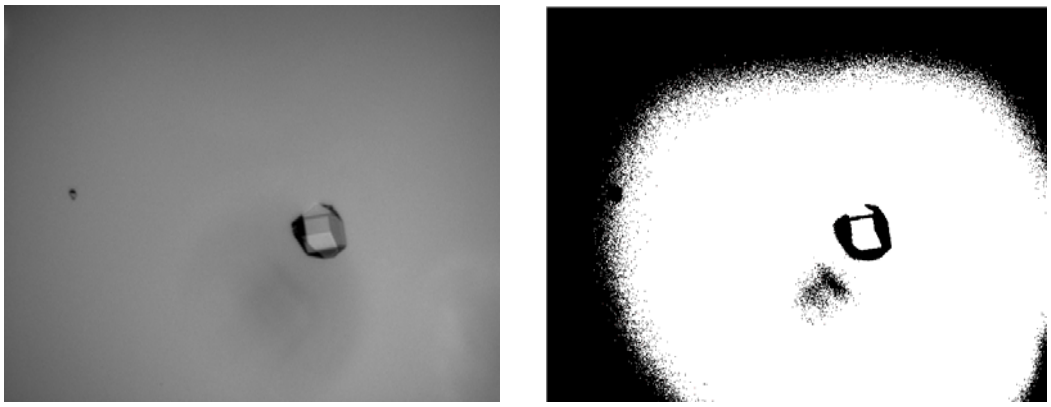

Figure 3.3. Problem of non-uniform background.
(a) original image; (b) binary image by directly threshold original image, the four corner are threshold as objects as well.

Figure 3.4. Reference image, $I_{\mathrm{Ref}}(x, y)$.

Further image enhancement using contrast-limited adaptive histogram equalization (Zuiderveld, 1994) was also evaluated. Fig. 3.5 illustrates the effect of image enhancement.

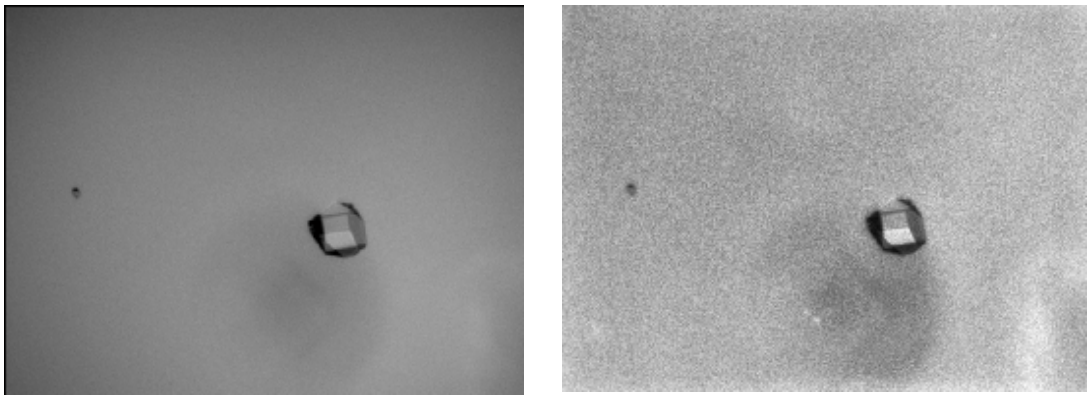

(a) (b)

Figure 3.5. Effect of image enhancement.
(a) original image; (b) result of image enhancement.

3.3 Particle Selection

The output from the morphology operation is the outline of objects in the image. While most of these would be particles of interest, some would be bubbles and clots formed by aggregating particles arising from noise and other imperfections in the image. To get an accurate estimate of particle size, it is important to take into consideration only those sizes which can be definitely attributed to particle. Therefore, we include a particle selection step.

Specifically, the signature curve (Gonzalez et al., 2004) is used to identify if the object outline obtained after morphology operations corresponds to a regular particle. First, the outline is smoothed using Discrete Fourier Transform (DFT) to obtain all the Fourier descriptors. Next, the outline is reconstructed using only the largest descriptors, thus resulting in a smoother boundary without high-frequency (curvy) edges, as shown in Fig. 3.6. A signature curve – which is a one-dimensional representation of the two-dimensional outline – is calculated for the reconstructed

outline as follows: First the centroid of the object $(\hat{X},\hat{Y})$ is calculated using the points in the outline.

$$\hat{X}=\frac{1}{n}\sum_{i=1}^{n}x_i \quad ; \quad \hat{Y}=\frac{1}{n}\sum_{i=1}^{n}y_i \tag{3.2}$$

Then, the points in the outline are described in a new polar coordinate system with the centroid as the origin. For the i^{th} point in the outline,

$$r_i=\sqrt{\left(x_i-\hat{X}\right)^2+\left(y_i-\hat{Y}\right)^2} \tag{3.3}$$

$$\theta_i=\tan^{-1}\left(\frac{\left(y_i-\hat{Y}\right)}{\left(x_i-\hat{X}\right)}\right) \tag{3.4}$$

The (r_i, θ_i) plot of the outline points in clockwise or counter-clockwise direction is called the *signature curve*. Since the boundary is a closed curve, the angle would range from 0^o (the start point) to 360^o (the end point).

The signature curve is a single-valued function of increasing angle and could be used to indirectly identify the quality of segmentation. Each geometrical shape has a specific signature curve. For instance, a spherical particle would have a circular outline, therefore its signature curve would be a straight line. Needle-shaped particles would have four local maxima – the two larger ones separated by about 180^o corresponding to the particle length and the smaller two corresponding to the particle width and also 180^o apart. The signature curve is therefore used to confirm if

the outline after the morphology operation corresponds to a well segmented particle. Particle size resulting from an improperly segmented object whose signature curve is "noisy" and does not have the peaks separated by about 180^{o} are therefore not used in subsequent calculations.

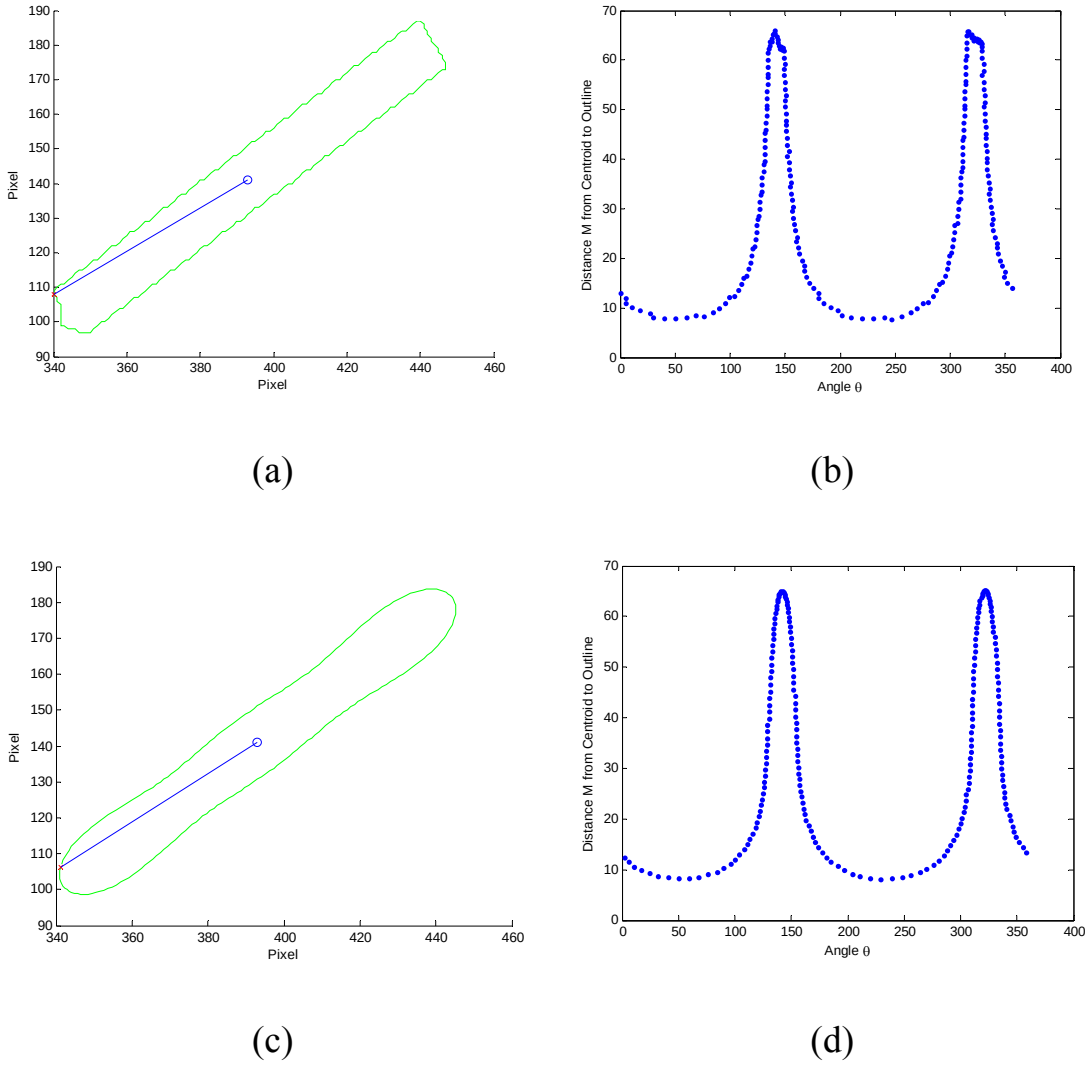

Figure 3.6. Signature curve for segmented and smoothed particles. (a) outline of a segmented particle; (b) signature curve of particle in (a); (c) smoothed particle outline obtained through Fourier transform; and (d) signature curve of particle in (c)

3.4 Size Estimation

The signature curve can also be used to estimate the particle size. As shown in Fig. 3.6, the two larger peaks that are separated by about 180^o correspond to the two points that are most separated. We use this as a computationally efficient means to estimate the particle length.

A particle's maximum chord length can be estimated from both coordinate positions and signature curve. From Fig 3.7(b), the two peaks (θ_i, r_i) that are separated by about 180^o are $P1'(142,65.0)$ and $P2'(322,65.2)$ Hence, the maximum chord length can be estimated as:

$$CLD_{Max}' = r_{P1'} + r_{P2'} = 130.2 \quad \text{pixels} \tag{3.5}$$

The corresponding coordinate positions of $p1'$ and $P2'$ in Fig. 3.7(a) are P1(342, 101) and P2(443, 181). This particle's maximum chord length also could be calculated as:

$$CLD_{Max} = \sqrt{(x_{P1} - x_{P2})^2 + (y_{P1} - y_{P2})^2} = 128.8 \quad \text{pixels} \tag{3.6}$$

Similarly, the two bottom minimums (θ_i, r_i) that are separated by about 180^o in Fig. 3.7(b) are $B1'(50,8.3)$ and $B2'(229,8.2)$ the minimum chord length, CLD_{Min}', can be estimated as 16.5 pixels. The corresponding coordinate positions of $B1'$ and $B2'$ in Fig. 3.7(a) are B1(398, 135) and P2(388, 147), and the estimated minimum cord length CLD_{Min} is 15.6 pixels.

The estimated maximum chord length, CLD_{Max}, and minimum chord length, CLD_{Min}, are considered as particle length and width, respectively.

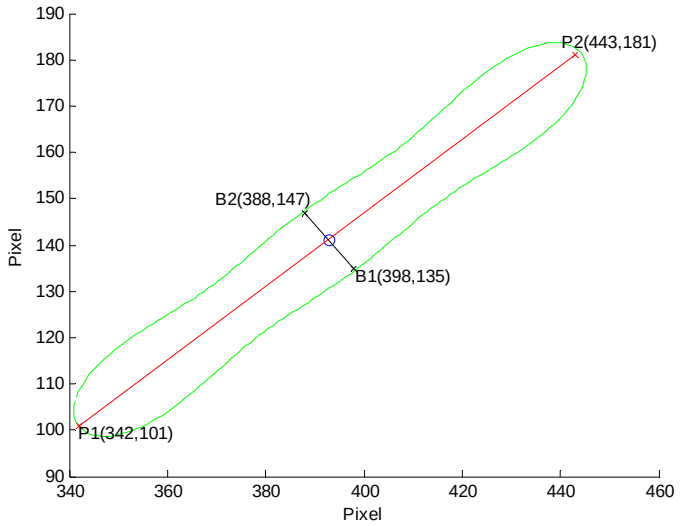

(a)

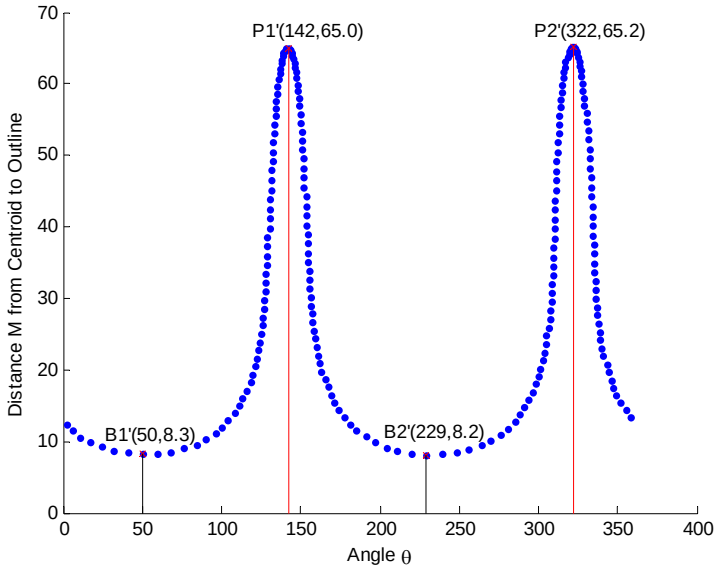

(b)

Figure 3.7. Particle size estimation from signature curve.
(a) particle size estimated from particle's coordinate position; (b) particle size estimated from particle's signature curve.

3.5 Overall Steps of Image Analysis (IA) Methodologies

Fig. 3.8 summarizes all the steps in the proposed IA methodology that is applied to each image acquired from the experiment. More examples of applying IA in different systems, such as silica gel, sea sand, sea salt, MSG and mixture of sea salt & MSG, are demonstrated in Fig. 3.9 to 3.13 respectively. By statistically combining the particle sizes from sets of adjacent images, size distributions and particle growth can be tracked as a function of time.

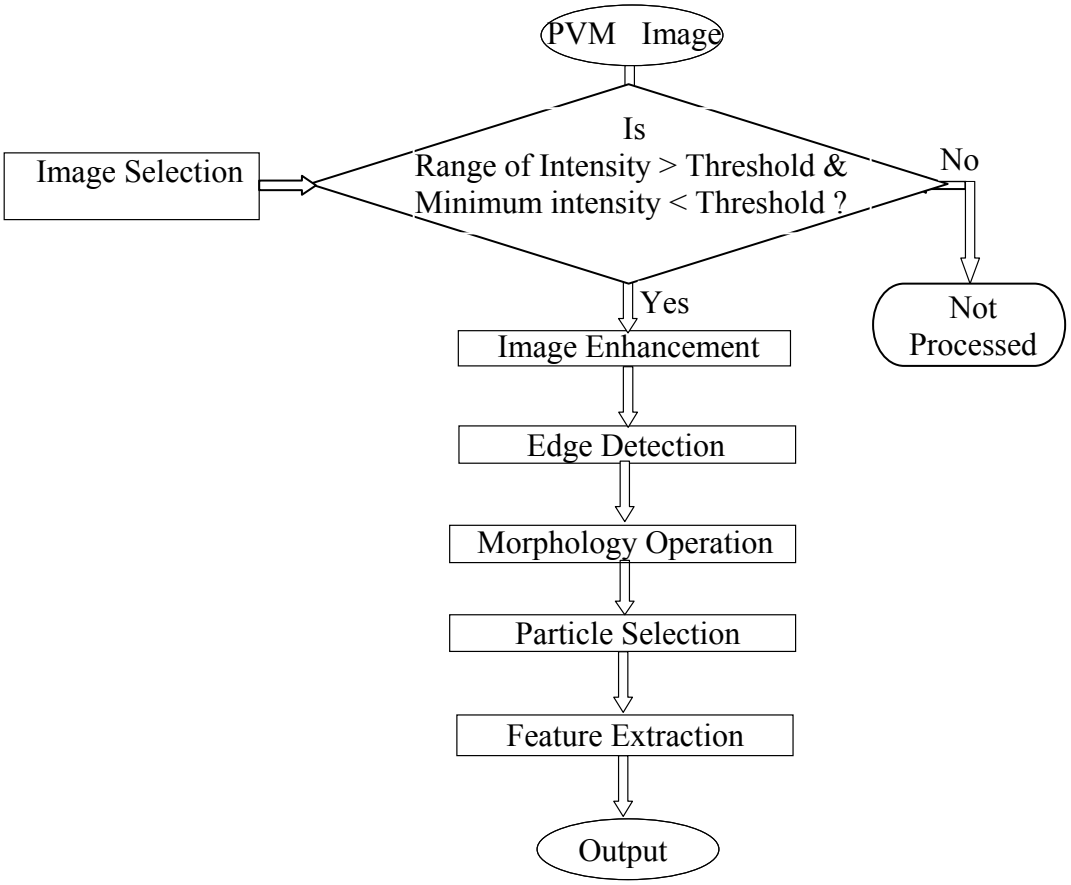

Figure 3.8. Proposed methodology for on-line image analysis.

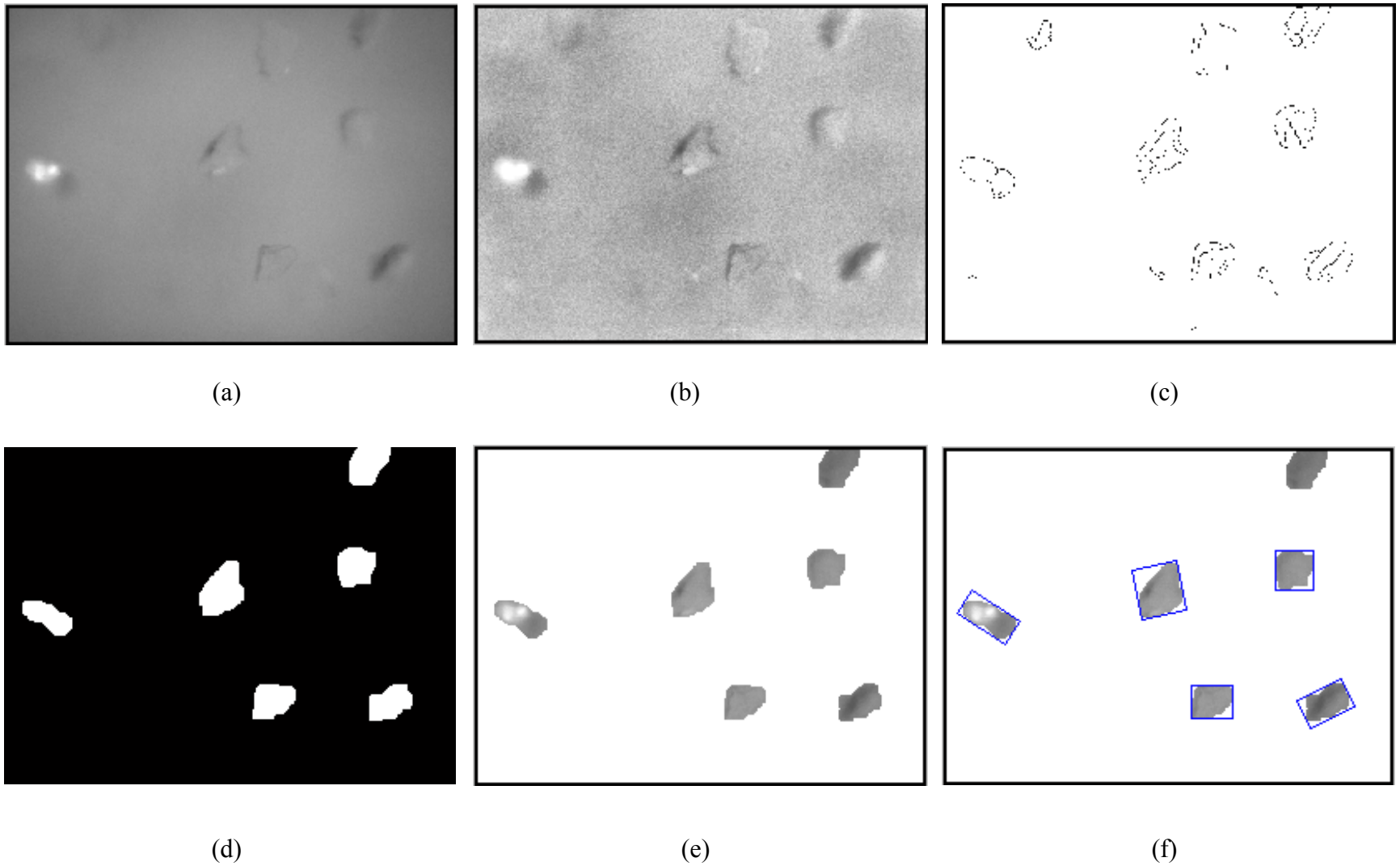

Figure 3.9. Steps in image analysis of silica gel PVM image.
(a) original PVM image; (b) enhanced image; (c) edge detection; (d) morphology operation; (e) isolated particle; (f) feature extraction.

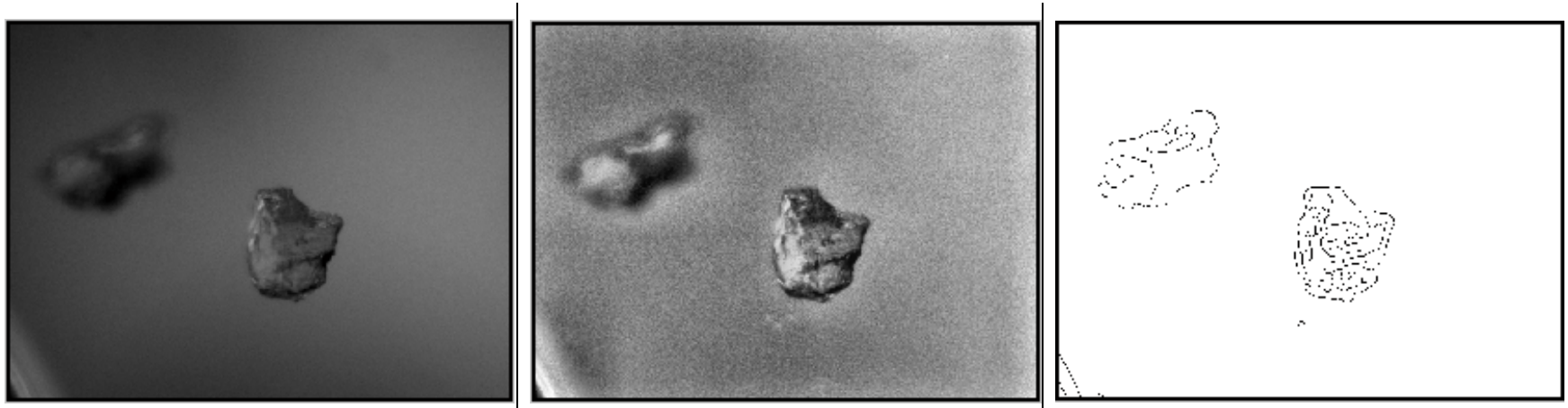

(a) (b) (c)

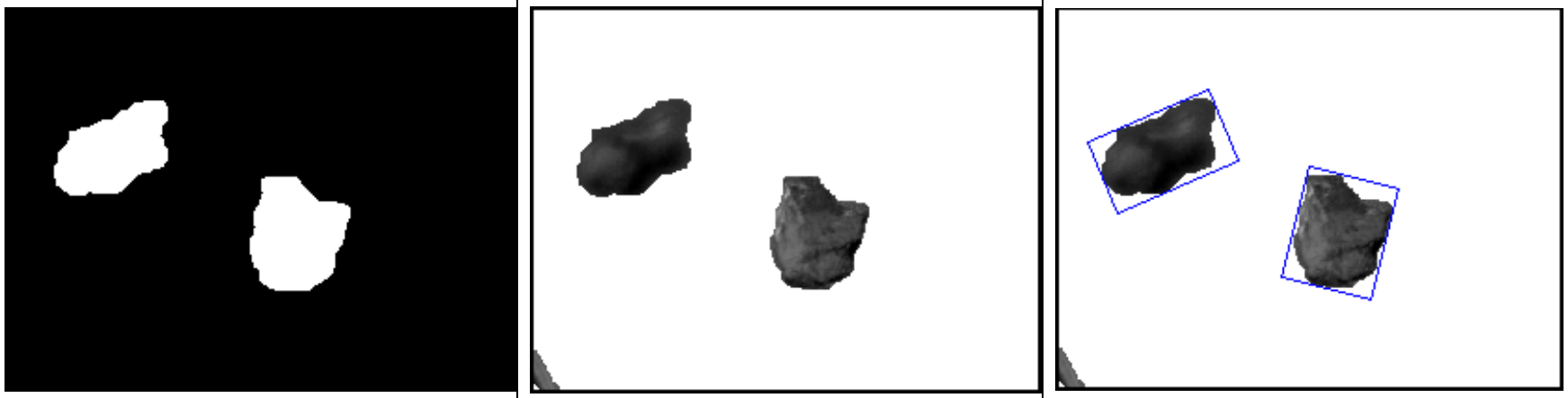

(d) (e) (f)

Figure 3.10. Steps in image analysis of sea sand PVM image.
(a) original PVM image; (b) enhanced image; (c) edge detection; (d) morphology operation; (e) isolated particle; (f) feature extraction.

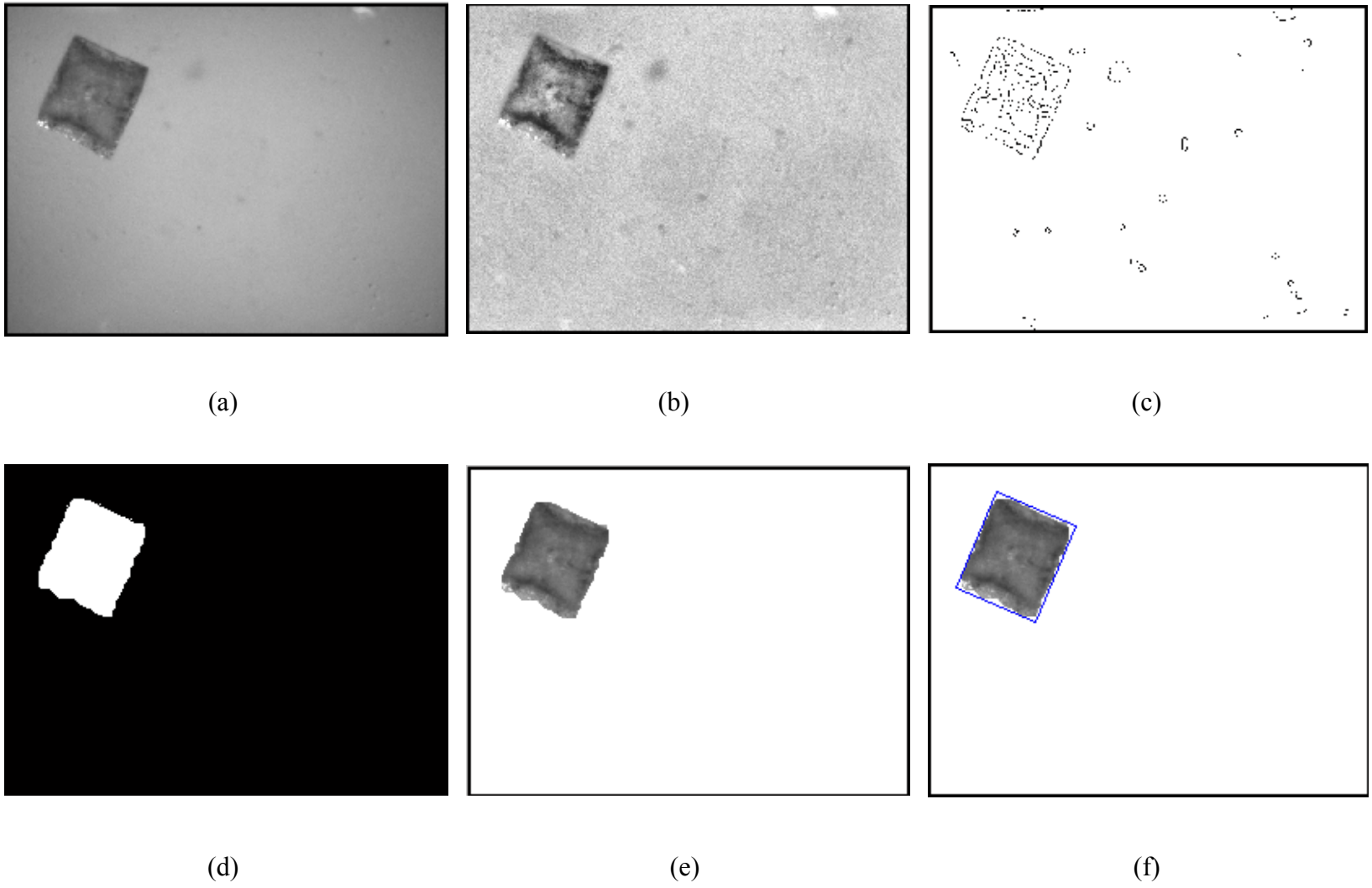

(a) (b) (c)

(d) (e) (f)

Figure 3.11. Steps in image analysis of sea salt PVM image.
(a) original PVM image; (b) enhanced image; (c) edge detection; (d) morphology operation; (e) isolated particle; (f) feature extraction.

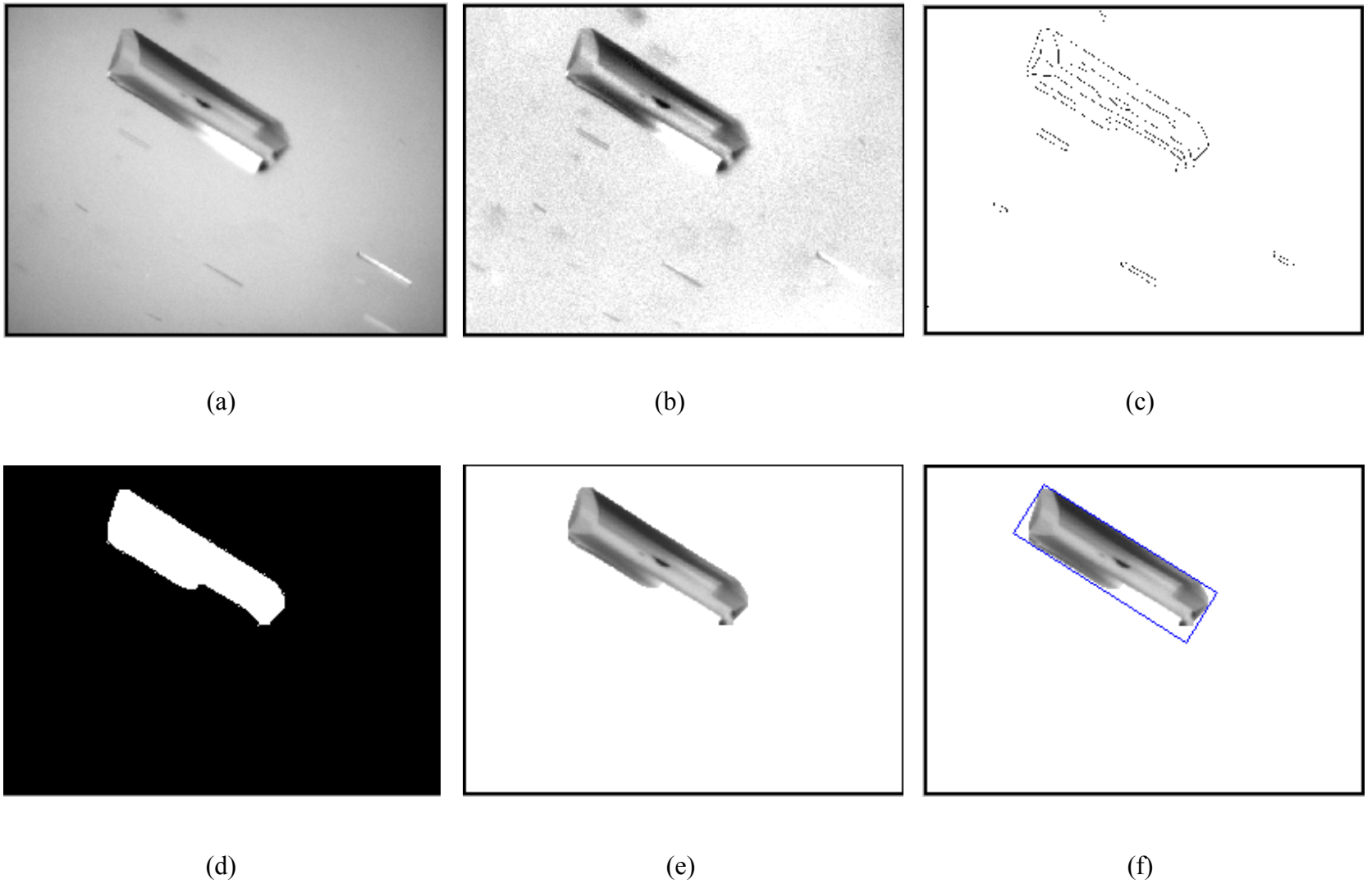

Figure 3.12. Steps in image analysis of MSG PVM image.
(a) original PVM image; (b) enhanced Image; (c) edge detection; (d) morphology operation; (e) isolated particle; (f) feature extraction.

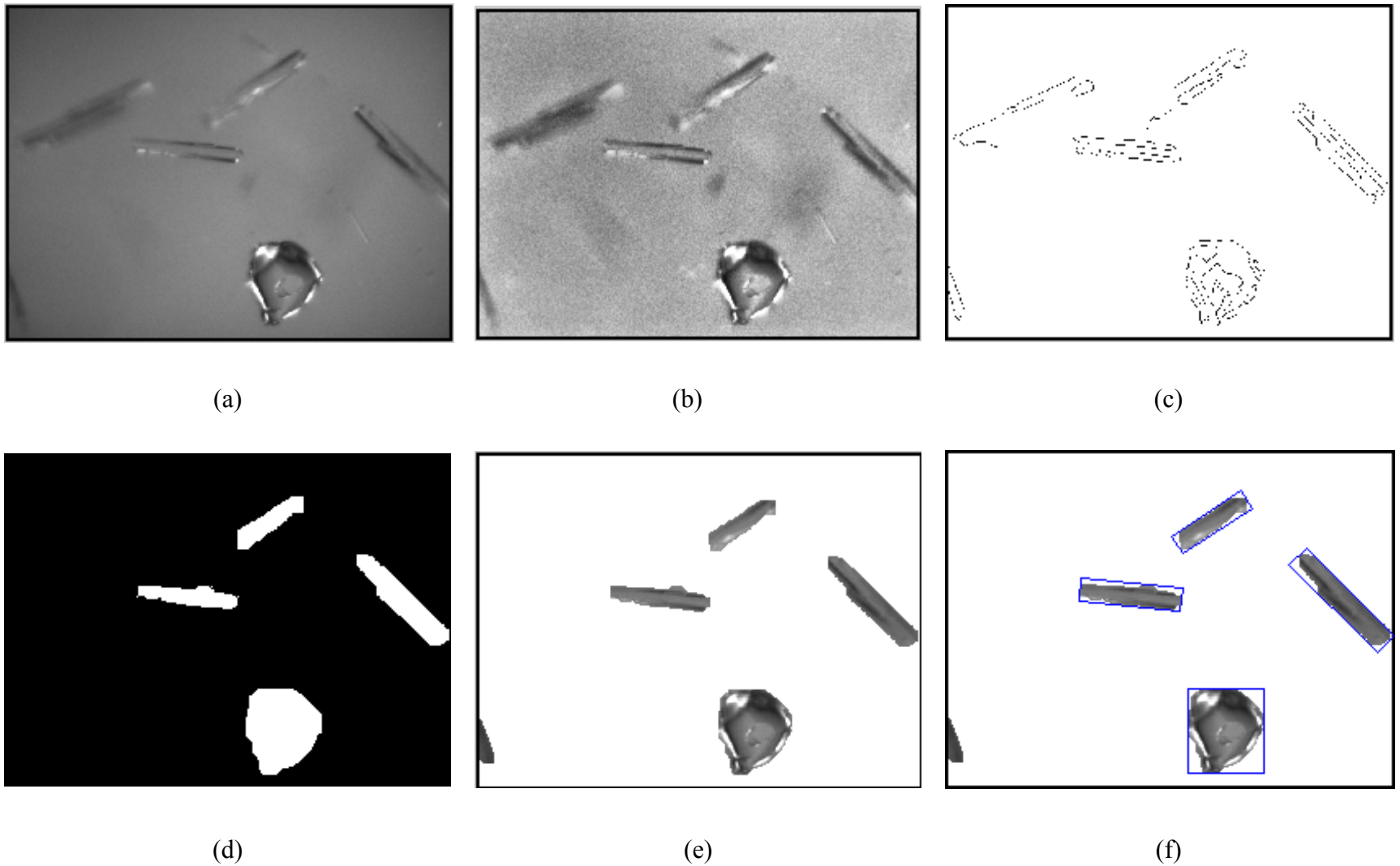

Figure 3.13. Steps in image analysis of sea salt & MSG mixture PVM image.
(a) original PVM image; (b) enhanced image; (c) edge detection; (d) morphology operation; (e) isolated particle; (f) feature extraction.

3.6 Conclusion

Based on the major image analysis steps in literature, an extended image analysis (IA) methodology, mainly focused on PVM images acquired from crystallization process, is developed in this chapter. It improves the computing efficiency by selecting only non-blank images for further analysis, eliminates the non-uniform background that occurs in process images, evaluate isolated objects, and characterize particle size with signature curve. The examples demonstrate that IA could properly segment particles from PVM images.

Chapter 4. Experimental Studies

This chapter describes the experimental setups for on-line monitoring of crystallization processes. PVM, FBRM and ATR-FTIR were employed to the crystallization system to acquire various process measurements in real-time. Two kinds of experiments were carried out with this experimental setup. One experiment was based on sea sand with known size range and size distribution. The purpose of this experiment was to correlate the in-line PVM measurements with off-line Microscopy measurements based on a system with know characteristics. Another set of experiments were conducted to monitor the particle growth in seeded MSG crystallization process by in-line analysis of the acquired PVM images.

4.1 Experimental Setup

The experimental setup is shown in Fig. 4.1. A 500ml jacketed flat-bottom glass reactor is used as crystallizer. A 4-bladed Teflon impeller driven by an overhead motor is used for mixing. Each blade is at a 45^{o} angle to the horizontal, and the stirrer blade is located at about one-third of the height of liquid above the bottom of the vessel.

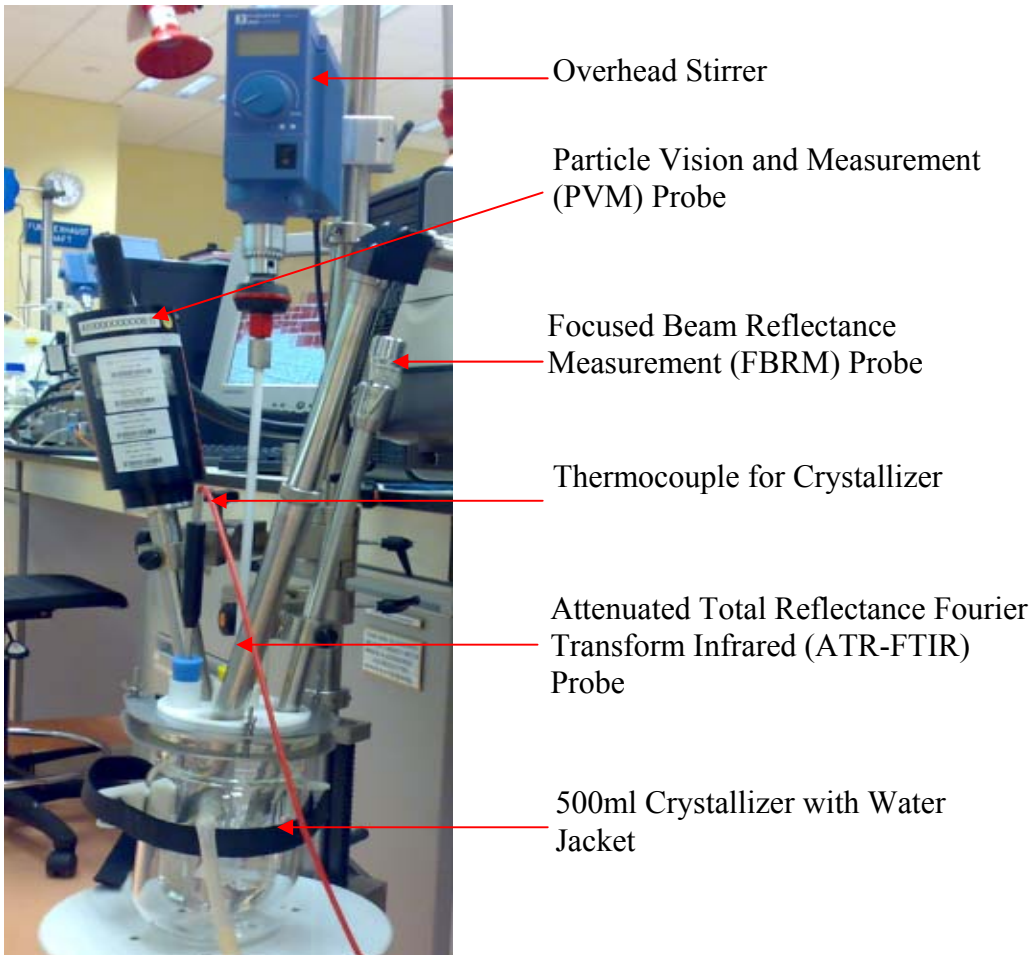

Figure 4.1. Experimental setup.

PVM (model 700) and FBRM (model D600L) from Lasentec / Mettler Toledo were inserted into the solution at an angle of about 45^{o}. They were connected to a Pentium III computer (CPU: 1G HZ; Memory: 256MB), where PVM instrumental software (Particle Vision Measurement PVM 700) and FBRM software (FBRM Data Acquisition Control Interface 6.0) were installed. The obtained image is 480x640 pixels corresponding to a 645x860 μm^2 field of view. This implies that one pixel is equal to 1.344 μm. Although the PVM software allows up to 10 images per second to be stored, this rate could not be really reached in actual operation. Therefore, a lower image acquisition speeds (up to 2 images /second) is used in our

experiments.

FTIR spectrometer (Nicolet 4700 from Nicolet Instrument Co.) equipped with a Dipper-210 ATR immersion probe (manufactured by Axiom Analytical Inc.) were used to collect absorbance spectra. A conical ZnSe crystal was sealed into the probe with two ATR reflections. The spectra of DI water at room temperature were used as background. A spectrum was acquired every minute and each spectrum had 64 scans in the range of 600 to 4000 cm^{-1}.

A Julabo circulator FP50-HL with capability to heat and cool is used to control the crystallizer temperature; a stainless steel Pt100 thermocouple is used for measuring the crystallizer temperature. This communicated with the control computer via RS232 interface.

Fig. 4.2 shows the schematic of the experimental setup. Various in-situ instruments acquire different signals and send them to the control computers for further analysis. The obtained process information, such as the particle chord length distribution from FBRM measurements, solution concentration characterized from ATR-FTIR spectra, particle size distribution and shape estimated from PVM images, are passed on to a central control computer. The central control computer will monitor and control the process in real-time by adjusting the temperature of the circulator.

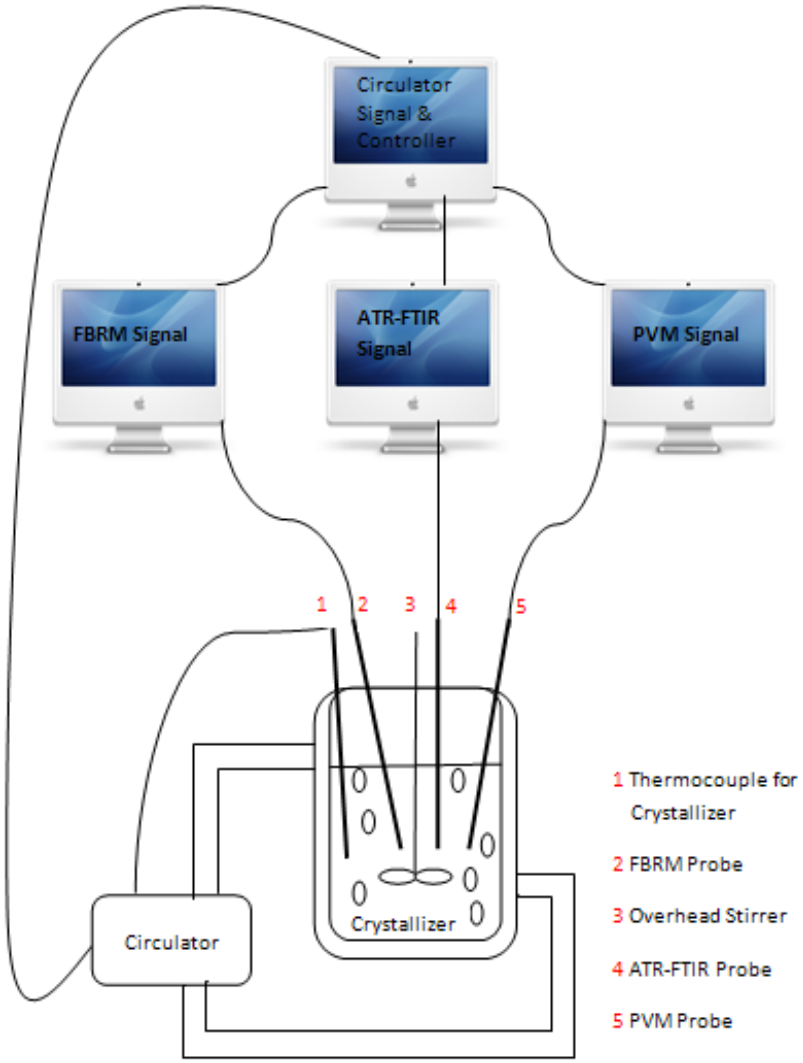

Figure 4.2. Schematic diagram of experimental setup.

4.2 Experiments

With the experimental setup in Fig 4.1 and 4.2, two experimental studies were performed for validating the PVM imaging system and the IA methodology – the first a simple study on sea sand (without variation of particle size and shape, as described in Section 4.2.1) and the second one which is a complex study of crystallization process (with growth of particle size, as described in Section 4.2.2).

In the first experiment, sea sand was separated into five different size ranges and put into DI water. The collected PVM images were compared with off-line microscopy images in order to validate the PVM imaging system. The second experiment dealt with the measurement and size estimation of a seeded batch cooling crystallization process of MSG from DI water.

4.2.1 Experiments with Sea Sand

The purpose of these experiments was to compare the accuracy of the particle size estimates from the PVM imaging system and determine its consistency with microscopy measurements. In the microscopy measurements, all particles are photographed on a flat plate, so the distance of particles from the lens is fixed and the particles are stationary. Compared to the PVM images, these microscope images are also much clearer, and therefore easier to process by image analysis. Therefore, we expect accurate measurements of particle size from microscopy and hence use it as a benchmark and to estimate the errors introduced by the PVM imaging system. The detailed experimental procedure is described as below:

a) Sea sand was separated into five different size ranges with sonic sifter and sieves. From top to bottom, the edge sizes of square holes of the sieves are 150μm, 125 μm, 106μm, 90μm, 75μm, 53μm respectively. The sea sand particles are then grouped into 5 sets with different particle ranges of 53 - 75μm (Set A), 75 - 90μm (Set B), 90 - 106μm (Set C), 106 - 125μm (Set D) and 125 - 150μm (Set E).

b) For each size range, an experiment was conducted separately. A small

amount of sea sand sample, (0.42 gram for Set A, 0.50 gram for Set B, 0.80 gram for Set C, 1.30 gram for Set D and 1.10 gram for Set E), was mixed with 250ml DI water and poured into the crystallizer and stirred at 350rpm. The amount of sea sand sample is different for each set. The bigger particle size requires the more amount of sample to ensure that the numbers of particles are similar in each set.

c) For each set, the experiment was conducted for about one hour, PVM images were saved at a speed of 2 images/second and over 3000 PVM images, (3149 images for Set A, 3779 images for Set B, 4483 images for Set C, 7730 images for Set D and 5077 images for Set E), were acquired; typical images are shown in Fig. 4.3. FBRM data was saved at a frequency of every 2 seconds, as shown in Fig. 4.4.

d) Off-line images of small amount of samples from each of the five sets of sieved sea sand were also taken using an Olympus BX51 microscope. 500 microscopy images (about 2000 sea sand particles) were acquired for each set. Fig. 4.5 shows some typical microscopy images.

4.2.2 Seeded Cooling Crystallization of MSG from DI Water

With the same experimental setup described in Section 4.1, detailed investigation of IA's accuracy was performed by monitoring particle growth in seeded crystallization experiments.

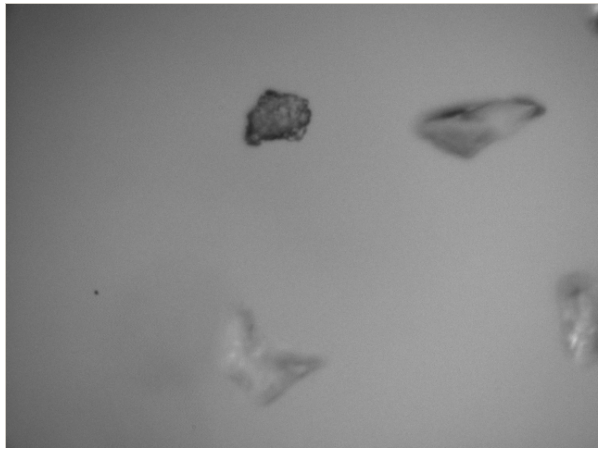

(a) Set A

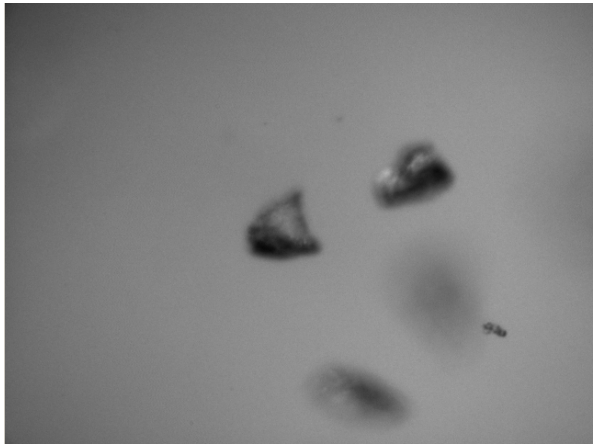

(b) Set B

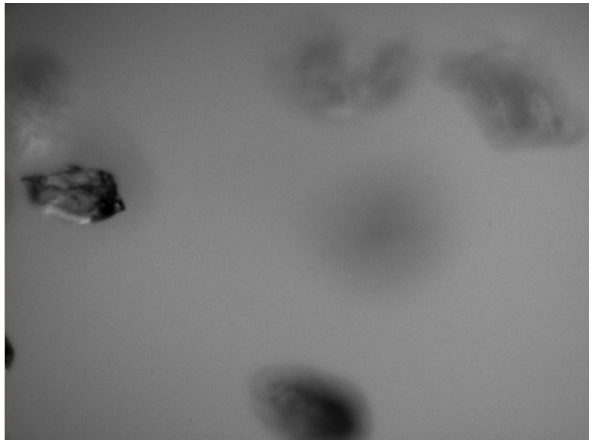

(c) Set C

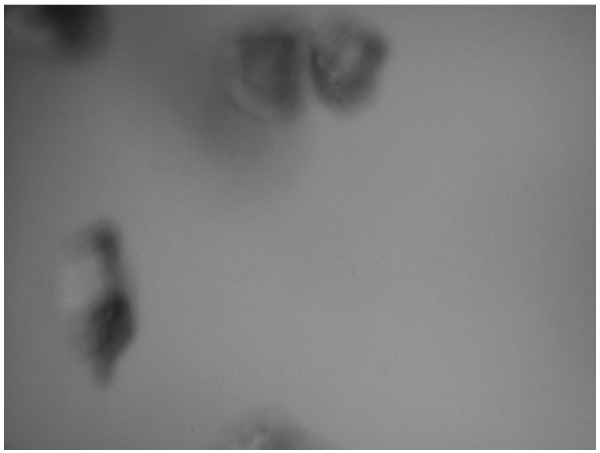

(d) Set D

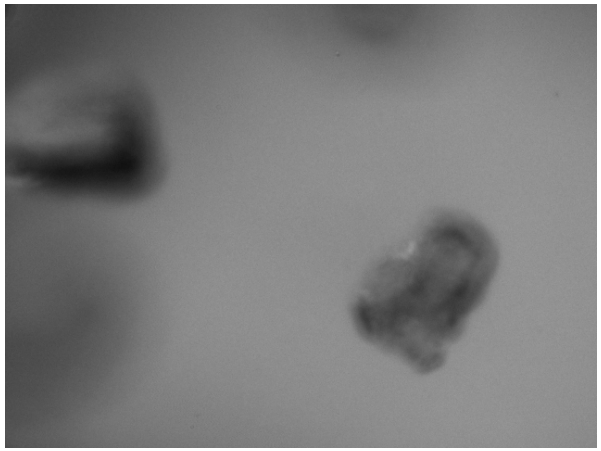

(e) Set E

Figure 4.3. PVM images of sea sand particles of various size ranges. (a) set A (sieve size: 53-75μm); (b) set B (sieve size: 75-90μm); (b)set C (sieve size: 90-106μm); (d) set D (sieve size: 106-125μm); (e) set E (sieve size: 125-150μm)

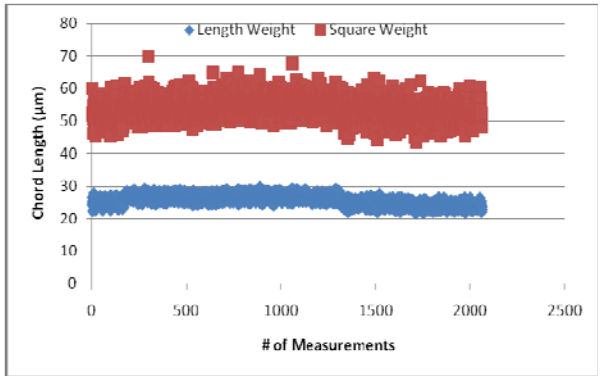

(a) Set A

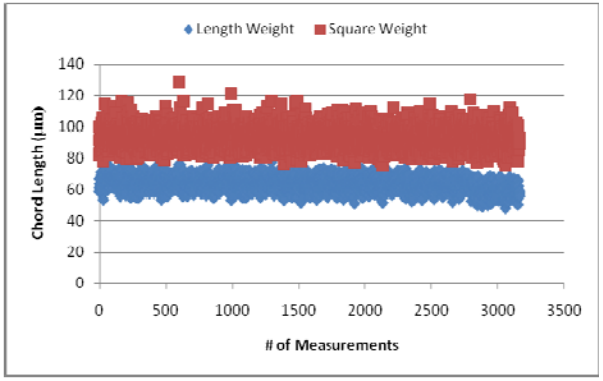

(b) Set B

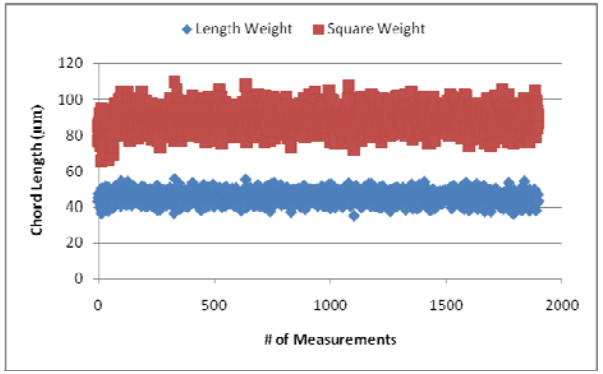

(c) Set C

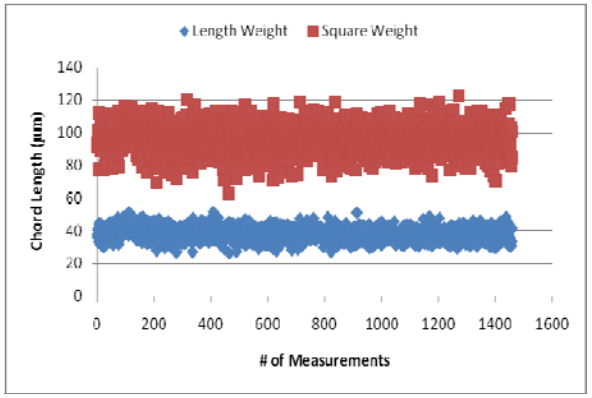

(d) Set D

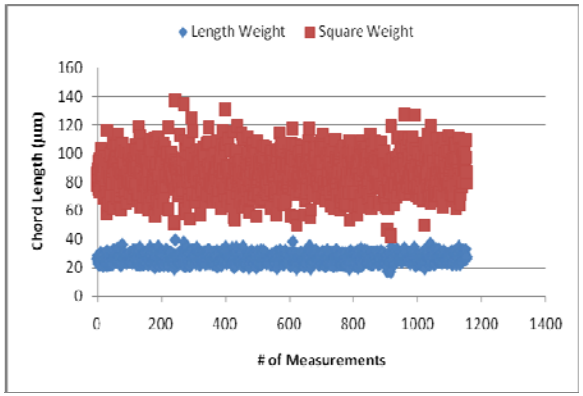

(e) Set E

Figure 4.4. FBRM measurements of sea sand particles of various size ranges. (a) set A (sieve size: 53-75µm); (b) set B (sieve size: 75-90µm); (c) set C (sieve size: 90-106µm); (d) set D (sieve size: 106-125µm); (e) set E (sieve size: 125-150µm)

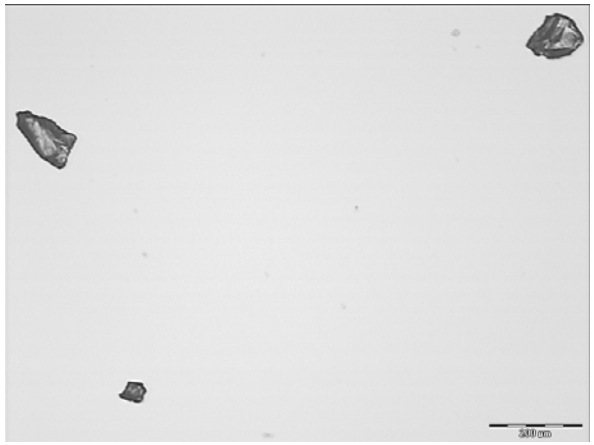

(a) Set A (10X)

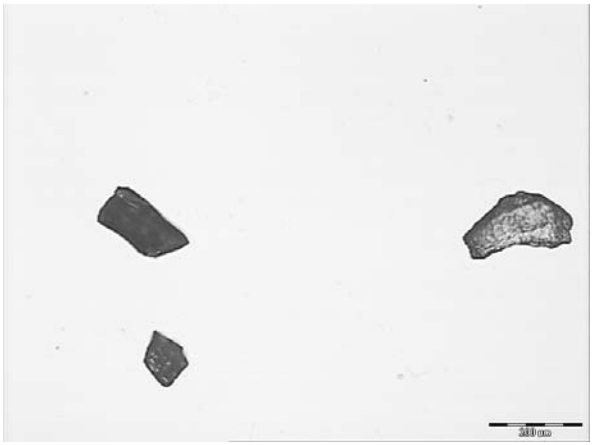

(b) Set B (10X)

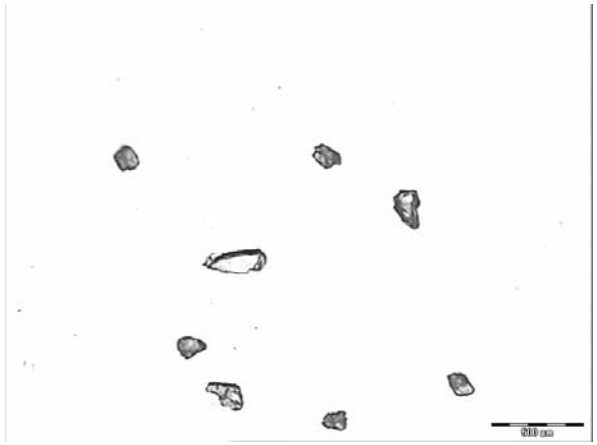

(c) Set C (4X)

(d) Set D (4X)

(e) Set E (4X)

Figure 4.5. Microscopy images of sea sand particles of various size ranges. (a) set A (sieve size: 53-75μm); (b) set B (sieve size: 75-90μm); (c) set C (sieve size: 90-106μm); (d) set D (sieve size: 106-125μm); (e) set E (sieve size: 125-150μm)

4.2.2.1 Monosodium Glutamate

MSG (L-Glutamic Acid Monosodium Salt Monohydrate from Sigma-Aldrich; ≥98.0% TLC) is selected as the chemical for case study. MSG is a flavor-enhancing compound that provides the savory taste in food. The substance was discovered and identified in the year 1866, by the German chemist Karl Heinrich. It is widely used as additive in food industry to produce fermented or aged food such as soya sauce, fermented bean paste and cheese.

MSG is a sodium salt consisting of sodium cations and glutamate anions. The formula of MSG is $C_5H_8NNaO_4.H_2O$ and the molecular structure of MSG is shown in Fig. 4.6. MSG appears as white crystalline powder. Its molecular weight is 187.14 AMU and melting point is 225^{o}C.

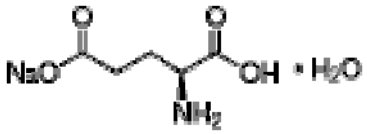

Figure 4.6. Molecular structure of l-glutamic acid monosodium salt monohydrate.

Solubility

MSG is very soluble in water (even in saliva). With the experimental setup described earlier, experiments were conducted to measure its solubility from 10^{o}C to 80^{o}C by both in-line ATR-FTIR approach and off-line evaporation approach. One experiment is conducted at every 5^{o}C interval. The measured solubility at each temperature is shown in Fig. 4.7. Both approaches are consistent at most (12 out 16) of the measurements, except the 3 experiments at 15^{o}C, 60^{o}C and 65^{o}C. If off-line

evaporation approach is considered as more reliable, the deviation of ATR-FTIR measurements may due to its sensitiveness to unknown ambient factors or experimental conditions.

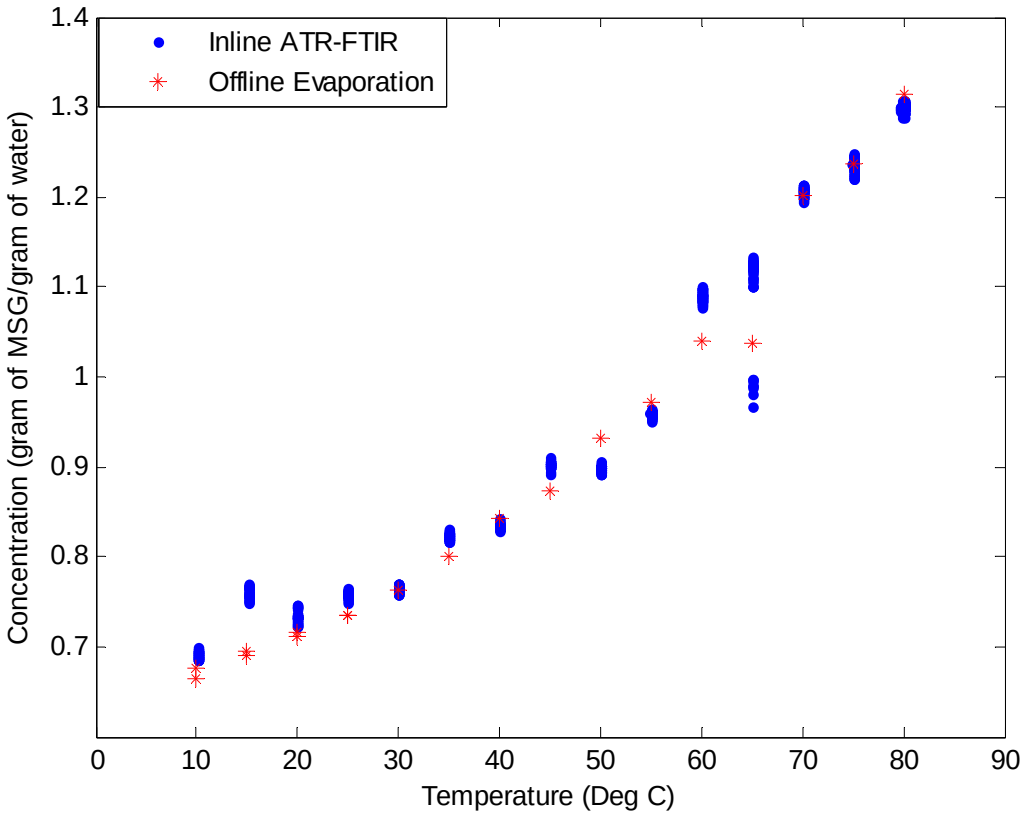

Figure 4.7. Solubility measured by ATR-FTIR and evaporation approaches.

For each experiment, a large amount of MSG is added to 400 ml DI water, the slurry is kept at a fixed temperature and stirred overnight to make it saturated and stable. Then, ATR-FTIR measures the spectrum of the slurry at a speed of 1 measurement per minute for 30 minutes. After that, 3 samples are taken with syringes that are equipped with filter (0.20μm syringe driven filter unit from Millipore Corporation). The 3 samples are weighted and dried in an oven at 45^{o}C for 1 week. MSG solubility was calculated from the weight change before and after drying.

ATR-FTIR measures the absorbance of infrared light and only spectra data is acquired. It is well known that ATR-FTIR spectrum vary with the solutions concentration and temperature. For example, Fig. 4.8 shows the typical ATR-FTIR spectra that are collected at certain concentration and temperature from the solution of MSG in DI water.

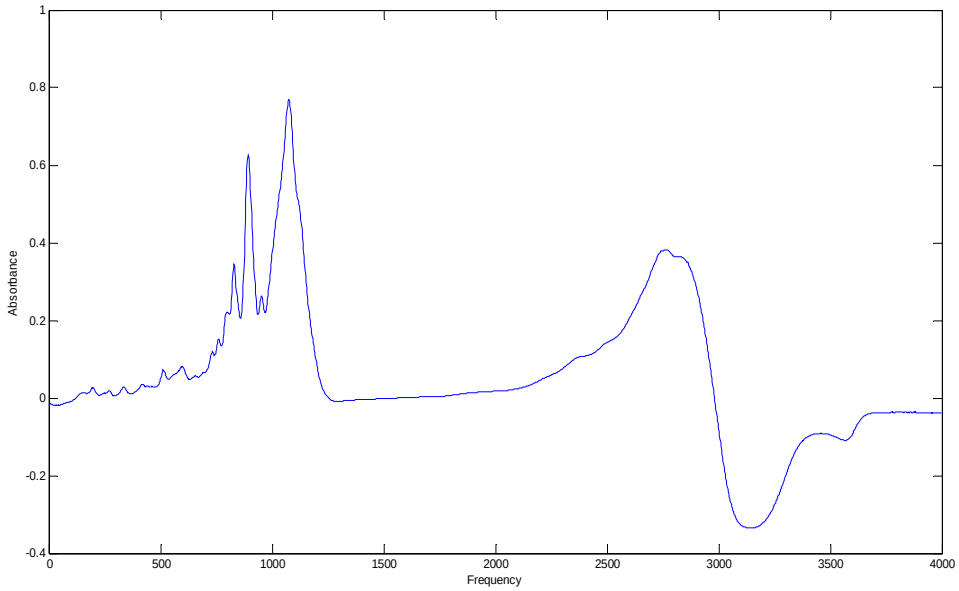

Figure 4.8. ATR-FTIR spectra collected at certain concentration and temperature from the solution of MSG in DI water.

To calibrate solution concentration and temperature with ATR-FTIR spectrum, a series of spectra are collected from solution with known concentration and temperature. Table 4.1 lists the experiments conducted for calibrating ATR-FTIR spectra. Principal component regression (PCR) is then applied to construct the calibration model between concentration, temperature and ATR-FTIR spectrum, which is represented as

$$C = b^T x \quad (4.1)$$

where, C is the solution concentration (predicted variable or output), x is the vector of predictor variables (spectra and temperature), which serve as the inputs and b is the regression coefficient.

The total 432 spectra (as listed in Table 4.1) were divided into training sets and validation sets. All the even numbered spectra belong to the training sets. All the odd numbered spectra belong to the validation sets. 10 principal components were extracted from a range of frequency (800 – 1200 cm^{-1}) and temperature measurements (total 174 predictor variables x) to build PCR model.

Table 4.1: Experiments for Calibrating ATR-FTIR

Expt. #	Fixed Concentration (gMSG/gDIWater)	Temperature Range (^oC)	Cooling Rate (^oC/min)	Number of Spectrum collected
1	0.6625	20 – 5	0.5	33
2	0.6750	25 – 10	0.5	31
3	0.6875	30 – 15	0.5	31
4	0.7000	35 – 20	0.5	29
5	0.7125	40 – 25	0.5	30
6	0.7250	45 – 30	0.5	31
7	0.7375	50 – 35	0.5	31
8	0.7500	55 – 40	0.5	31
9	0.7625	60 – 45	0.5	32
10	0.7750	65 – 50	0.5	31
11	0.7875	70 – 55	0.5	31
12	0.8000	75 – 60	0.5	31
13	0.8125	80 – 65	0.5	31
14	0.8250	85 – 70	0.5	29

4.2.2.2 Experimental Procedures

The temperature profile for all the MSG experiments is shown as in Fig. 4.9.

a) 320g of MSG is added to 400ml DI water at room temperature, heated in 30 minutes to 80°C and maintained there for additional 30 minutes to ensure that all the MSG is dissolved.

b) The solution is then cooled to 50°C at a rate of 1°C/min, and then to 30°C at 0.5°C/min.

c) Subsequently, the solution is held at 30°C until the end of the experiment (up to 118 hours).

d) To prepare the seed, a small amount of MSG is ground and sieved. Particles within sieve size of 38-45μm are set aside as seeds. 1g of the seed is added to initiate crystallization when the solution is at 40°C (stirring speed 350 rpm). Typical microscopy images of prepared seeds are shown in Fig. 4.10.

e) At the end of the experiment, the final solution is filtered, the product dried at 40°C for 24 hours and weighed.

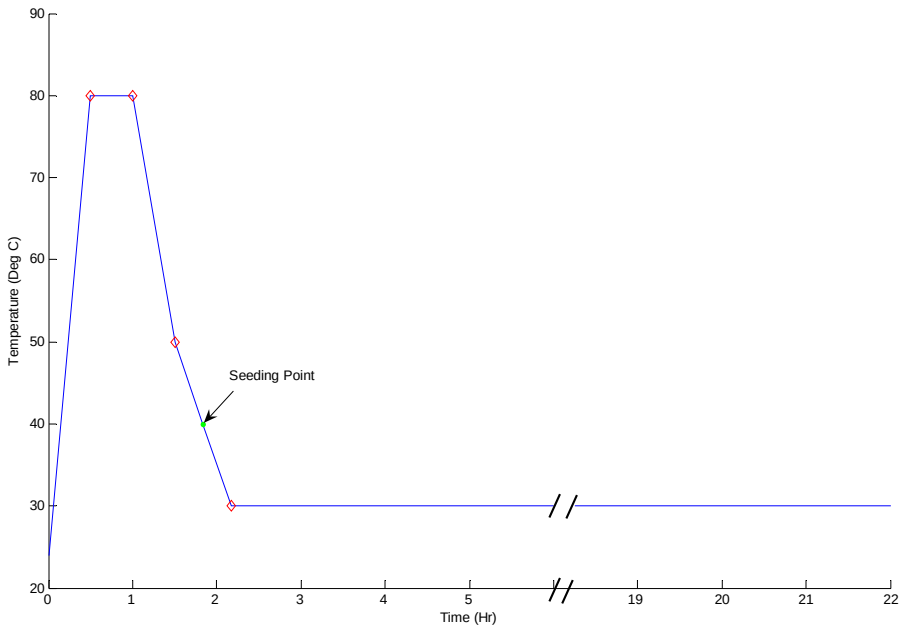

Figure 4.9. Temperature profile for MSG seeded crystallization process.

(A)

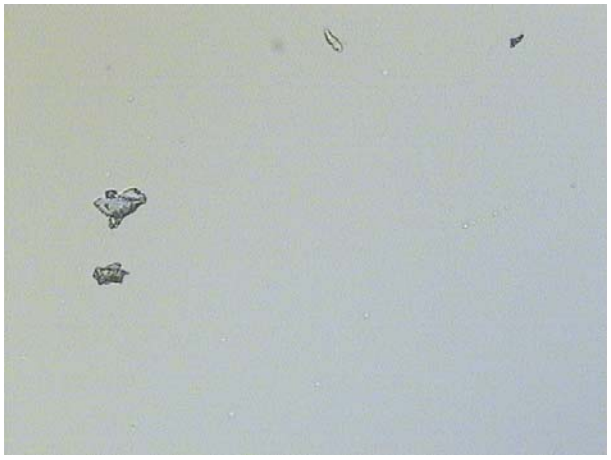

(B)

(C)

(D)

Figure 4.10. Microscopy images of prepared MSG seeds with 50X magnification.

PVM images are acquired throughout the experiment. The PVM was set to auto-adjust for light and contrast every minute. Without this adjustment, the images tend to get darker as the crystallization proceeds and more solids get formed in the solution. Occasionally, the PVM probe also had to be removed for cleaning.

As shown in Table 4.2, although every effort was made to maintain the same experimental conditions in all the runs (except Experiment X), differences were still apparent in the results of the experiments. The variations could have originated from the (manual) seeding step or unknown disturbances that affect the crystallization mechanism (Samant & O'Young, 2006). The variations became evident during the course of the experiment (e.g. difference in PVM image quality) and at the end of the crystallization (different amounts of final product). The variation could also be due to small changes in the positioning of the PVM probe, the stirrer, or their relative positions in the crystallizer.

Corresponding to Table 4.2, Fig. 4.11 to 4.15 depicts the PVM images acquired from different experimental runs of MSG seeded cooling crystallization process. The images are sampled at evenly-distributed time points based on the total process time of each experimental run.

Table 4.2 : Comparison of Different Runs of MSG Seeded Cooling Crystallization Experiments

Experiment No.	Seed Size (by sieve size) (μm)	Weight of Products (g)	Rate of Image Acquisition (image/sec)	Experiment Duration	No. of PVM Images
X	Not sieved	Not measured	2	22 hr 20 min	29,898
A	38-45	5.41	0.5	93 hr 41 min	51,141
B	38-45	7.2574	1	117 hr 36 min	62,129
C	38-45	15.9126	0.5	69 hr 22 min	42,304
D	38-45	14.6119	0.5	71 hr 14 min	43,156
E	38-45	Not measured	2	10 hr 27 min	61,007

4.3 Discussion

4.3.1 Comparison of Image Quality

Microscopy Images to PVM Images

As shown in Fig 4.3 and Fig. 4.5, there are obvious differences between microscopy and PVM images. Microscopy is an off-line measurement, where in the sample crystals are well separated on a static and flat surface. The image is clear and there is almost no noise effect on the measurements. Compared to microscopy images, the PVM images are less sharp, with non-uniform background, and have artifacts like ghost images. PVM is at a fixed position in the stirred slurry and randomly acquires process images at specific frequency. Only when crystals are within PVM's field of view, they can be imaged. The motion of the liquid solution and solid crystals, as well as the light illuminance of PVM probe, may cause the low quality of acquired

images.

PVM Images Acquired from Different Runs

When the images from Experiment X are compared with those from Experiment A to D, the images, as shown in Fig. 4.11, are quite clear. The contrast of crystal objects to background is quite high and the growth of the crystals (especially the long needle shape MSG crystals) is distinct. However, the PVM image acquired from Experiments A to D, as shown in Fig. 4.12, 4.13, 4.14 and 4.15 respectively, are not as clear as those taken from Experiment X. The images are relatively faded, the crystal objects are not clear in the images and there are many more darker clots or objects without clear edges. Specifically, images from Experiment X contain only needle shape (β form) MSG crystals which grow quite long by the end of the experiment (after 21 hours). However, the images from Experiment A to D contain not only needle- shape (β form) MSG crystals, but also rhombus-shape (α form) crystals. Furthermore, the particles obtained at the end of these experiments (from 66 hours to 116 hours) are not as big as those from Experiment X. The image quality, particle shape and size in Experiment A to D are quite different from Experiment X, one possible reason is the seeding particles are ground before adding to the processes in Experiment A to D. The grinding may modify the surface properties of the particle and lead to different particle growth kinetics.

PVM Images Acquired from the Same Run

During each MSG experimental run, the image quality varies with process time. As shown in Figures 4.11 to 4.15, the images that are acquired at the 1st hour of each experiment are almost blank, and contain very few small particles. With the progress

of each experiment, more particles are imaged and the quality of images gets poorer and poorer. The increase in solid concentration is suggested as the major reason for this. If there are more solids in the solution, the particles will have more chance to overlap or aggregate together to form particle clots. In a high solid concentration solution, there are too many particles around the lens of instruments and these particles may corrupt the image quality because they may be out of focus to be clearly imaged. The higher the solid concentration, the darker the images tend to be, since the external source of light is not able to get into the field of view for imaging - the illumination provided by instrument itself is not sufficient to take clear images.

To quantify this problem, Experiment X is selected as a case study. Fig 4.16 shows more PVM images that are acquired at different process times from Experiment X. It is obvious that the quality of image varies from the beginning to the end.

The histogram intensity value of each image in Fig. 4.16 is calculated and the results are shown in Fig. 4.17. It is obvious that the intensity values are confined to lower values as time progresses. Since intensity value 0 represents black and 255 represents white, it shows that the image is getting dark and blur and this is consistent with Fig. 4.16 as well.

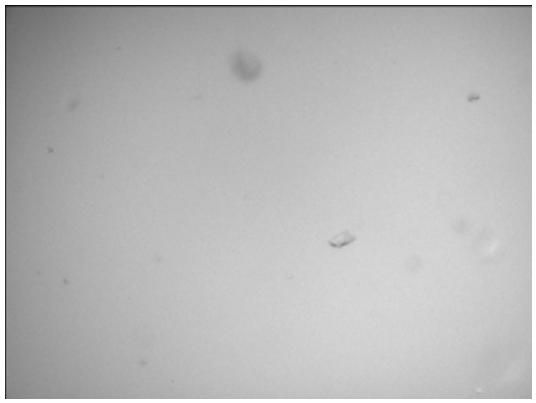

(a) 1st Hour (Image No. 2598)

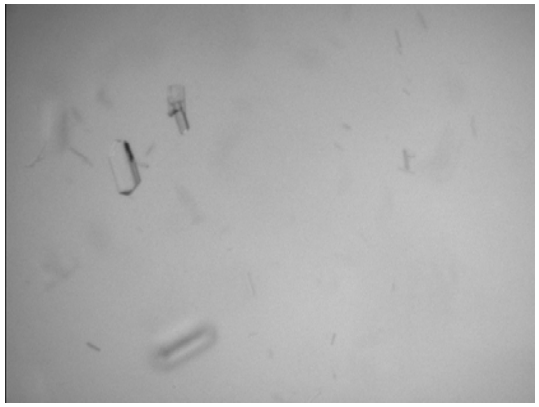

(b) 5th Hour (Image No. 13407)

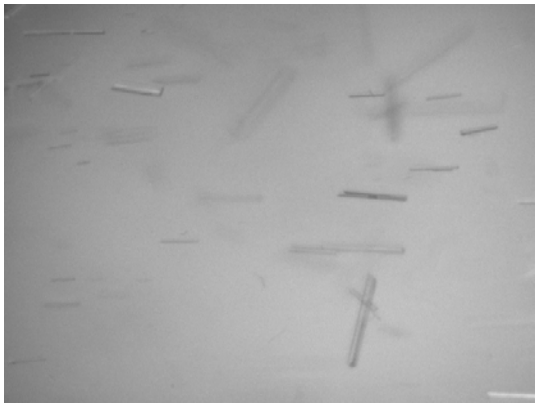

(c) 9th Hour (Image No. 19366)

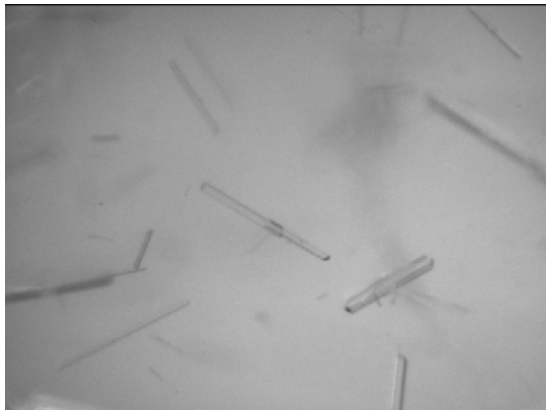

(d) 13th Hour (Image No.23804)

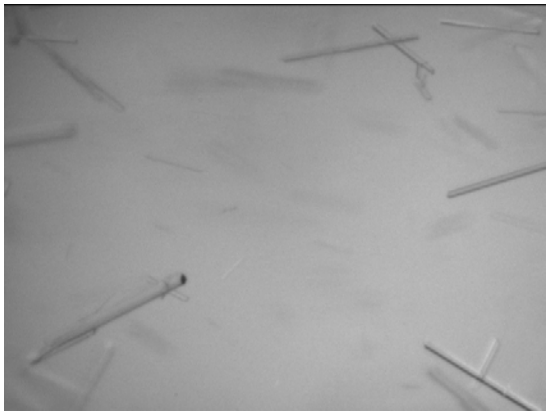

(e) 17th Hour (Image No.27336)

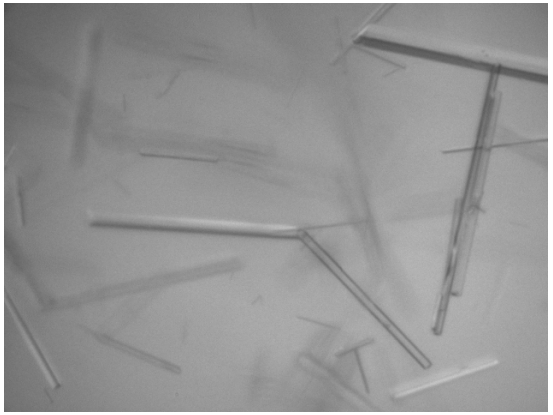

(f) 21st Hour (Image No.29272)

Figure 4.11. PVM images acquired at evenly-distributed process time from experiment X of MSG seeded cooling crystallization.

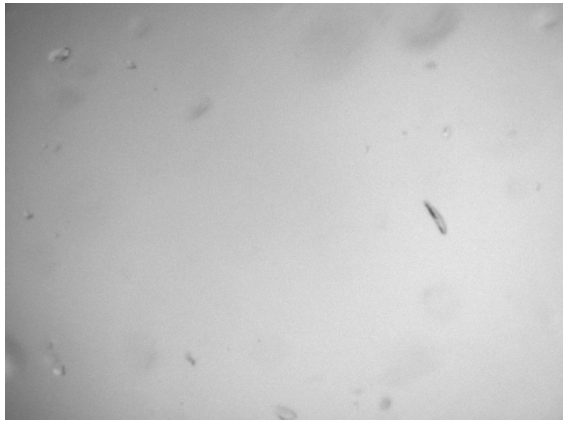

(a) 1st Hour (Image No. 1326)

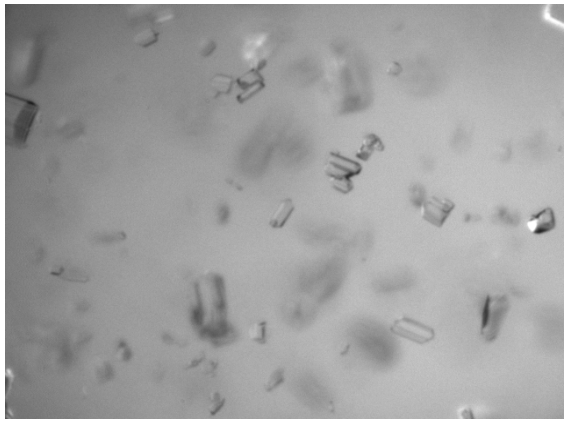

(b) 19th Hour (Image No.19473)

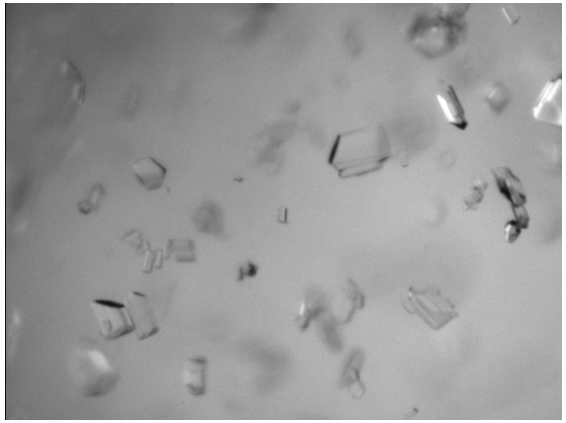

(c) 37th Hour (Image No.30172)

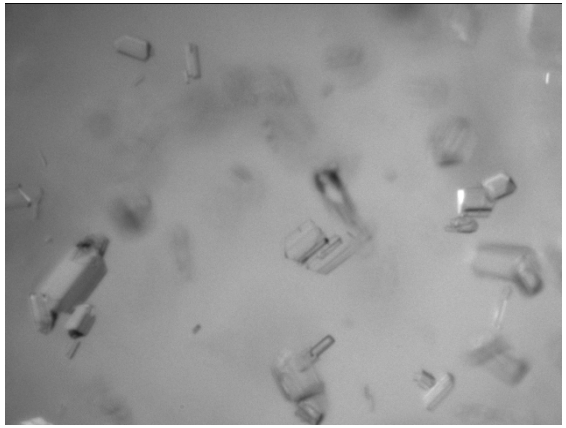

(d) 55th Hour (Image No.37960)

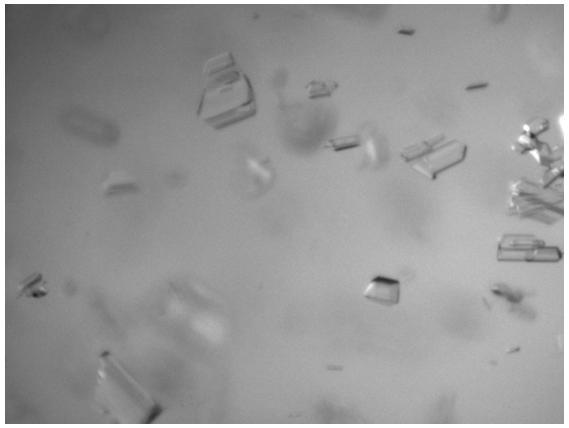

(e) 73th Hour (Image No.44726)

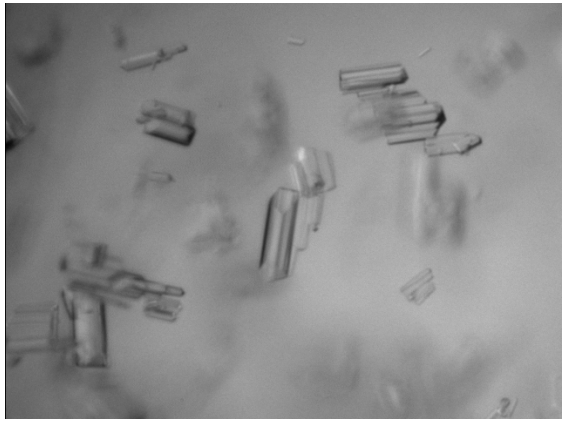

(f) 91st Hour (Image No.50315)

Figure 4.12. PVM images acquired at evenly-distributed process time from experiment A of MSG seeded cooling crystallization.

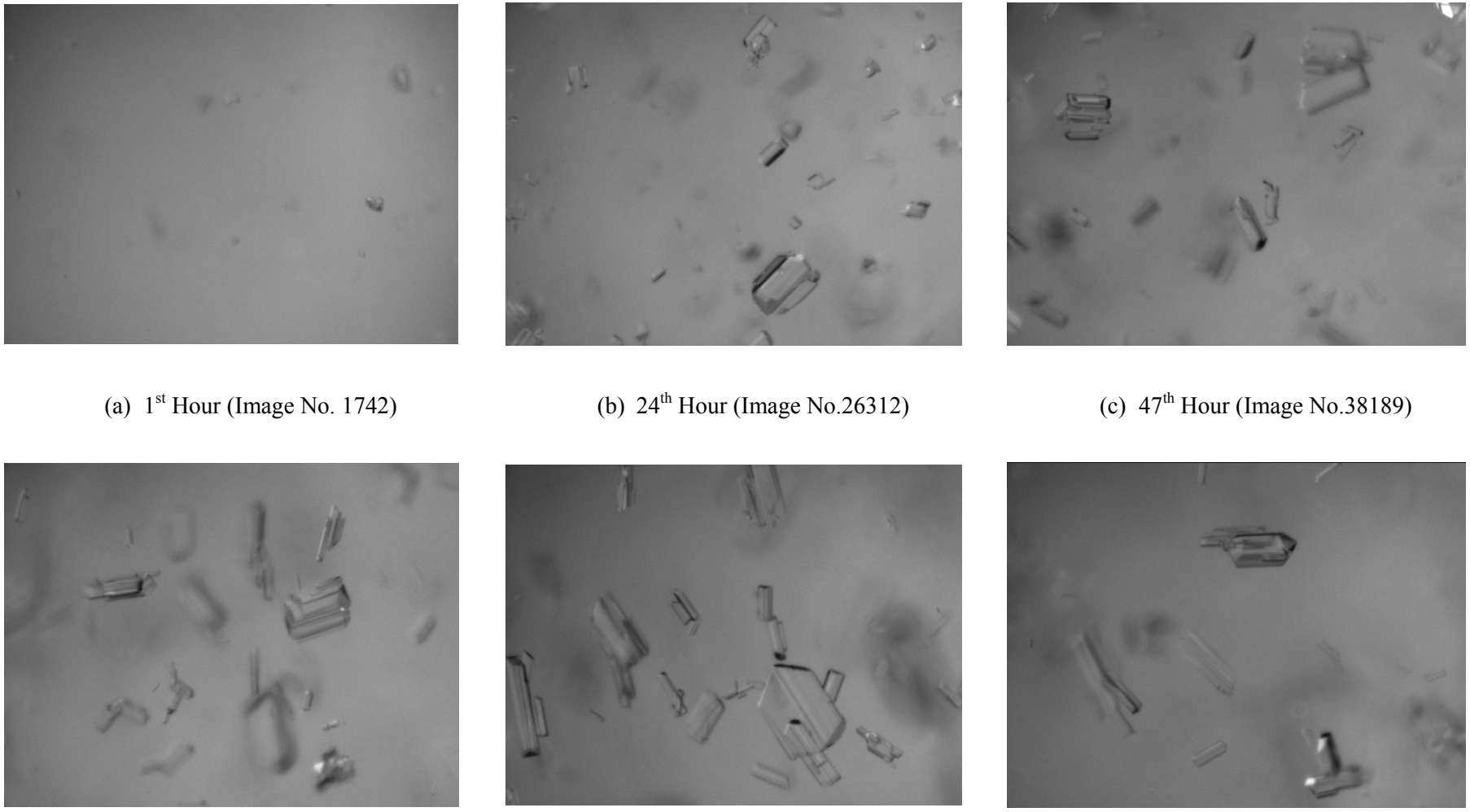

(a) 1st Hour (Image No. 1742) (b) 24th Hour (Image No.26312) (c) 47th Hour (Image No.38189)

(d) 70th Hour (Image No.47778) (e) 93th Hour (Image No.55610) (f) 116thHour(Image No.61727)

Figure 4.13. PVM images acquired at evenly-distributed process time from experiment B of MSG seeded cooling crystallization.

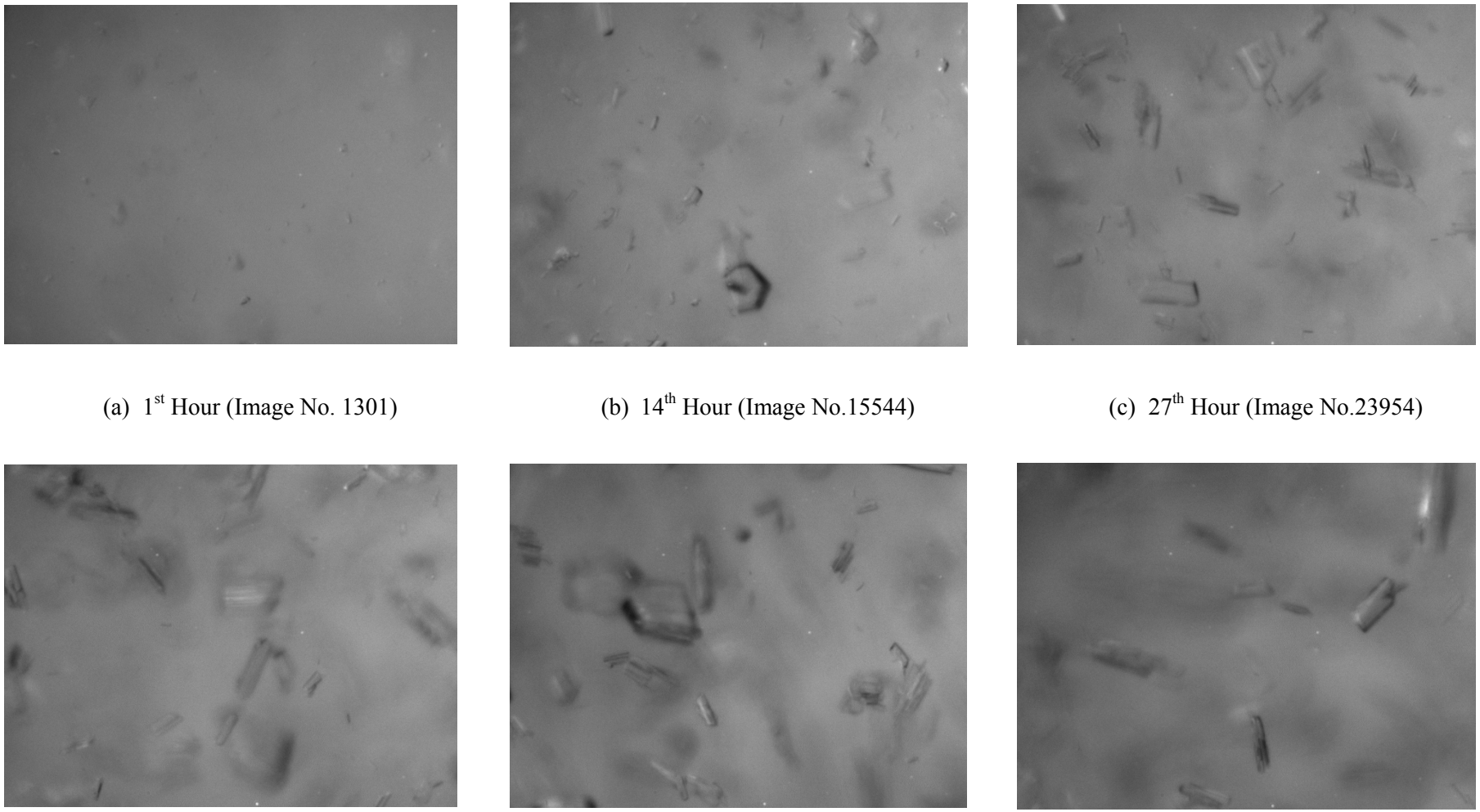

(a) 1st Hour (Image No. 1301) (b) 14th Hour (Image No.15544) (c) 27th Hour (Image No.23954)

(d) 40th Hour (Image No.30928) (e) 53th Hour (Image No.36299) (f) 66thHour(Image No.41081)

Figure 4.14. PVM images acquired at evenly-distributed process time from experiment C of MSG seeded cooling crystallization.

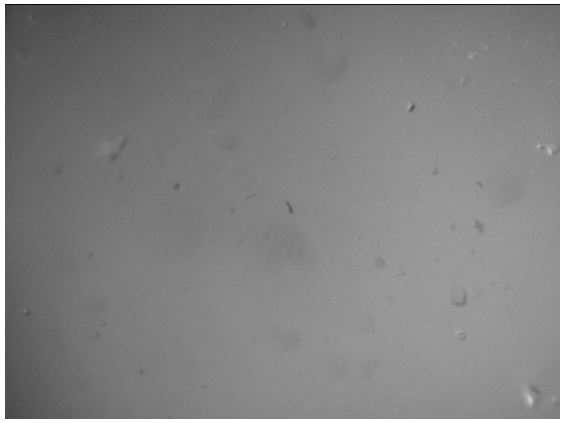

(a) 1st Hour (Image No. 1345)

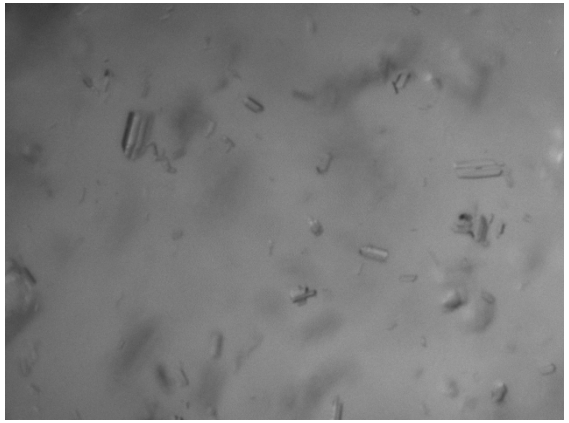

(b) 15th Hour (Image No.16668)

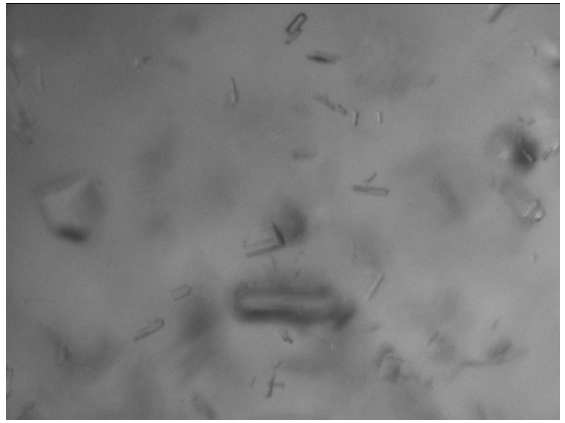

(c) 29th Hour (Image No.25236)

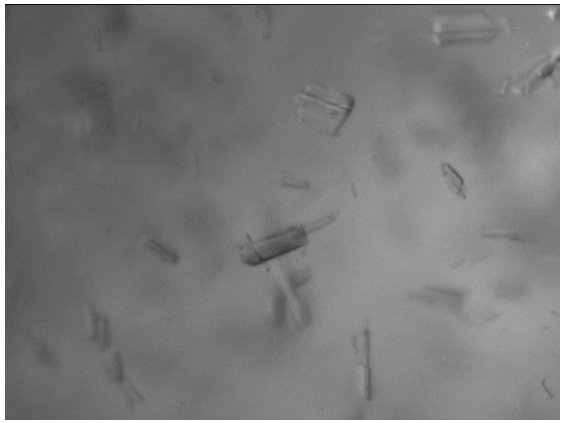

(d) 43th Hour (Image No.32136)

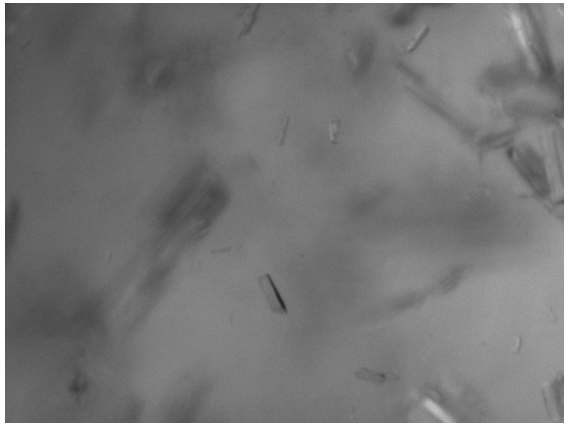

(e) 53th Hour (Image No.37786)

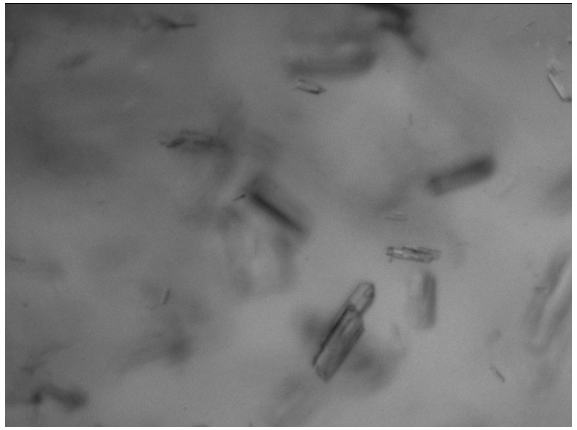

(f) 66thHour(Image No.43049)

Figure 4.15. PVM images acquired at evenly-distributed process time from experiment D of MSG seeded cooling crystallization.

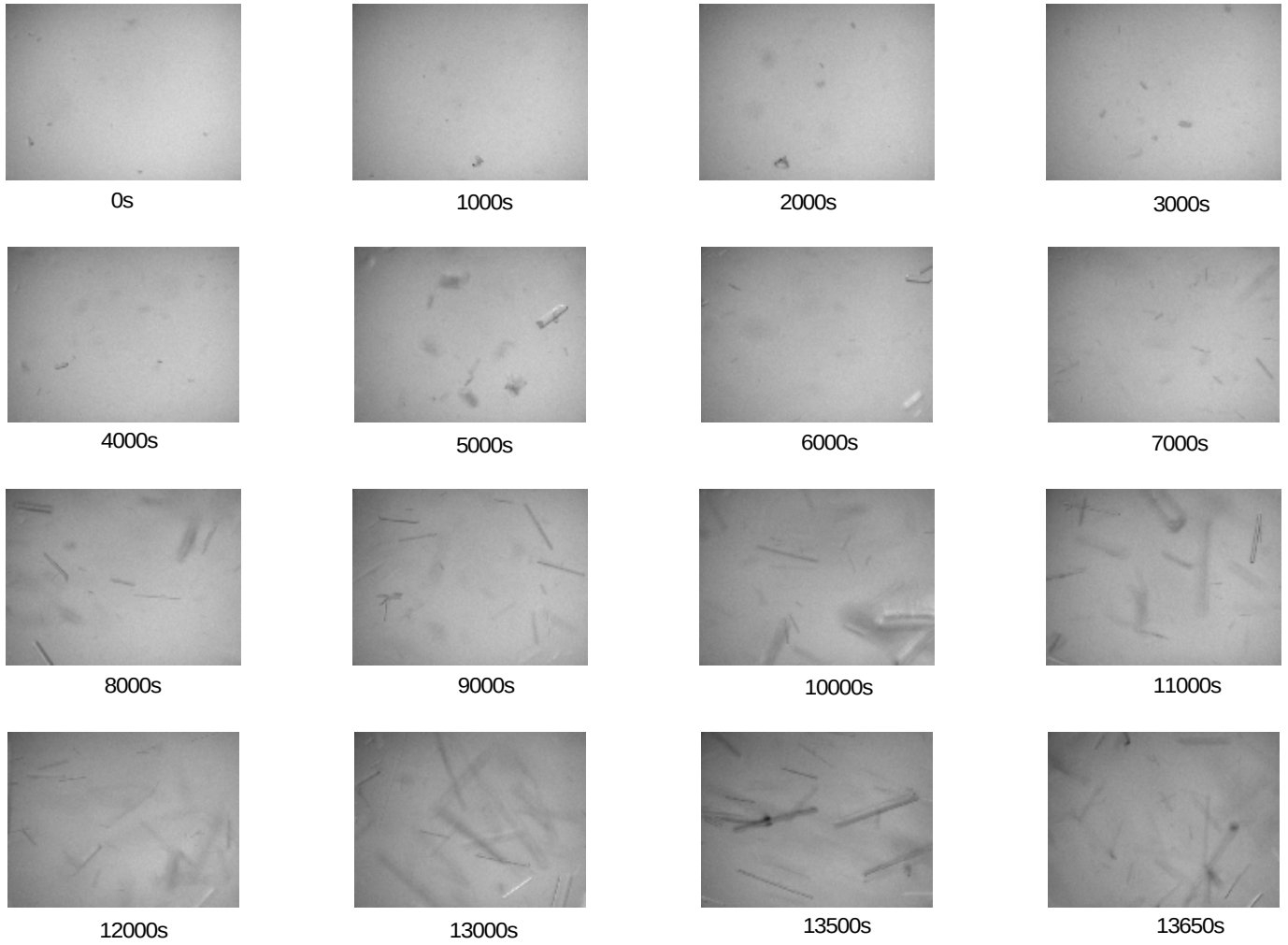

Figure 4.16. Time series PVM images acquired from experiment X.

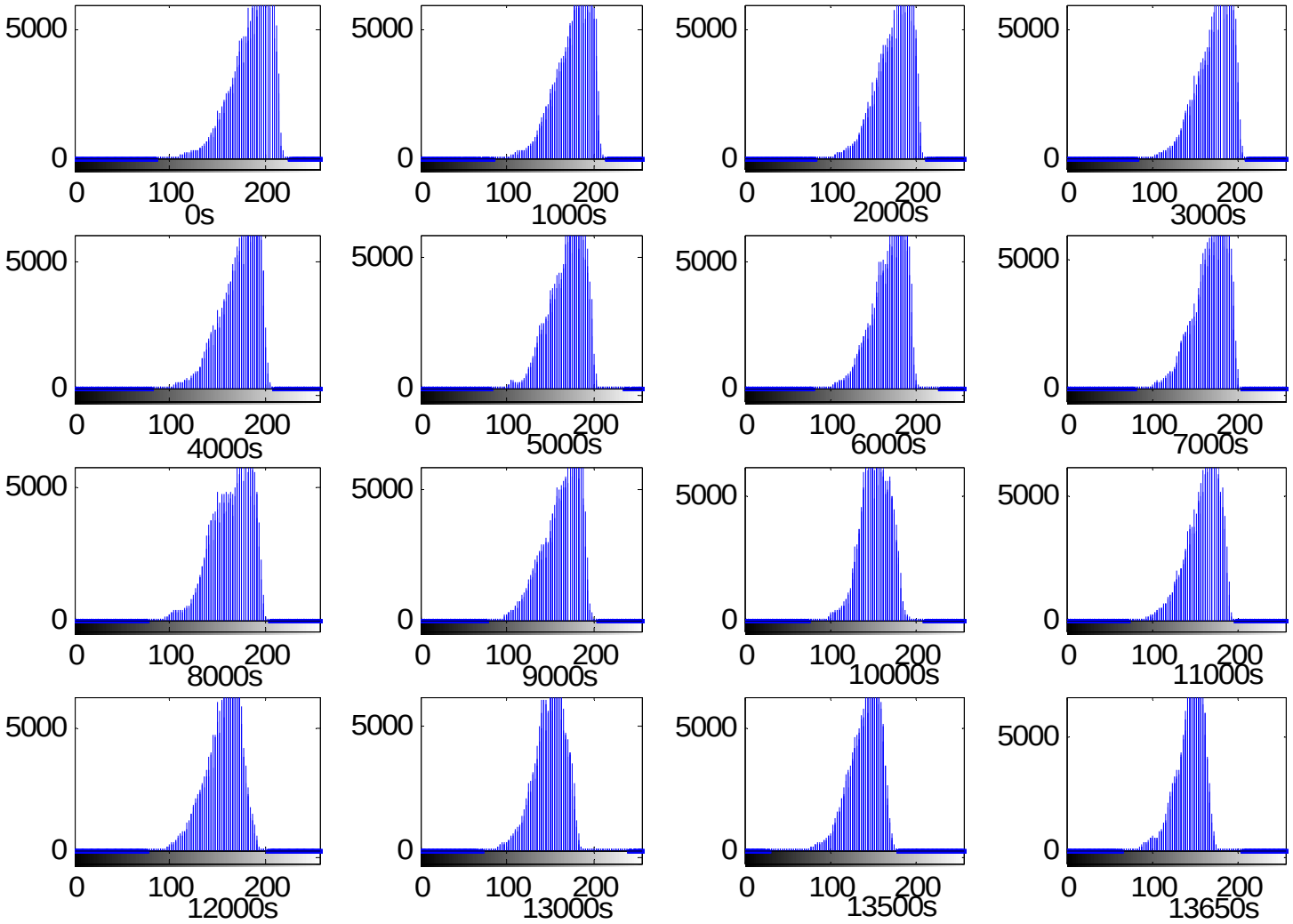

Figure 4.17. Intensity histogram variations corresponding to Figure 4.16.
(Horizon axis represents intensity values, vertical axis represents the counts)

Further quantification is based on the whole set of 29,898 PVM images that are acquired from Experiment X. The mean intensity value of each image in Experiment X is calculated, as shown in Fig. 4.18. It is obvious that the mean intensity value goes down as the experiment progresses. This is consistent with the results shown in Fig. 4.16 and 4.17 and indicates that the images get darker and blurred.

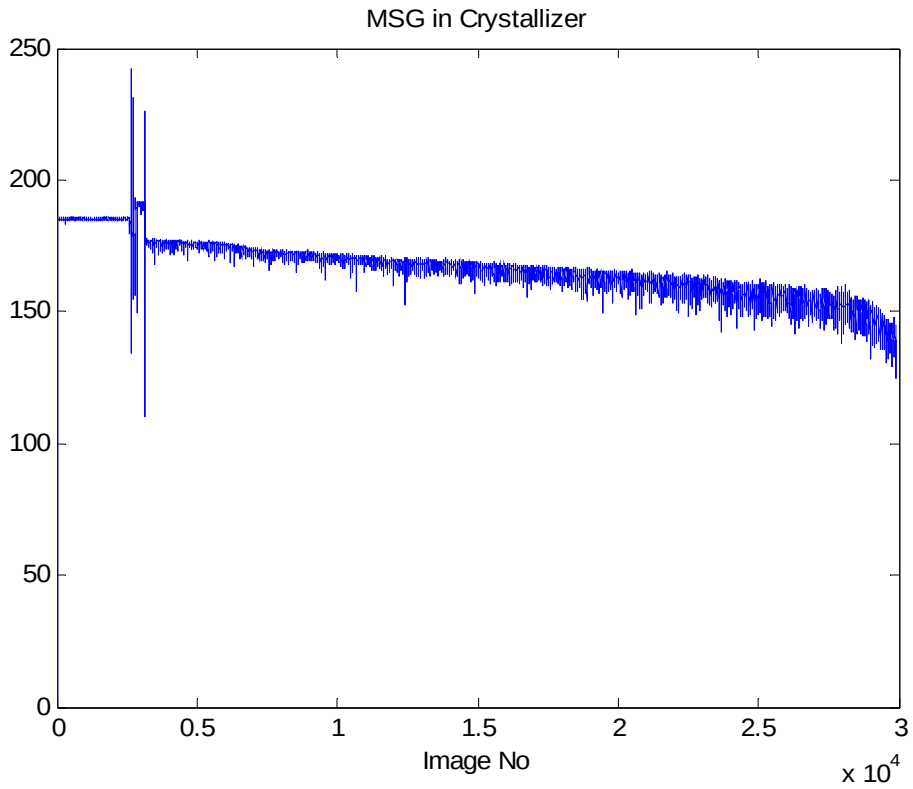

Figure 4.18. Mean intensity variations with time corresponding to experiment X.

4.3.2 Speed of PVM Imaging

With image-based methods to quantify particle size distribution, if more particles are segmented in a certain time window, a higher accuracy in system characterization can be achieved. Hence the fastest possible image acquisition speed is desirable. PVM is stated to have a maximum image acquisition speed of 10

images per second. With different settings of image acquisition speed for each MSG experiment (as listed in Table 4.2), the number of images that are collected in each hour is plotted in Fig. 4. 19. It is observed that in the first few hours, with higher speed setting, more images are collected. However, for all settings of image acquisition speed, the number of acquired images drops dramatically with time going on. After 5 hours, any of the settings may collect more or less the same number of images per hour and it reaches a value of about 500 images per hour after 40 hours of process time.

Furthermore, the performance of each setting is studied. As an example, when the image acquisition speed is set to 2 images per second, 7,200 images are expected to be collected for each hour. It is observed that during the first hour, only about 4,400 images are collected and this means a "performance" of about 60%. The hourly performances of different settings are plot in Fig. 4.20. It is obvious that lower setting of image acquisition speed results in higher hourly performance. Also, all the hourly performances drop dramatically after the first 20 hours and stabilize at the 10% to 20% performance level.

The above studies indicate that PVM is able to collect and store reasonable number of images and has acceptable performance during the first few hours of image acquisition. Both the number of collected images and the hourly performance drop dramatically and reach to unsatisfactorily low values after 20 to 40 hours of non-stop image acquisition. This may be considered as the main limitation of PVM usage as an inline measuring instruments.

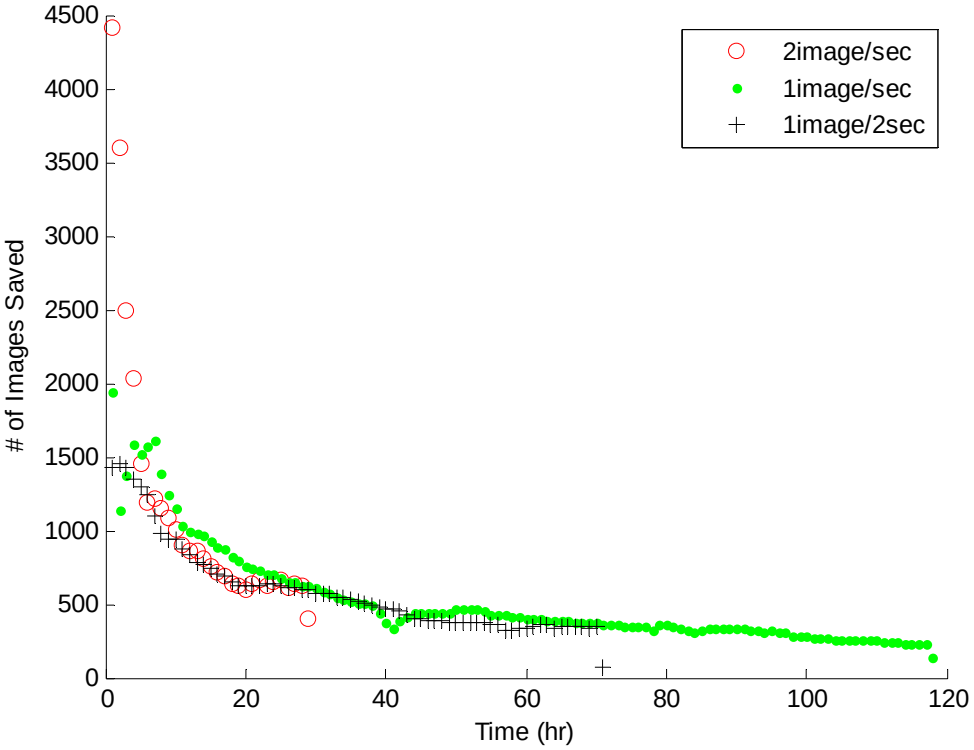

Figure 4.19. Number of images acquired in each hour with different settings of image acquisition speed.

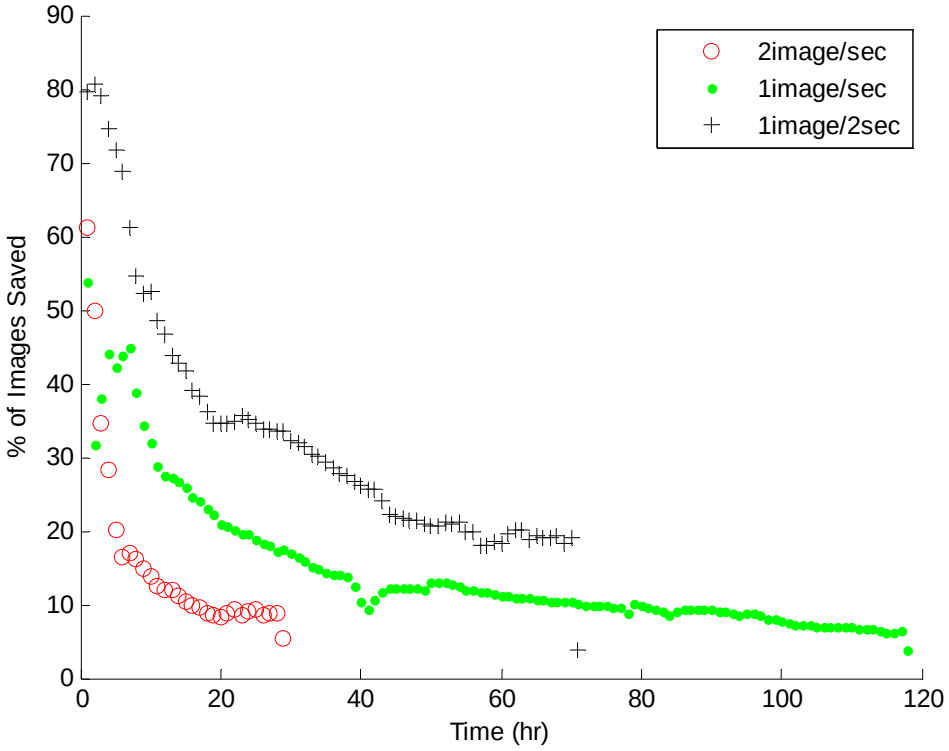

Figure 4.20. Hourly performance with different settings of image acquisition speed.

4.4 Conclusion

This chapter described the experimental setup and the two experiments that were conducted with it. Five sets of sea sand samples with different ranges of particle sizes in DI water were studied to compare the measurements made with PVM and microscope. In addition, seeded cooling crystallization experiments of MSG were conducted to monitor the particle growth.

PAT instruments were used to gather process information in real time from the experiments. ATR-FTIR predicts solution concentration from the collected spectrum, FBRM directly measures the chord length of particles and PVM acquires process images that contain many individual particles. Despite its usefulness, the quality of PVM images varies from one to another run of experiment. Even within one run of experiment, the quality of the images tends to vary from the beginning to the end of the experiment. These measurements and characterizations are expected to provide more detailed information to enable better process monitoring and control.

Chapter 5. Metrics for Evaluating PVM Imaging System and IA Methodology

None of the available process imaging systems or proposed image analysis approaches is applicable to all processes. Different methodologies are more or less suitable for a particular application. It is therefore necessary to evaluate the PVM imaging system and IA methodology for application in crystallization processes.

There are three general evaluation methods: analytical, empirical goodness and empirical discrepancy (Zhang, 1996 & 2006; Mao & Kanungo, 2001; Martin et al., 2001). Analytical methods usually require formal models of an image and priori-knowledge, such as processing strategy, processing complexity and efficiency and segmentation resolution. These methods directly qualitatively examine and assess the segmentation algorithms themselves. Empirical goodness methods subjectively evaluate and assess segmented images according to human intuition. Typical goodness measures are intra-region uniformity, inter-region contrast, and region shape. For example, images that are segmented correctly should have intra-region uniformity and high inter-region contrast. Empirical discrepancy methods require an ideal segmentation as reference and find the discrepancy between the reference and the actual segmented images to evaluate and assess image segmentation algorithms.

When these three evaluation methods are compared, the analytical methods are simple, direct and fast, but require priori-knowledge and formal models, which are not always available. The empirical goodness methods are reliable only when suitable goodness measures are properly selected. For complex process images, it is hard to define such goodness measures. The empirical discrepancy methods are objective and quantitative and provide precise result except the influence of human factors. But these are complex and require manual or automatic reference segmentation that presents the ideal or expected results.

Empirical discrepancy methods are the most reliable despite their complexity. In this thesis, one such method is used to evaluate the PVM imaging system and IA methodologies. Manual segmentation is considered as the ground truth and used as the reference to evaluate IA methodology. Manual segmentation is reliable and accurate, but cumbersome. It is known that segmentations of the same image by different persons, even the same person at different times, may be different, but the statistical results of manual segmentations for a wide variety of images are highly consistent (Martin et al., 2001). From each set of PVM images acquired from sea sand experiments (as described in Section 4.2.1), about 1000 are selected for manual segmentation. The manually segmented particles are used as a reference template for evaluating the PVM imaging system and IA methodology.

In Section 5.1, the evaluation criteria of Extent of Matching and Cumulative Error are mathematically defined. Section 5.2 evaluates the PVM imaging system and IA methodology based on the five sets of sea sand experiments (as described in Section 4.2.1). In the experiments of sea sand in DI water, there is no variation of particle

size and shape through the process time. Firstly, the PVM imaging system is evaluated with microscopy measurements. The median particle sizes that are obtained from microscopy measurements are compared with those from manual segmentation of PVM images. Secondly, the IA methodology is evaluated with manual segmentation using the evaluation metrics that are defined in Section 5.1. Lastly, the conclusions are given in Section 5.3.

5.1 Metrics for Evaluating IA Results

We evaluate the accuracy of IA results from PVM images through manual segmentation of the particles. A human operator enables the size estimation by segmenting the particle(s) visible in the PVM images. Specifically, the operator locates the particle outline in the image, as shown in Figure 5.1. We evaluate the similarity of the size estimates to quantify the accuracy of the IA results where the algorithm automatically segments the particles from the PVM image. Here, we propose metrics for evaluating the similarity between automated and manual segmentation.

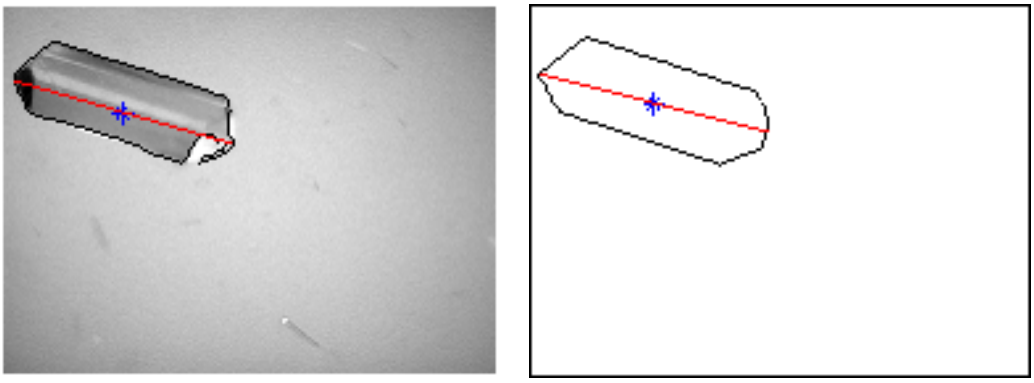

(a) (b)

Figure 5.1. Segmentation of a MSG particle
by (a) image analysis, and (b) human operator.

An identified particle, irrespective of whether it is segmented manually or through the automatic image analysis algorithm, will have an outline which consists of a series of (x, y) values of the boundary pixels. However, the set of particles identified in the two segments may not completely match, i.e., certain particles in the manual segmentation may not be identified by the IA or vice versa – hence a direct comparison would be erroneous. Therefore, to estimate the quality of IA segmentation, two related problems have to be solved: (1) establishing the particles that have been identified in both segmentations, and (2) estimating the difference in particle lengths calculated from the two segmentations. We solve the first problem by recognizing that when both the manual and IA segmentations detect the same particle in an image, the particle centroid should be similar (within a small distance of each other), as described in detail below. Based on this, for the second problem, we propose metrics to quantitatively measure the agreement between the two segmentations.

Consider an image G with several particles that have been segmented by two different approaches – denoted as A and B – resulting in two different sets of particles S_A and S_B. Each set contains the outlines of the constituent particles. Consider a particle p in S_A described by its outline o. o is an ordered set of the coordinates (2-d) of the pixels that form the outline of p. Let the number of pixels in o be n. So

$$o = \left[\ell_1, \ell_2, \ldots \ell_i, \ldots \ell_n\right] \tag{5.1}$$

$$\ell_i = \left[\ell_i^x \quad \ell_i^y\right]^T \tag{5.2}$$

where, ℓ_i^x and ℓ_i^y are the x- and y- coordinates of the i^{th} outline pixel ℓ_i. The

distance between two pixels can be measured by the Euclidean distance between them.

$$d(\ell_i, \ell_j) = \sqrt{(\ell_i^x - \ell_j^x)^2 + (\ell_i^y - \ell_j^y)^2} \tag{5.3}$$

The length of particle p, in the sense of maximum chord length, as calculated from outline o, can be defined as:

$$\|o\| = \max_{\forall i,j} \{d(\ell_i, \ell_j)\} \tag{5.4}$$

The position of p as calculated from outline o can be characterized by the centroid as:

$$\hat{o} = \frac{1}{n}\sum_i \ell_i = \left[\frac{1}{n}\sum_i \ell_i^x \quad \frac{1}{n}\sum_i \ell_i^y\right]^T \tag{5.5}$$

In this work, the length $\|o\|$ and location $\hat{o}$ of the particle as derived from its outline, completely characterize the particle. Other attributes such as the angle of the major axis can also be included, if necessary. This characterization enables the systematic comparison of particles identified by the two segmentations.

Two particle outlines, o_1 and o_2, from different segmentations of the image, can be said to *correspond* if:

$$\frac{d(\hat{o}_1, \hat{o}_2)}{\|o_1\|} \le \delta \tag{5.6}$$

where, δ is an user-defined threshold. Since larger particles would have larger offset in the centroid, the above equation includes a normalization based on the length of the particle. All corresponding particles can be identified in an image, as well as all images in a set. If a total of S_A particles have been segmented by approach A and S_B particles by approach B, a subset of S_{AB} particles may be found

to correspond.

$$S_{AB} \le \min\left(S_A, S_B\right) \tag{5.7}$$

A quantitative measure of correspondence is given by the *extent of matching*, defined as the percentage of particles in a segmentation with corresponding particles in the other segmentation:

$$M_A = \frac{S_{AB}}{S_A} \tag{5.8}$$

S_{AB} and M_A are dependent on the choice of δ as shown in Chapter 6. A high extent of matching indicates that most of the particles identified by the manual segmentation is also located by IA.

For any particle p that has corresponding outlines in the two segmentations, the *error* in the length estimate is given by:

$$\varepsilon_p = \left| \frac{\|o_1\| - \|o_2\|}{o_1} \right| \tag{5.9}$$

Statistical properties such as median error can be calculated from the errors of all corresponding particles in the two segmentations of image *G*:

$$E_G = \underset{p \in G}{median}\left(\varepsilon_p\right) \tag{5.10}$$

Similarly, the *cumulative error* can be calculated from all the images in the set.

$$E = \underset{\forall G}{median}\left(E_G\right) \tag{5.11}$$

A small cumulative error indicates a close match between the particle size results from IA. Next, we experimentally evaluate the accuracy of the PVM imaging system and the IA methodology.

5.2 Evaluation of PVM Imaging System and IA Methodology

First we evaluate the accuracy of the PVM imaging system by comparing the microscopy and the manual segmentation of the PVM images. For this purpose, about 165 PVM images were randomly selected by the operator to manually build templates. These templates contained about 200 particles. Table 5.1 lists the median particle sizes and standard deviation for the five sets as estimated by the various measurement methodologies. As expected, the microscopy measurements correctly show that the particle sizes increase from Set A to Set E. The measurements from the manual segmentation of PVM images also demonstrate the same trend. It is noticed that the PVM measurements are always smaller than those from microscopy, and the difference between these two measurements increases with particle size (with mean and median values of the difference about 11% and 12.5%, respectively). This is to be expected since during PVM imaging, sea sand is moving in the crystallizer and is oriented randomly vis-à-vis the PVM probe. Since the PVM may image a particle from any perspective, the particle's biggest chord length may not be visible in the resulting 2-d image, thus leading to under-estimation of particle size. Multiple PVM probes can help us to get a better estimation of particle size distribution. However, even this may not completely overcome the under-estimation of particle size. The under-estimation problem is a key shortcoming of PVM that may be overcome by correlating PVM measurements with microscope measurements. Both methodologies have similar standard deviation indicating a systematic error across the particle size range. The consistency in the measurements

from microscopy and manually segmented images indicates that as an imaging system, the PVM is a reliable tool to estimate particle size.

As discussed in Section 2.2.4, although microscopy yields high accuracy, it is limited to off-line measurements and cannot be used as an in-line instrument to estimate particle size in real-time. Also, manual segmentation is tedious and is impractical for large-scale real-time applications. Automated image analysis of PVM images to yield size estimates is therefore essential. So, we evaluate the accuracy of the IA methodology to estimate the particle size from PVM images by comparing it with the manual segmentation.

Table 5.1: Size Estimates of Sea Sand Particles using Microscopy and Image Analysis

Evaluation Methodology	**Set A**	**Set B**	**Set C**	**Set D**	**Set E**
Sieve Size in μm	53 - 75	75 - 90	90 - 106	106 - 125	125 - 150
Microscopy Median (Std) in μm	130 (27)	174 (35)	208 (34)	231 (34)	260 (43)
Manual Segmentation of PVM images Median (Std) in μm	123 (34)	153 (41)	182 (41)	202 (38)	225 (40)
Difference between Microscopy & PVM imaging	5.4%	12.1%	12.5%	12.6%	13.5%
Image Analysis of PVM images Median (Std) in μm	116 (47)	135 (58)	160 (63)	190 (71)	190 (87)
Error of IA to Template (%)	3.8	2.1	2.1	1.7	2.2
Extent of Matching (%)	89.3	94.5	91.1	94.8	93.3

The IA methodology automatically processes all the PVM images and identifies thousands of particles for each set. It also finds the particle size to be increasing from Set A to Set D. Most of the manually segmented particles (92.6%) could also be identified by the IA methodology. A one-on-one comparison based on these matched particles show that the measurements from IA are almost the same as those from the manual segmentation (difference of about 2.4%). The median size of the IA results for Set E breaks the trend. A visual inspection of the IA segmentation reveals incorrect segmentation of big particles into several small ones in all sets, possibly due to background noise in the image, thus leading to a decrease in the median particle size. This leads to the higher standard deviation of the IA results as well. However, when these sub-particles are ignored, as is done in the calculation of the cumulative error, the results are acceptable. Overall, it can be concluded that the IA methodology can reasonably estimate particle size.

5.3 Conclusion

In this chapter, we have focused on the accuracy of the results which can be obtained from image analysis. We have shown that there is a noticeable difference between the true particle size as seen under the microscope and that extracted from PVM images even with the human eye. PVM images lead to an estimated particle size that is about 11% less than that obtained from microscopy analysis, possibly because of the random orientation of the particles during in-situ imaging. While this is a significant measurement error, it should not obviate particle size identification using PVM because of the numerous benefits and potential advanced control applications that easy, real-time size measurements would entail.

We have also sought to quantify the errors introduced by automated image analysis. Basic image analysis is well-established in literature, however, its accuracy in any application depends highly on various parameters that have to be pre-specified by the user. We have used manual segmentation of the image as a basis for evaluating the results from automated image analysis. We have proposed two metrics – extent of matching and cumulative error – to compare automated and manual segmentations. These serve as a quality measure to evaluate the effect of various parameters. Our results with 5 sets sea sand images have shown that 92.6% of the manually segmented particles could be identified by IA methodology, which leads an error about 2.4% in estimating particle size.

Chapter 6. Evaluation of IA Methodology for Real-Time Monitoring of Particle Growth in Seeded MSG Crystallization

This chapter further evaluates the IA methodology using a manually segmented template. In contest to Chapter 5, the experiments in this chapter are based on real crystallization processes, where the particles grow with time. As discussed in Section 2.4 and chapter 3, image analysis incorporates several steps, each of which require certain parameters to be specified by the user. The choice of parameter settings can considerably affect the resulting particle segmentation. The first section presented in this chapter focuses on quantitatively studying the effects of the different parameters on IA performance and identifying the best set of parameters for good particle segmentation leading to more accurate particle size estimation. In the second section, the obtained optimal parameters were applied to monitor the particle growth in seeded MSG crystallization process.

6.1 Effect of Image Analysis Parameters on PSD Estimates

Quantitative study of the effects of the parameters on the resulting quality metrics proposed in Section 5.1 is taken up here. For this, the PVM images from Experiment

X (as described in Section 4.2.2.2 and Table 4.2) were manually segmented. Two operators identified clear particles in the PVM images and located their outlines to build two independent templates. Template 1 consists of 2781 images out of a total of 29,898 PVM images collected during the run. These images were selected evenly from different times in the course of the experimental crystallization run. 4970 particles were manually segmented from these images. The other operator developed a more comprehensive Template 2, segmenting 69,048 particles from 25,352 images. The two templates give us the particle size information as evident to the human eye – the results from the automated IA methodology are benchmarked against these.

Fig. 6.1 shows some examples of IA, Template 1 and Template 2 segmentation as applied to the same PVM images. It is noticed that IA segments much more particles than the two manual templates. Template 1 segments only a few big and clear particles, while Template 2 segments all clear particles regardless of the particle size.

The effects of ten IA parameters were studied: intensity range and lowest pixel threshold during the image selection step; low threshold, high threshold and sigma from the canny edge detection step; the four structuring elements during morphology operations on the image; and the area threshold during the particle selection step. The effect of varying each of these was studied while keeping the others constant as summarized in Table 6.1.

The intensity range and the lowest pixel threshold parameters lead to a PVM image

being selected for further processing only when their values exceed a pre-defined threshold. These can be set to any integer between 0 and 255, the intensity range of grey-scale images. We varied the intensity range from 100 to 150, and the lowest pixel threshold from 90 to 255. In the corresponding image analysis results, the cumulative error varied from 31.4% - 33.3%, and the extent of matching from 34.9% - 66.0% which shows that the two parameters do have an effect on image analysis results.

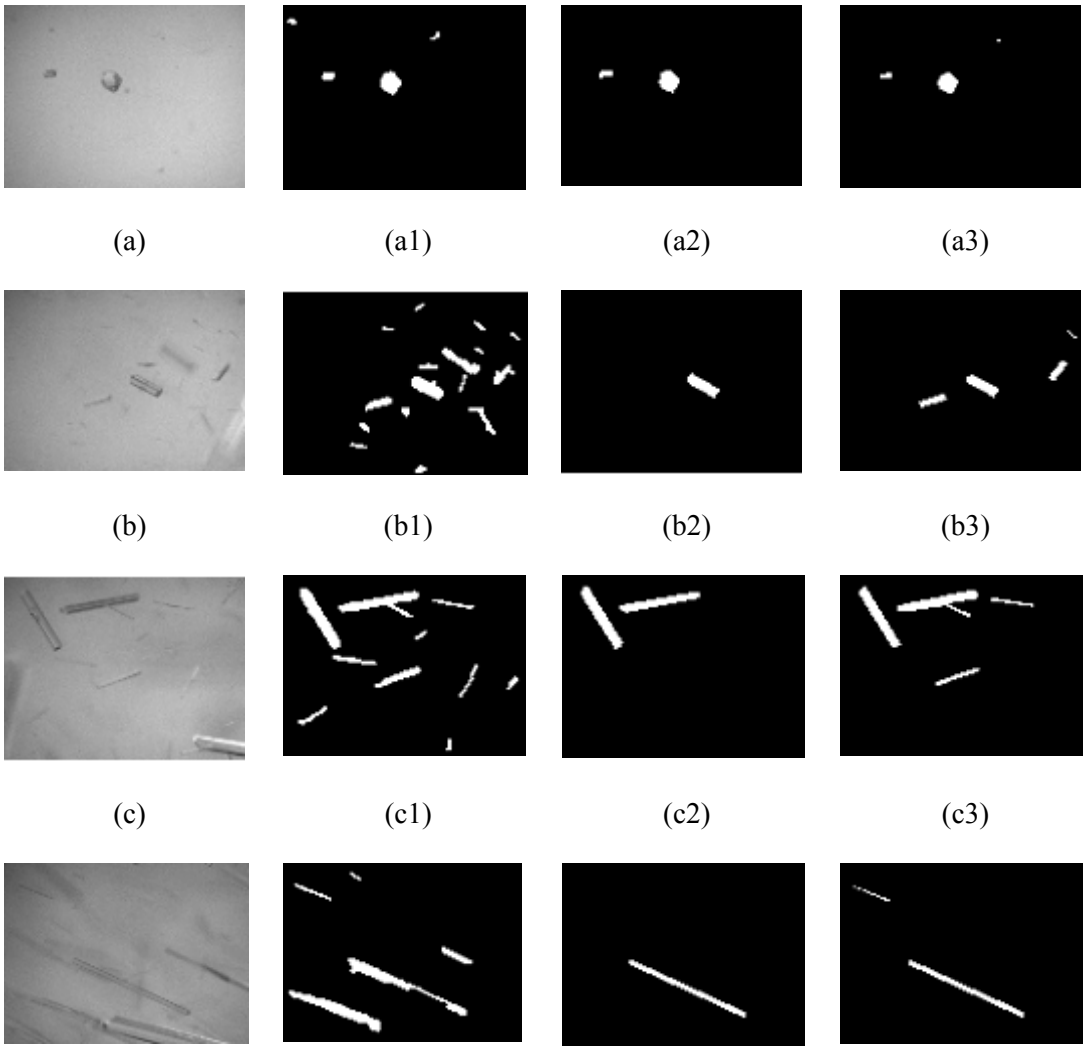

Figure 6.1. Examples of IA, Template 1 and Template 2 segmentation of the same PVM images (a)-(d) original PVM images acquired at the 1st, 6th, 11th and 22nd hours of Experiment X ; (a1)-(d1) corresponding IA segmentation; (a2)-(d2) corresponding Template 1 segmentation; (a3)-(d3) corresponding Template 2 segmentation.

Table 6.1: Effects of IA Parameters on Image Analysis Performance

	IA Step	Tuned Parameters	Value Range	Fixed Parameters	Cumulative Error (%)	Extent of Matching (%)
1	Image Selection	Intensity Range	100-150	Canny = ([0.1 0.2], 2) Se1 = (Diamond, 15); Se2 = (Square, 15)	31.4-33.3	34.9-66.0
		Lowest Pixel Threshold	90-255	Area Threshold = 200 Without adaptive histogram equalization step		
2	Canny Edge Detection	Low Threshold (Canny-T1)	0.01-0.2	Intensity Range = 120 Lowest Pixel Threshold = 200	30.2-52.8	26.4-83.6
		High Threshold (Canny-T2)	0.05-0.6	Se1 = (Diamond, 15); Se2 = (Square, 15) Area Threshold = 200		
		Sigma (Canny-Sigma)	1 – 3	Without adaptive histogram equalization step		
3	Morphology Operation	Structuring Elements for Morphological Operation, SE1 & SE2 (SE1-Shape, SE1-Size SE2-Shape, SE2-Size)	See Table 6.2	Intensity Range = 120 Lowest Pixel Threshold = 200 Canny = ([0.1 0.2], 2) Area Threshold = 200 Without adaptive histogram equalization step	8.0-60.5	0.5-94.3
4	Particle Selection	Area Threshold	100-800	Intensity Range = 120 Lowest Pixel Threshold = 200 Canny = ([0.1 0.2], 2) Se1 = (Diamond, 15); Se2 = (Square, 15) Without adaptive histogram equalization step	22.7-31.9	56.0-65.3

Table 6.2: Effects of Morphology Structuring Elements on Image Analysis Performance

	Parameter		Result	
	SE1	**SE2**	**Cumulative Error (%)**	**Extent of Matching (%)**
1	Diamond 15	Square 1	9.0	80.9
2		Square 2	9.1	82.9
3		Square 3	9.0	83.2
4		Square 4	8.9	83.5
5		Square 5	9.0	84.0
6		Square 10	19.3	71.7
7		Square 20	43.4	54.2
8	Square 15	Diamond 5	16.4	76.0
9		Diamond 10	35.9	61.1
10		Diamond 20	47.9	24.6
11	Line 10, 45	Square 5	13.2	85.0
12		Square 10	45.9	52.1
13		Square 15	54.5	34.5
14		Square 20	55.3	19.0
15	Line 5, 45	Square 15	22.1	4.8
16		Square 5	14.5	45.9
17	Square 15	Line 10, 45	10.4	82.4
18	Diamond 5	Square 15	47.1	49.6
19	Diamond 10		36.8	62.5
20	Diamond 20		29.6	65.3
21	Square 5	Diamond 15	42.7	5.7
22	Square 10		48.6	31.9
23	Square 15		46.1	40.6
24	Square 20		45.8	46.3
25	Square 5	Line 5, 45	11.7	78.2
26	Square 15		8.0	84.9
27	Diamond 5	Square 5	9.1	88.6
28	Square 5		12.4	78.3
29	Diamond 10		8.3	86.8
30	Diamond 20		10.3	80.9

(Other parameters are Area Threshold=200, Intensity Range = 120, Lowest Pixel Threshold=200, Canny parameter=([0.1 0.2], 2), and without adaptive histogram equalization)

Among the three parameters used in Canny edge detection, the first two are the low and high threshold values to detect an edge, and can be defined as any real number in the range [0 1]. The third parameter is the standard deviation, σ of the Gaussian

filter. We varied the low threshold from 0.01 to 0.2, the high threshold from 0.05 to 0.6 and σ from 1 to 3. In the corresponding image analysis results, the cumulative error varied from 30.2% to 52.8%, and the extent of matching from 26.4% to 73.6% indicating that these Canny Edge Detection parameters have a considerable effect on image analysis results.

There are many choices for the four structuring elements in the image opening and closing operations of the morphology operation step, as described in Section 2.4.2. We selected 30 combinations as listed in Table 6.2. It was noticed that the cumulative error ranged from 8.0% to 55.3% and extent of matching from 4.8% to 88.6%. This shows that the four structuring elements in the morphology operation step have a significant effect on image analysis results, and several (8) settings lead to a high (> 80%) extent of matching and low (< 10%) cumulative error.

The minimum area threshold in the particle selection step defines the smallest particle that would be further processed, i.e. an object will not be considered as a particle if its pixel area is less than the threshold. With a minimum area threshold value of 200 pixels, objects whose projected area in the image is less than 361μm^2 will be ignored. We studied the effect of several values of the minimum area threshold from 100 to 800 pixels, and the corresponding IA results varied from cumulative error of 22.7% to 31.9%, and extent of matching varied from 56.0% to 65.3%.

The effect of image enhancement was also studied. It was found that without the contrast-limited adaptive histogram equalization, the cumulative error and extent of

matching varied from 8.0% to 19.3% and 45.9% to 88.6%, respectively. With the adaptive histogram equalization, the cumulative error ranged from 8.0% to 26.1% and the extent of matching from 62.2% to 94.3%. It was noted that while in some cases, adaptive histogram equalization improves the results, in others it degrades performance with no discernible pattern.

Overall, every IA parameter studied was found to affect the image analysis results, and therefore a careful consideration is warranted. By comparing the complete set of results, we concluded that the parameters shown in Table 6.3 are the best suited for the MSG seeded Crystallization experiments.

Table 6.3: Optimal IA Parameters for PVM Images from MSG Crystallization

	IA Step	**Parameters**	**Parameter Value**
1	Image Selection	Intensity Range	120
		Lowest Pixel Threshold	200
2	Image Enhancement	With/Without the Contrast-Limited Adaptive Histogram Equalization	With
3	Canny Edge Detection	Low Threshold	0.1
		High Threshold	0.2
		Sigma	2
4	Morphology Operation	Structuring Element for Morphological Closing, Se1	Diamond 5
		Structuring Element for Morphological Opening, Se2	Square 5
5	Particle Selection	Area Threshold	200

With these settings, the IA methodology automatically identifies 105,118 particles from the 29,898 PVM images in Experiment X with high quality – at most 8.0% cumulative error, and up to 94.3% extent of matching, with a δ of 0.7. Even at a strict $\delta = 0.1$, the extent of matching is 67% and the cumulative error is as low as 4.1%. The effect at intermediate values of δ is shown in Fig. 6.2 (a) and (b) where the smooth variation testifies to the validity of the metrics.

Fig. 6.3 shows the hourly values of the extent of matching and the cumulative error as crystallization proceeds. As can be seen there, the extent of matching and cumulative error vary only within short ranges as crystallization proceeds although the quality of PVM images varies significantly due to the presence of more particles in the later stages (see Fig. 4.11 (a) and Fig. 4.12). This shows the image analysis parameters are adequately robust (vis a vis the human eye based segmentation) to the solid concentration.

Finally, these image analysis parameters selected using Template 1 were also validated using the independently developed Template 2. As shown in Fig. 6.2(b), the cumulative error is also consistently low (4.2% to 6.7%). The much lower extent of matching (22% to 30%) is due to the much larger (13x) number of particles in this template compared to Template 1. From these studies, it is clear, that with the selected parameters, accurate, consistent, and robust particle size estimation can be obtained automatically by the IA methodology. These studies also demonstrate that the IA procedure with optimal parameters obtained by training with big well-shaped particles (Template 1) can provide good results when applied to more challenging situations (e.g. Template 2). Next, we use these settings for monitoring crystal

growth during several crystallization runs.

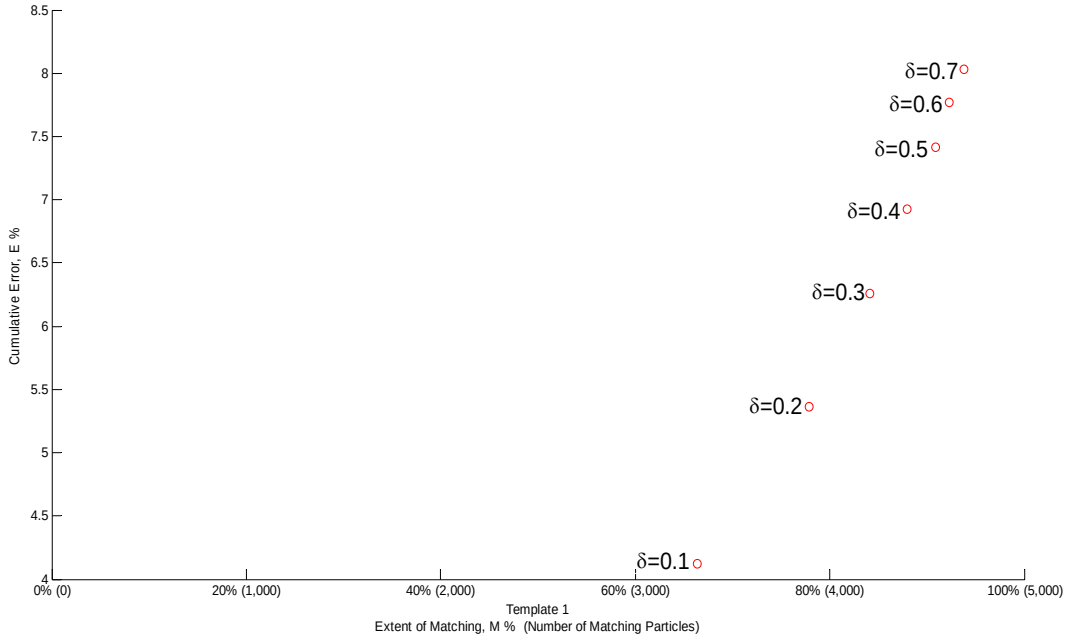

(a)

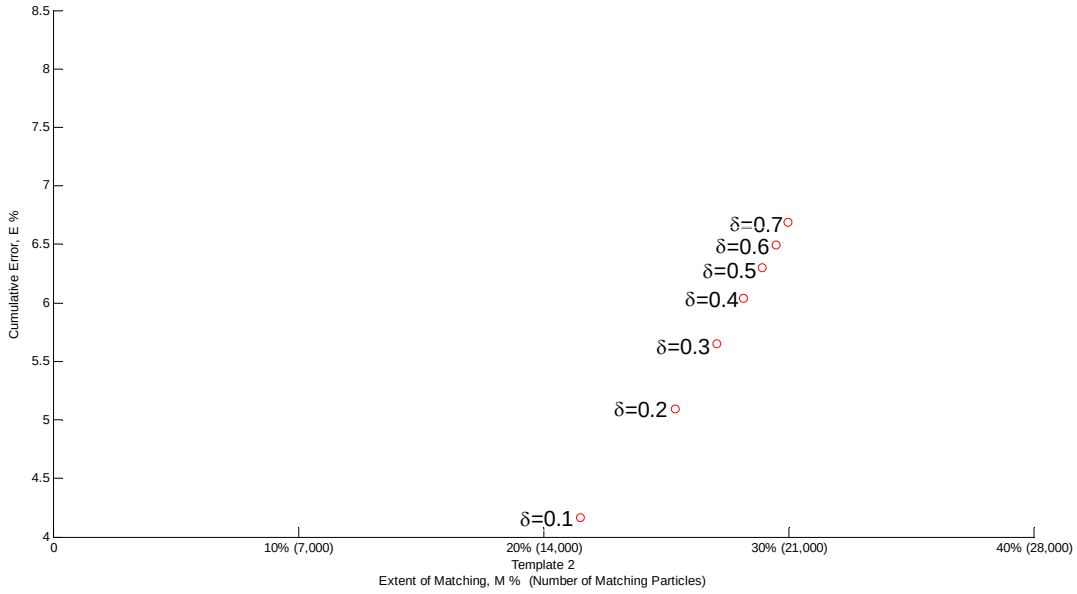

(b)

Figure 6.2. Quality of image analysis results
as measured by (a) Template 1 and (b) Template 2.

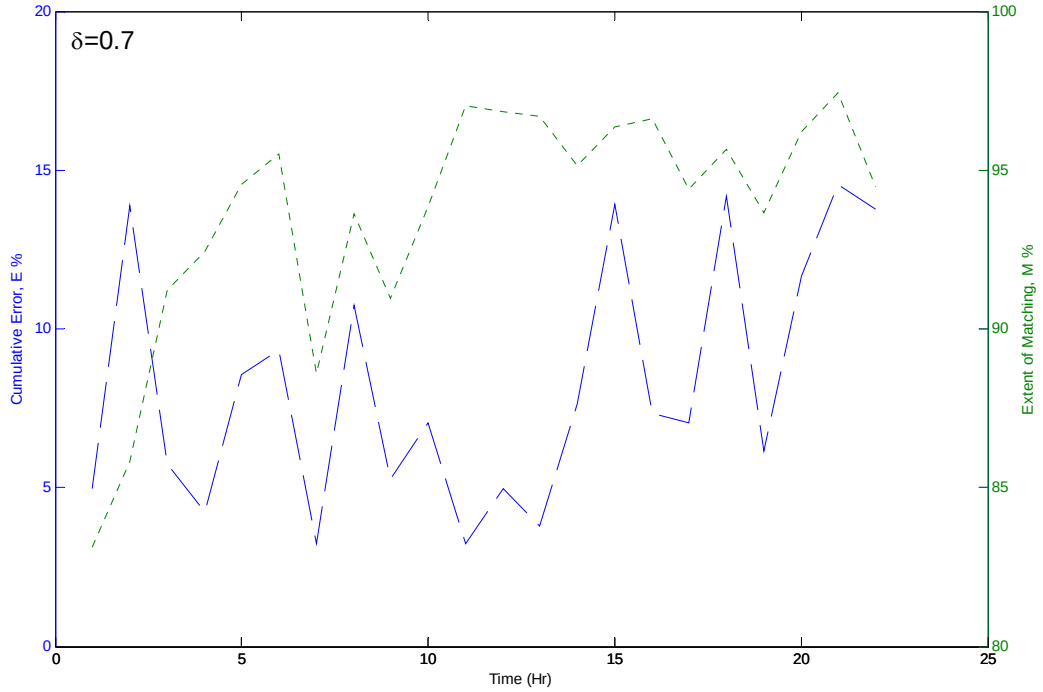

Figure 6.3. Time evolution of extent of matching and cumulative error during experiment X.

6.2 IA-Based Real-Time Monitoring of Particle Growth in Seeded MSG Crystallization

With the optimal setting of parameters obtained in Section 6.1, we apply IA for real-time monitoring of particle growth in seeded MSG crystallization processes. According to the experiments described in Section 4.2.2.2 and Table 4.2, we studied the growth of MSG crystals by examining the particle size distribution at various times during the crystallization. The size (length) distribution was derived for each hour by statistically combining the particle size information from the images captured during that hour. These give hourly snapshots of the process evolution. Fig. 6.4 shows the evolution of the median particle size during Experiment X as obtained

from the IA methodology. In order to validate these, we also extracted (in a similar fashion) the size from the particles segmented by operator 2 from the same images. The median size from the IA methodology was found to be highly consistent with that obtained from Template 2. Both results clearly indicate that MSG crystals are growing in length throughout the course of the experiment.

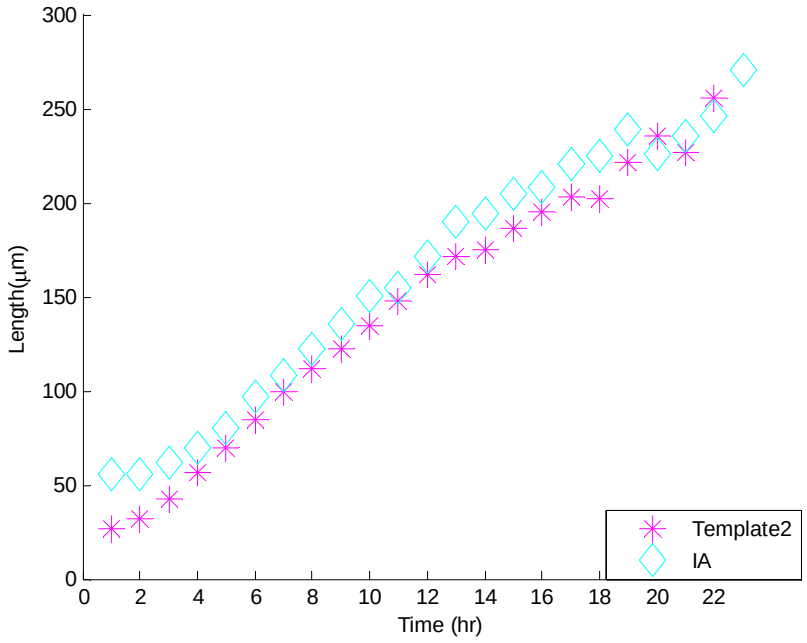

Figure 6.4. Median particle size during experiment X estimated from image analysis and manual segmentation

The estimated particle size distribution at every hour obtained from IA methodology is shown in Fig. 6.5 and provides further insights into the crystallization kinetics. The particle width was also measured from these images (not shown here) and found to not vary significantly during the course of the experiment indicating that the kinetics of the two faces of the crystal are in fact significantly different.

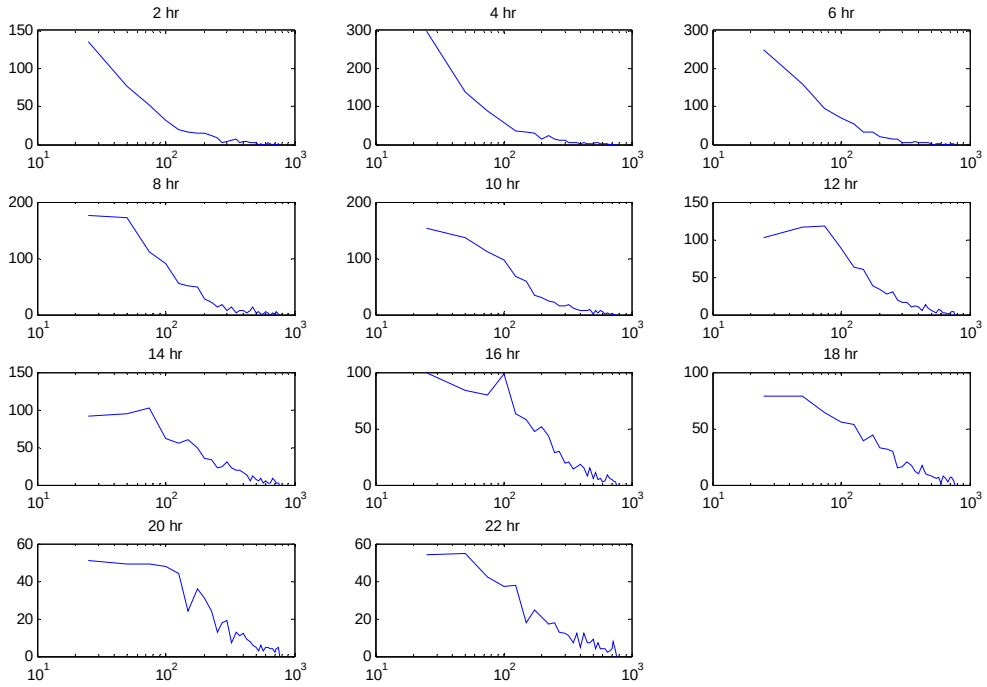

Figure 6.5. Bi-hourly particle size distribution during Experiment X.
In each subplot, x-axis represents particle size in μm, and y-axis represents the count number.

Images from the four other experimental runs, Experiments A, B, C and D as described in Section 4.2.2.2 and Table 4.2, were also similarly analyzed. In the interest of space, only a summary is presented here. Fig. 6.6 shows the evolution of the median particle size for each experiment. Particle growth is clearly evident in all the experiments. However, there are some variations in the growth rate – the median particle size during Experiment A is different from that in Experiment B in the first 50 hours, but overlaps for the next 50 hours. Experiment C and D are consistent with each other for the entire duration. Several possible reasons, as discussed earlier, may contribute to these variations. Overall, similar growth rates are observed in all the runs.

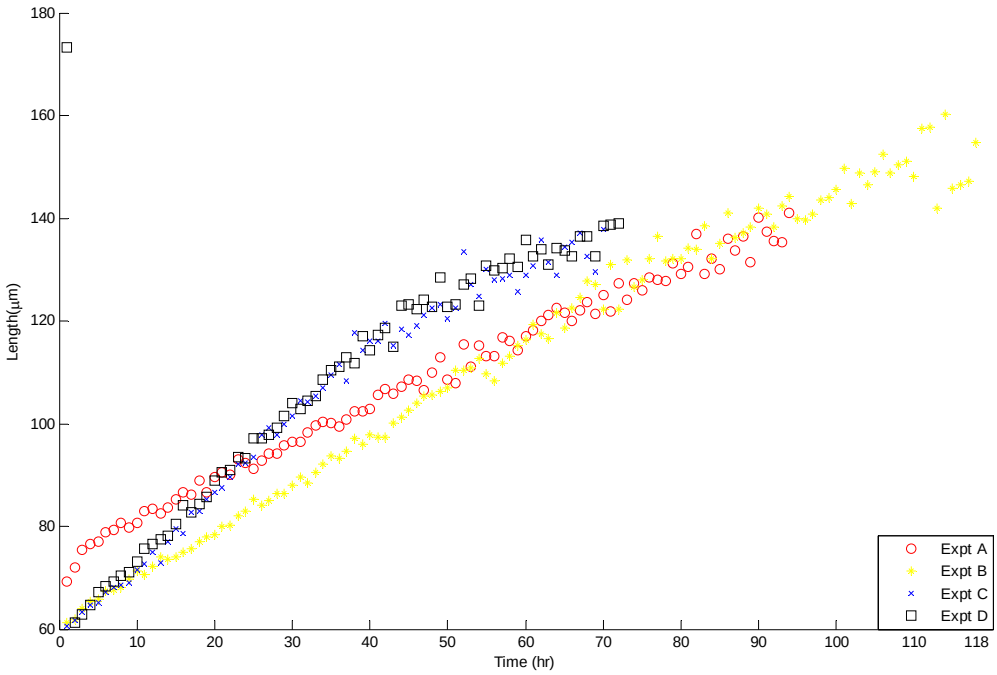

Figure 6.6. Growth of particles during four MSG crystallization experiments.

6.3 Conclusion

The results show that although all image analysis parameters have some effect, the four structuring elements in morphology operation step have the most significant effect. These determine the shape information of the objects (particles) to be extracted from the image. This reveals that for segmenting needle-shaped MSG particles, the diamond and square are the most suited structuring elements. Further study is required to establish the generality of this conclusion to other systems.

This work has also demonstrated that when tuned suitably, automated image analysis can estimate particle sizes with high accuracy (about 4-8% error) relative to that seen by the human eye. Image analysis using the PVM system is therefore a reasonably accurate approach to track particle growth. At the initial stage of

working with a new system, we need to manually segment particles from one experimental run and establish an optimal set of parameters for PVM based image processing by using systematic perturbation to the IA parameters based on the theory of design of experiments. In production plants where a large number of similar crystallization runs would be carried out, despite the high one-time cost of manual segmentation, the large benefits incurred from a certifiably accurate particle-size distribution available in real-time would make the proposed scheme attractive. Furthermore studies are required to formulate a systemic procedure for IA parameter optimization that would reduce the parameter optimization effort so as to make it workable with as little human effort as is possible.

Chapter 7. Optimization of Image Processing Parameters

7.1 Introduction

Common image processing algorithms usually involve a number of parameters in each step. Examples include the parameters in an image filter, the threshold values in edge detection, and the options of shape and size for structuring elements in morphology operations. The setting for each of these parameters may have a significant effect on the final image processing result. Manual tuning is commonly applied to select optimal image processing parameters, but such an approach may be time consuming and challenging when the image set is large, quality of images varies and the image processing parameters may be sensitively related to each other. Manual tuning of image processing parameters is especially difficult for industrial processes where the quality of the images varies as the process evolves. For example, in batch crystallization operations that are conducted in chemical or pharmaceutical industries, the process images are acquired at a speed of up to 10 images per second and each batch can last for a few days or weeks. It is usual to analyze tens of thousands of images in real-time to characterize particle size distribution and shape information for certain process period. In each batch, as

crystals form and grow, the image quality changes from images with clear background to images with a lot of overlapping particles. Even for the same crystallization process, the image quality changes from batch to batch owing to the complexity of the process. It is hard to manually tune the image processing parameters and find an optimal set of values for parameters that are not only suitable for images of the entire duration of a particular batch but also suitable for images obtained from different batches. The problem of manually tuning image processing parameters can be more complicated if the involved parameters are highly interacting with each other. The manual tuning approach is usually done in "one parameter at a time" manner and this will very likely reach a sub-optimal solution. Hence, it is necessary to develop a systematic and automatic methodology to optimize a set of image processing parameters for a large set of process images.

There are several ways to solve the problem of optimizing image processing parameters. In model-based optimization approaches, one constructs models between image processing parameters (input factors) and performance metrics (output responses), so the optimal parameters are obtained by solving the models. In the direct search approach, optimal image processing parameters are determined in a model-free manner by searching the parameter space using heuristics. Note that in this chapter, the words "parameter" and "factor" will be used interchangeably.

Model-based optimization approaches require building reliable and robust mathematical models to accurately predict the optimal parameters. To generate enough information to construct models, Design of Experiments (DOE) is

commonly applied. DOE is a well-structured, generic and organized methodology. It designs a set of experiments by systematically varying the input factors. The designed experiments cover the permissible factor space efficiently with only a few experimental runs and provide significant information about the system being studied. The results obtained from designed experiments can be used to fit a model that will quantify the effects of each input factor on the output responses, as well as determine the interaction between factors and identify the most influential factors. Such analysis can help in conducting further experiments or in arriving at the optimal values for the input factors. As long as the input and output factors are identified and the variation ranges of each input parameter are known, this approach can be applied to any system that exhibits smooth behavior. Model-based optimization approaches with DOE has been applied to improve product quality in large-scale manufacturing lines, to find optimal reaction conditions in experimental R&D systems (Verran et al., 2008; Yamashita et al., 2010), as well as to solve difficult production problems (Kenny, 1997). As DOE extracts process knowledge by conducting only a few systematically designed experiments, it is time- and cost-effective. Furthermore, since the designed DOE experiments cover the whole permissible factor space, the predicted optimal parameters could be globally optimum and not destined to be a local one (Lucas et al., 2006; Matsopoulos et al., 1999).

Optimization, in conjunction with DOE, has been applied for image processing with a view to improve image quality (Taner & Sezen, 2007; Trivedi & Kurz, 1992), optimize input parameters for various image processing algorithms (Chen & Wu, 2004; Wu et al., 2005; Lucas et al., 2006), as well as detect nucleation in

crystallization by histogram matching (Simon et al., 2010b) . These studies show that optimization with DOE is a powerful statistical technique to evaluate the effect of parameters so that they can be tuned to get best outcomes from image processing algorithms. Although research articles have begun to address problems where processing of large number of images is needed, the quality of the images in these studies is found to have low variability. As stated, in certain chemical and pharmaceutical batch processes, image quality varies significantly from batch to batch. Even in the same batch, image quality varies with time. There is a relative lack of literature on optimizing image processing parameters for such large sets of process images which are of varying quality. There are also fewer studies showing the validation of the obtained optimal parameters on other batches of images acquired from the same process. In this chapter, we investigate these problems and the results demonstrate that optimization of image processing parameters using DOE concepts can successfully locate good parameter values using only few *in silico* experiments.

As an alternative to the model-based DOE approach, direct search for the optimal values of image processing parameters in the parameter space can also be attempted. In this case, there is no explicit mathematical model to relate input factors with the system response. Direct search methods, such as sequential simplex search (SSO), are typically applied to solve optimization problems in a ‘model-free” manner. Simplex method requires only function evaluations and the optima is reached by adjusting input factors according to a pre-set algorithm. Simplex progresses according to empirical experimental response without the complexity of mathematical modeling and can be regarded as an automatic optimization method.

Simplex search method is simple but powerful. It has been widely applied to image processing-related areas. It has been used to register various kinds of medical images (Matsopoulos et al., 1999; Xia et al., 2008), to calibrate or correlate stereo vision systems (Yocky & Jakowatz, 2007; Chesi, 2009), to design filters for image processing (Dellamonica et al., 2007), and also to optimize parameters for certain image processing algorithms (Kamoun et al., 2009; Welch et al., 2003). These studies show that simplex is an efficient, robust solution for a wide range of image-related optimization problems. Simplex requires only limited experimental runs in the initial design and is capable of optimizing several parameters simultaneously. Despite these benefits and applications, there are no studies on using simplex search for optimizing image processing parameters for large sets of process images that are characterized by changing image quality.

In this chapter, we will combine model-based optimization with DOE and direct search optimization to determine optimal values of image processing parameters. The obtained optimal parameters will be validated with a fresh batch of process images. This chapter adopts Uniform Design (UD) (Liang et al., 2001) as the specific DOE algorithm and SSO (Walters et al., 1999) as the specific direct search method.

The rest of this chapter is organized as follows. In Section 7.2, we will summarize the optimization procedure with model-based UD approach followed by a description of optimization with the simplex search approach. In section 7.3, the two optimization approaches are combined to locate optimal sets of IA parameters for

large sets of process images, which are obtained from batches of MSG crystallization process. Conclusions will be provided in Section 7.4.

7.2 Methods for Parameters Optimization

Model-based optimization with DOE is a common solution to parameter or factor optimization problems. The major DOE methods include factorial design, fractional factorial design, orthogonal design, D-optimal design, uniform design, etc. Usually, these methods will pre-define input parameters into different levels and suggest certain runs of experiments according to the chosen experimental design plan (e.g. 2k or 2k-f). By analyzing the results of designed experiments, the model-based optimization methods will correlate the relationship between input parameters and output responses in the form of mathematical equations which subsequently predict the optimal values of parameters. To build a reliable and robust model with the minimum number of experimental runs, the designed experiments should be well-structured and efficiently map the whole experimental domain. UD is such a DOE method and its major advantage over other similar experimental designs is its capability of designing high representative experiments in the studied experimental domain [27]. UD is cost-efficient, robust and flexible.

As for the direct search optimization approach, the variable-size SSO algorithm is selected to optimize the parameters of the image processing algorithm. SSO approach is easy to understand and is very efficient for practical applications. SSO directly searches for the optimal parameters step by step in the multidimensional parameter space. There is no need for a mathematical model to relate input factors

and output responses; instead the SSO adjusts the input factors and optimizes them based on the systems' response. For a process with n input factors, SSO will initially design n+1 runs of experiments. Using these experimental results, SSO will search for a new set of parameter values that can generate a better output response. This search procedure will be repeated until an ideal set of parameter values (optimal parameters) is obtained. Normally, SSO will converge to a small region in the parameter space and the values from this region are considered as optimal parameter values. To fully understand the relationship between input parameters and output response in this optimum region, researchers may prefer to build a mathematical model in this region and estimate the optimal parameters. However this modeling step is not necessary; normally any set of parameters in the region to which the SSO converges is good enough. The efficiency and accuracy of SSO often depends on the starting simplex that is constructed.

The detailed procedure of optimization with UD and SSO are explained below.

7.2.1 Model-Based Optimization with Uniform Design

As shown in Fig. 7.1, the optimization with DOE includes three parts: (i) the DOE part that designs certain runs of experiments to get informative data from the system; (ii) the modeling part that will construct system models with the data and relate the input factors with system responses; and (iii) the prediction part that will determine the optimal input parameters using the model. Predicted optimal values of parameters are usually verified by conducting a confirmatory experiment.

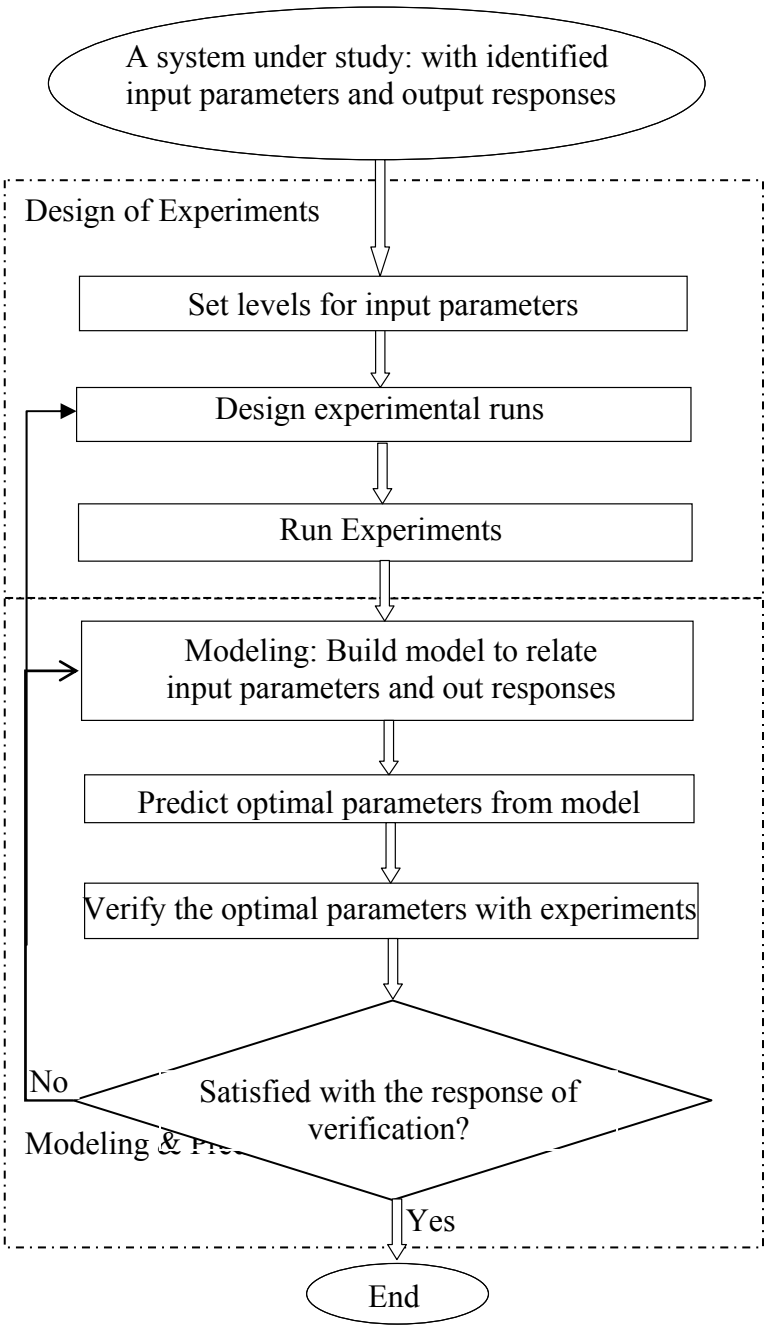

Figure 7.1. Procedure of optimization with design of experiments.

UD is employed here as the DOE method. The first step with UD is setting the number of levels for each input factor. The levels, which are the different values of a factor, should be within the experimental domain. The gap between two successive levels of a factor should be relatively large so as to overcome the effects of random

error.

The next UD steps are to design the experimental runs and conduct the designed experiments on the system of interest. As the purpose of UD is to understand the system behavior using least number of experiments, the designed experiments must be most representative, uniformly spread over the whole space of experimental factors and contain the most information between input factors and output response. As stated in Liang et al., (2001), there are several algorithms to fulfill this task. Instead of using computationally intensive methods to compute the UD, there are well-designed UD tables that in the literature (Liang et al., 2001; Website, 2004). These UD tables are carefully designed according to different number of parameters and different levels of each parameter. One can directly apply these UD tables to design experiments and execute them on the physical system.

The next step is to analyze the experimental results and construct mathematical models which quantitatively represent the relationship between input factors and output responses. Different modeling paradigms are possible. Here, as not much a prior knowledge exists about the model structure, we use a genetic programming (GP) tool described by Rao et al. (2009) to automatically assemble an appropriate mathematical model.

The last step in this model-based optimization method is to predict an optimal set of input parameter values from the constructed models and verify it by conducting an experiment with those predicted values. If the experimental result is consistent with model prediction, one may conclude the procedure and declare that the optimal

values of parameters have been obtained. Else, the additional "experimental result" is added to the data set and another model is constructed to determine the optimal parameters. If the predicted optima could not be validated even after a few iterations, one may consider performing another round of experiments.

7.2.2 Variable-Size Sequential Simplex Optimization

SSO is a step by step procedure to search for the optimal values in the parameter space. For a system with n input factors, [x_1, x_2, …, x_n], and 1 output response, y, the SSO iteration procedure is shown in Fig. 7.2 and described below:

Step 1: Here, the starting vertices of SSO are designed. There are many ways to design the initial n+1 vertices for an n-parameter optimization problem. According to Kamoun et al. (2009), a typical initial design representing n+1vertices in n-dimensional simplex is listed in Table 7.1. There is one row for each of the n+1 vertices, one column for each of the n parameters. Assume the initial guess for each parameter is X_i, that is [X_1, X_2, X_3, …, X_n] for the n parameters respectively. Define the step size S_i for each parameter, that is [S_1, S_2, S_3, …, S_n] respectively. In Table 7.1, the symbol $v_{i,j}$ represents the value of i^{th} parameter in j^{th} vertex, $v_{i,j}$ is calculated with the equations given below.

$$\begin{cases} v_{i,j} = \dfrac{-1}{\sqrt{2i(i+1)}} \cdot S_i + X_i & if \quad i > j \\ v_{i,j} = \dfrac{i}{\sqrt{2i(i+1)}} \cdot S_i + X_i & if \quad i = j \\ v_{i,j} = X_i & if \quad i < j \end{cases} \tag{7.1}$$

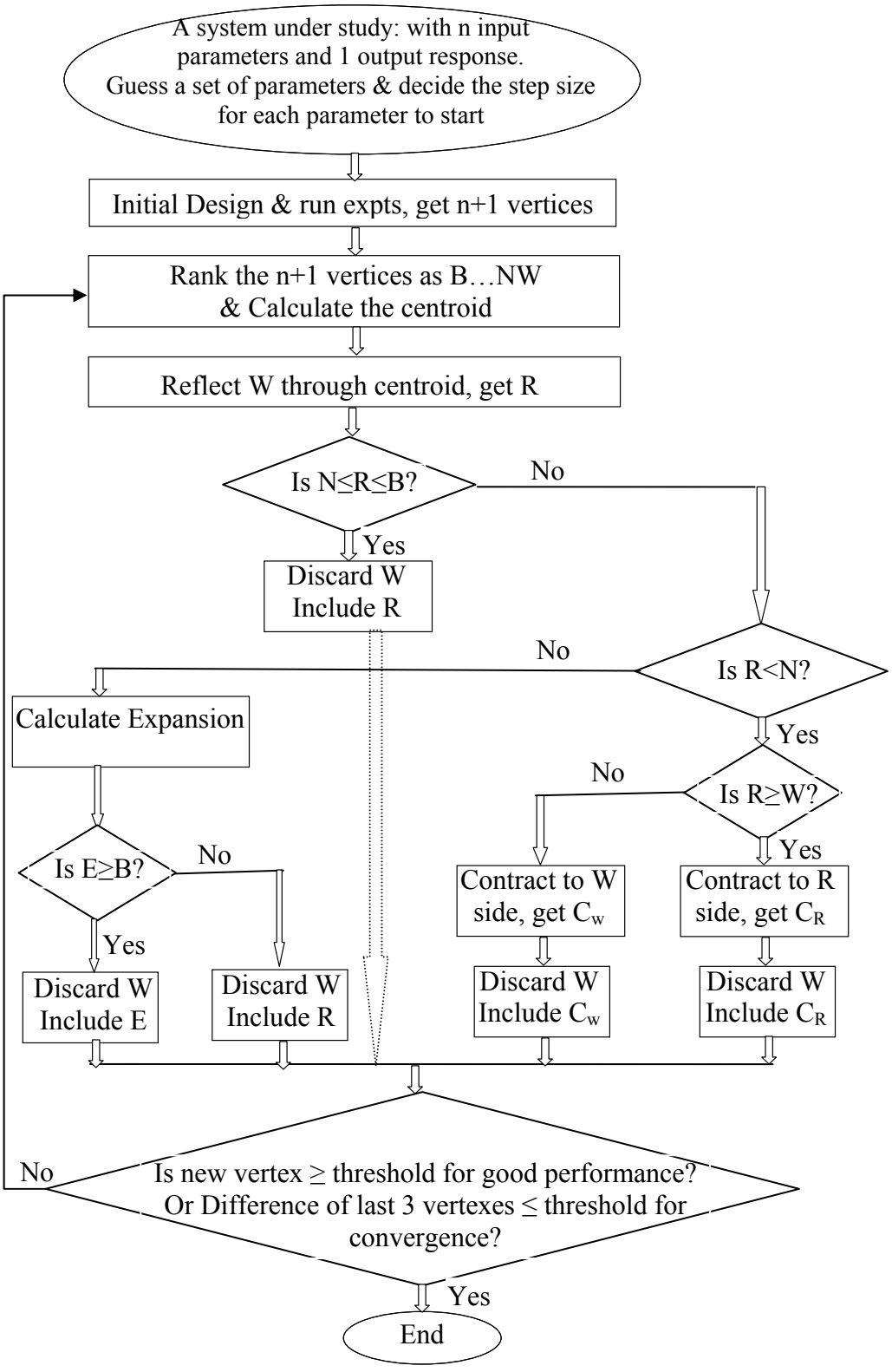

Figure 7.2. Procedure of variable-size sequential simplex optimization.

Table 7.1: Typical Initial Design of Simplex

Vertex	Parameters				
	x_1	x_2	x_3	…	x_n
0	$v_{1,0}$	$v_{2,0}$	$v_{3,0}$	.	$v_{n,0}$
1	$v_{1,1}$	$v_{2,1}$	$v_{3,1}$	.	$v_{n,1}$
2	$v_{1,2}$	$v_{2,2}$	$v_{3,2}$	.	$v_{n,2}$
3	$v_{1,3}$	$v_{2,3}$	$v_{3,3}$	.	$v_{n,3}$
…	.	.	.	.	.
n	$v_{1,n}$	$v_{2,n}$	$v_{3,n}$	.	$v_{n,n}$

Step 2: In this step, one calculates the reflection vertex of the vertex with worst response. From the designed n+1 vertices, the vertex giving the best response is named as B; the vertex giving the worst response is named as W and the i^{th} parameter in the W vertex is defined as W_i; the vertex giving the next-to-the-worst response is named as N. Simplex assumes the optimal parameters should exist at the opposite direction of the worst vertex, so it reflects W through the centroid of the remaining n vertices (except the worst vertex of the n+1 vertices) with an identical distance. The centroid point of the i^{th} parameter is defined as P_i, which is calculated as:

$$P_i = \frac{\sum_{j=1}^{n} v_{i,j}}{n} \tag{7.2}$$

where, j=1 to n, includes all the vertices except the W vertex. The reflected coordinate R_i for the i^{th} parameter is calculated as below:

$$R_i = P_i + (P_i - W_i) \tag{7.3}$$

Step 3: Here, we evaluate the reflection point according to the following criteria:

A) If N ≤ R ≤ B, it implies that the reflected vertex is not better than B and not worse than N. We have no clue whether R is in the right direction. In this case, SSO will discard W and include R to form a new set of n+1 vertices.

B) If R > B, it implies that R is in the same direction as the optimal point. We would like to go further in this direction and evaluate the response. The expansion vertex is named as E and the coordinate of i^{th} parameter in E is defined as E_i and calculated as

$$E_i = P_i + 2(P_i - W_i) = R_i + (P_i - W_i) \tag{7.4}$$

a) If E ≥ B, we have a successful expansion. In this case, SSO will discard W and include E to form a new set of n+1 vertices.

b) If E < B, the expansion is not successful. In this case, SSO will discard W and include R to form a new set of n+1 vertices.

C) If R < N, it implies that the reflected vertex is worse than the next-to-the-worst vertex indicating that R is not in the correct direction to reach the optimal value. So we would like to contract this large movement to a small one and gradually search for a better point in this direction. The contraction could be either at the R side or at the W side.

a) If R ≥ W, it implies that the reflected point is not worse than the worst point and the contraction should be at the R side. In this case, SSO will

discard W and include the contraction vertex C_R to form a new set of n+1 vertices. The coordinate of the i^{th} parameter in contraction point C_R is defined as:

$$C_{R_i} = P_i + (P_i - W_i)/2. \quad (7.5)$$

b) If R < W, it is clear that the reflected point is worse than the worst point and the contraction should be at the W side. In this case, SSO will discard W and include the contraction vertex C_w to form a new set of n+1 vertices. The coordinate of the i^{th} parameter in C_w is defined as

$$C_{w_i} = P_i - (P_i - W_i)/2. \quad (7.6)$$

Step 4: With the newly formed n+1 vertices, steps 2 and 3 are iterated until either an optimal point is reached or the responses of the n+1 vertices converge to a small region without further improvement of the performance.

7.2.3 Integration of Two Optimization Approaches

It is obvious that each optimization approach has its own advantages and shortcomings: Model-based optimization with UD could cover the whole parameter space in initial design, while it requires more effort for modeling and prediction. Direct search optimization with SSO does not involve such mathematical modeling and verification, but it possibly searches for local optima only.

In this chapter, we propose to integrate the two optimization approaches: 1) The mathematical models built from UD will be solved by SSO approach; 2) SSO adopts

multiple initial guesses from UD. This integration will save the effort to solve complex UD models, as well as enable SSO to have a better chance of locating the global optima.

Next, either the two optimization approaches or the integrated version will be applied to our previously developed multi-step IA algorithm (Zhou et al., 2009).

7.3 Optimization of IA Parameters

Chapter 3 developed an IA algorithm to estimate particle size in real-time by on-line analysis of PVM images that are acquired from crystallization processes. As shown in Fig. 3.8, the developed IA methodology involves six key sequential steps to identify particles from PVM images and estimate the corresponding particle size. Each IA step involves certain parameters - the study (Chapter 6) shows that the setting of the parameters can dramatically affect IA performance. With correct settings of these parameters, IA can be successfully applied to the images acquired from large scale seeded MSG crystallization and it leads to good tracking of the evolving particle size.

Previous studies (Chapter 6) manually tuned the 10 IA parameters and concluded that only 7 parameters coming from Canny edge detection and morphology operation steps significantly affect IA performance. The seven factors are: Canny-T1, Canny-T2, Canny-Sigma, SE1-Shape, SE1-Size, SE2-Shape and SE2-Size. The details of these parameters are listed in Table 6.1. In this chapter, with the same set of images, instead of manual search, we will automatically

optimize these 7 IA parameters using the two methods discussed in Section 7.2.

7.3.1 Optimization with Uniform Design Method: Model Solving by Simplex

The IA parameter optimization problem can be cast as a 7 factors 6 levels UD problem. As listed in Table 7.2, the 7 parameters are denoted as input factors u1 to u7 and each parameter is assigned to 6 levels according to its range. It should be noted that u4 and u6 only have 4 values (corresponding to the four shapes considered as defined in Table 2) instead of 6 values. Thus, levels 5 and 6 in u4 and u6 are considered as infeasible experiments and omitted from consideration. E (y_1) and M_A (y_2) are the two output responses of this optimization problem. At least nine UD based experimental plans are available for this 7 factors 6 levels problem. A close examination of these plans confirmed that some of the experimental runs suggested in these plans are not feasible due to the constraint conditions given in Table 6.1.

After eliminating such unfeasible experimental runs, a total of 105 feasible experiments are identified. The parameters and corresponding results of the finalized 105 runs of experiments are depicted in Fig. 7.3.

About half of the experimental runs (56 runs) are randomly selected to build mathematical models that relate 7 input parameters with 2 output responses. The models, as listed below, are built with the software GeMS-Genetic Modeling System described in Rao et al. (2009).

$$y_1 = \frac{-0.1433u_7 + 0.1141u_5}{u_2} - 0.4740u_7 + u_6 + 2.231u_7 + \frac{2.231u_6}{u_3}\left(\frac{1}{u_2} - 1\right) - 2.231$$
$$y_2 = -\frac{53.46}{u_5} - 2.009u_7 - \frac{2.197}{u_2} - \frac{0.1564u_5}{u_2} + u_3 + 43.86 + 81.42(1 - u_2) \quad (7.7)$$

The RMSE for y_1 and y_2 are 10.32 and 10.84 respectively. These models are verified with the remaining 49 experimental runs, as shown in Fig. 7.4. For the validation set, the RMSE for the two models are 10.75 and 14.15 respectively. It is evident that the built models are reasonable.

Table 7.2: 7 Factors 6 Levels Uniform Design of IA Parameters

	Levels	1	2	3	4	5	6
Canny Edge Detection	Low Threshold: Canny-T1 (u1)	0.00	0.05	0.1	0.15	0.2	0.25
	High Threshold: Canny-T2 (u2)	0.05	0.15	0.25	0.35	0.45	0.55
	Sigma: Canny-Sigma (u3)	1	1.5	2	2.5	3	3.5
Morphology Operation	Close Shape: SE1-Shape (u4)	1	2	3	4	NA	NA
	Close Size: SE1-Size (u5)	0	5	10	15	20	25
	Open Shape: SE2-Shape (u6)	1	2	3	4	NA	NA
	Open Size: SE2-Size (u7)	0	5	10	15	20	25

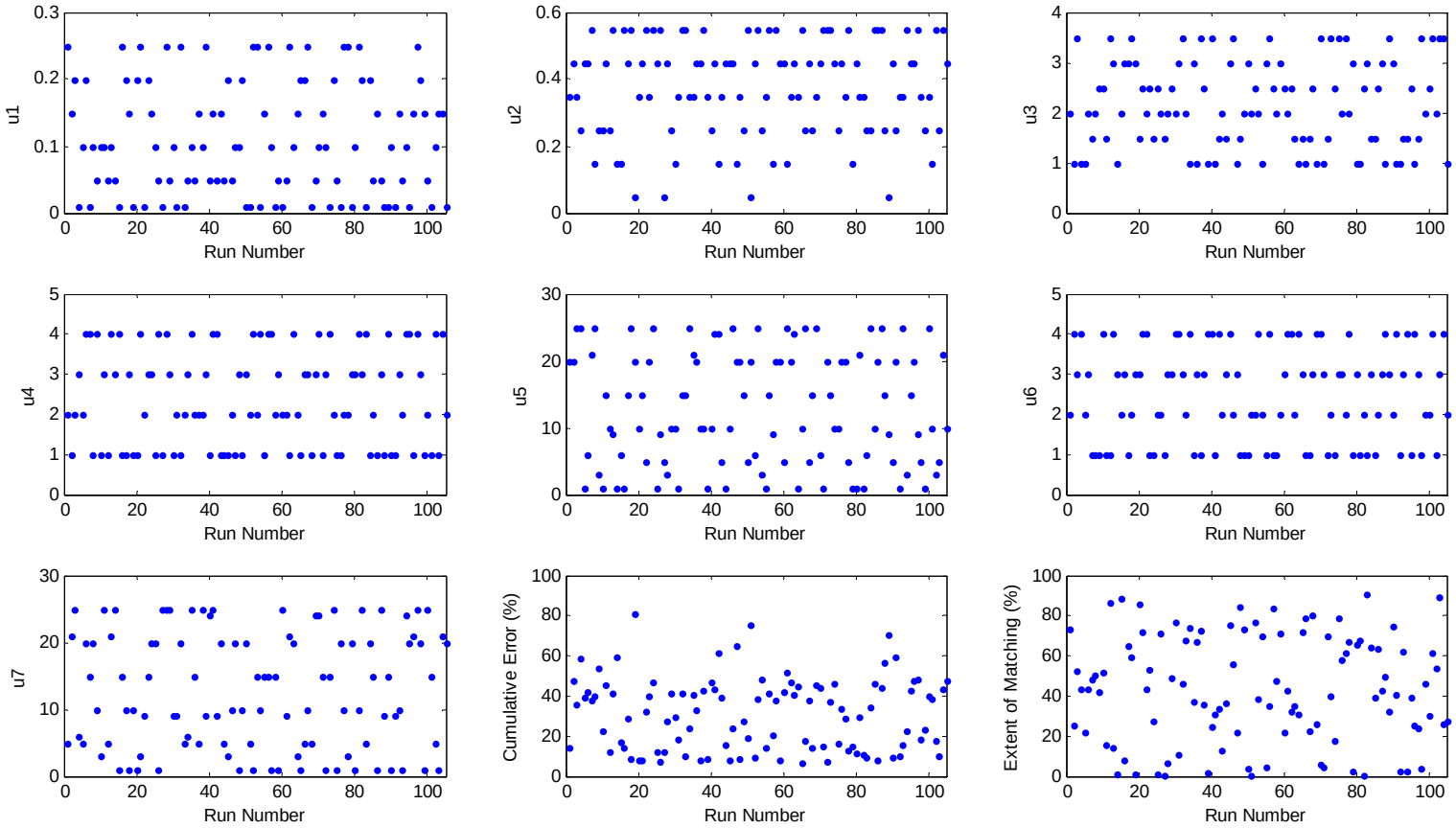

Figure 7.3. Parameters and responses of 105 experimental runs of UD.

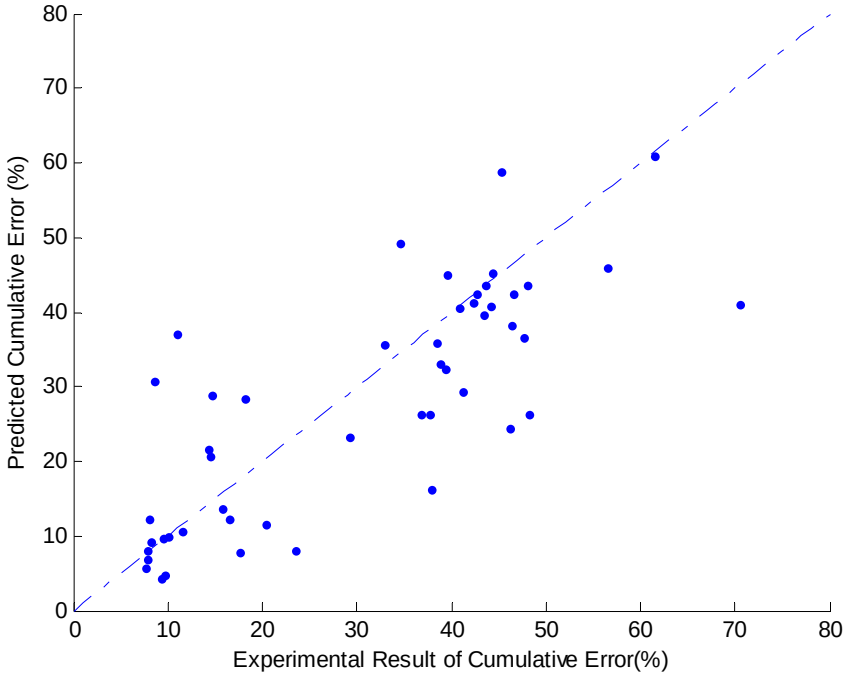

(a)

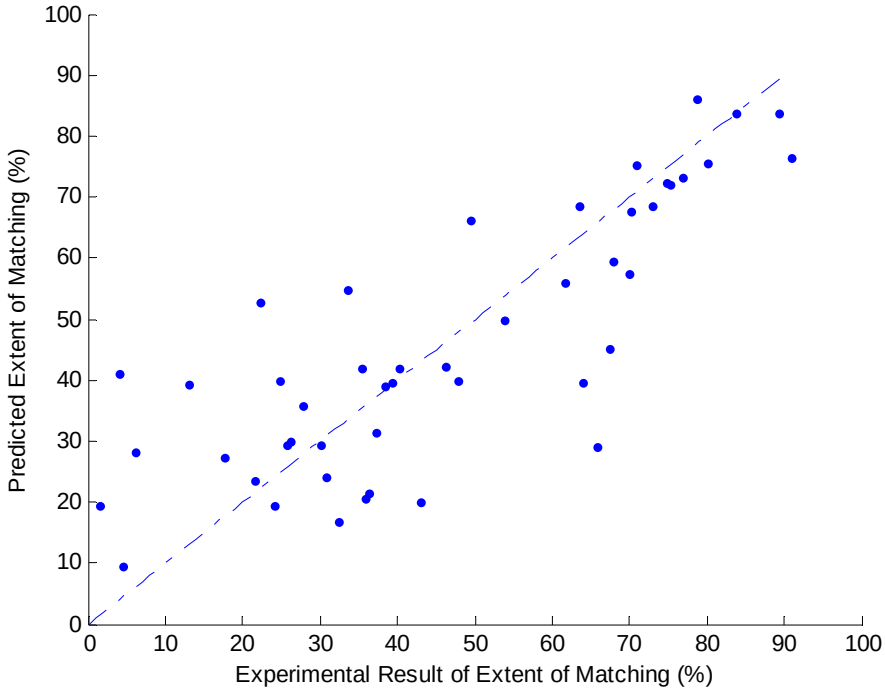

(b)

Figure 7.4. Comparison of model prediction and experimental validation (a) cumulative error (b) extent of matching.

The next step is to predict the optimal parameters from the built models. Both exhaustive search method and simplex optimization method may be employed for this purpose. Using an exhaustive search, that is, search of the whole parameter space with step size of [0.01, 0.1, 1, 1, 1] for [u_2, u_3, u_5, u_6, u_7] respectively, ten sets of parameters that are likely to result in $y_1 < 5\%$ and $y_2 > 85\%$ are identified and listed in Table 7.3. It is noticed that the 10 parameter sets are quite similar with differences only in u_2 and u_5. When these sets of parameters are verified, the results show that all of these 10 sets of parameters can give better output response for y_1 while worse output for y_2 than what the models predict, with the best result of 8.55% and 91.73% for E and M_A respectively.

Depending on the step size of each parameter, the exhaustive search to locate best parameter values can be quite time consuming, especially with more parameters and a broader parameter search. Simplex optimization can also be utilized to locate optimal parameter values from the model. Since simplex can optimize only one objective, the two measures of E and M_A are combined into one by defining $ER = M_A / E$. ER will be maximized by using the simplex algorithm as described in Section 7.2.2. The optimal parameter sets obtained are shown in Table 7.3, with the best result of 7.23% and 90.40% for E and M_A respectively. These parameters result in better experimental responses than that predicted by the model. Table 7.3 summarizes the results from the exhaustive search and simplex search.

Table 7.3 Validation of Predicted Optimal Parameters for Uniform Design

	u1	u2	u3	u4	u5	u6	u7	Predicted		Experimental		
								y1 (%)	y2 (%)	y1 (%)	y2 (%)	ER
Exhaustive Search	0.13	0.24	3.20	2	6	1	1	4.99	85.03	8.55	91.73	10.73
	0.13	0.24	3.30	2	6	1	1	4.92	85.13	8.84	91.49	10.35
	0.13	0.24	3.40	2	6	1	1	4.86	85.23	8.70	91.10	10.47
	0.13	0.24	3.50	2	6	1	1	4.80	85.33	9.13	90.84	9.95
	0.13	0.25	3.50	2	6	1	1	4.60	85.04	9.09	90.24	9.93
	0.13	0.26	3.30	2	7	1	1	4.97	85.17	8.94	88.51	9.90
	0.13	0.26	3.40	2	7	1	1	4.91	85.27	9.34	88.79	9.51
	0.13	0.26	3.50	2	7	1	1	4.86	85.37	9.47	88.73	9.37
	0.13	0.27	3.50	2	7	1	1	4.68	85.03	9.30	88.37	9.50
	0.13	0.28	3.50	2	8	1	1	4.91	85.04	9.29	87.10	9.38
Simplex Search	0.10	0.20	2.00	1	5	1	1	7.12	83.49	8.25	93.50	11.33
	0.10	0.20	2.00	2	6	1	1	7.69	84.49	9.00	90.58	10.06
	0.16	0.28	2.09	2	8	1	1	5.96	83.52	7.84	89.07	11.36
	0.12	0.28	1.99	1	7	1	1	5.67	82.98	7.75	91.12	11.76
	0.16	0.29	2.07	2	6	1	1	4.97	81.94	7.23	90.40	12.50
	0.14	0.29	2.03	1	5	1	1	4.62	80.60	7.45	91.95	12.34

These results demonstrate that optimization with uniform design is a good method to search for an optimal combination of several IA parameters. This approach initially considers the whole parameter space and its performance depends on building and solving models. Furthermore, both exhaustive search and simplex optimization could be applied to obtain optimal values for the parameters. To obtain more accurate parameters, smaller step size is required for exhaustive search and this means more computing time required. Simplex search greatly improves the efficiency in computing the optimal parameter values. In the next section, we will discuss how to directly find optimal IA parameters without involving any models.

7.3.2 Optimization with Sequential Simplex Optimization

As mentioned in Section 7.2.2, SSO can directly search for an optimal combination of several parameters but it cannot directly deal with multiple objectives. Therefore, maximizing ER (the ratio of M_A to E) is used as the sole objective for SSO. The first step of SSO is related to initial guess and step size of each parameter, it also relates to the constraints and boundary conditions. Each of these can affect SSO performance, as will be demonstrated and discussed later.

7.3.2.1 Initial Guess of Parameters

Simplex optimization is a local optimization methodology and the initial design will affect its convergence rate and precision (Matsopoulos et al., 1999). Only when good prior knowledge of the system is available, the initial guess could be possibly set to the optimal region and the optimal values will be reached within a few iterations. Otherwise, with a poor initial guess, the simplex may restrict the parameters into a bounded poor region and could not break out to search for better parameters. This can be illustrated with the following example. As shown in Row 23 and 24 of Table 7.4, with the IA algorithm studied here, an expert with good knowledge of the system may choose the initial values of the 7 parameters as [0.1, 0.2, 2, 1, 5, 1, 5] and step size for each parameter as [0.05, 0.05, 0.1, 1, 5, 1, 5] respectively. With this initial guess and step size, the 8 runs of initial design, as listed in Table 7.4, will give the best ER response of 7.92 ($E = 11.35\%$ and $M_A = 89.92\%$) and the worst ER response of 3.94 ($E = 20.04\%$ and

$M_A = 78.93\%$). Only after one more simplex step, the ER response is improved to 11.98, with $E = 7.89\%$ and $M_A = 94.61\%$. This result is already better than the published result ($E = 8.03\%$, $M_A = 94.35\%$ and $ER = 11.74$). On the contrary, when the initial guess for parameters is [0.05, 0.5, 0.5, 3, 2, 2, 1] and with the same step size as above, SSO converges to a region with ER about 1.54 after another 26 moves. This shows that initial guess is very important for simplex search.

For a system without any prior knowledge, we suggest to use any experimental run (e.g. a run from uniform design) as initial values. In this paper, the parameters from the first 22 runs of uniform design are used as initial guesses in turn. For each set of these initial guesses, a maximum of 20 SSO iterations will be performed. Table 7.4 lists the results with these different initial guesses. As stated in Section 7.3, each iteration may involve 3 motions of reflection, expansion and contraction, and each motion means a new experimental run. The column titled "Vertex No." in Table 7.4 indicates the number of experiments conducted to reach the optima. It is seen that with different initial guesses, SSO will converge to different regions in the parameter space. Furthermore, all the results with the exception of run number 17, demonstrate that after certain number of iterations, the ER will be better than the best ER from initial design.

The results in Table 7.4 demonstrate that initial guess for parameters will significantly affect the SSO performance. The effect of the step size in SSO is studied next.

Table 7.4: SSO Performance with Different Initial Guess and Step Size (1st set of images)

	No.	Initial Guess							Step Size [0.05, 0.05, 0.1, 1, 5, 1, 5]						Step Size [0.1, 0.1, 0.2, 2, 10, 2, 10]					
		u1	u2	u3	u4	u5	u6	u7	ER from Initial Design		Best ER Obtained from SSO Iteration				ER from Initial Design		Best ER Obtained from SSO Iteration			
									Best	Worst	ER	E	M_A	Vertex No.	Best	Worst	ER	E	M_A	Vertex No.
Initial Guess from Uniform Design	1	0.25	0.35	2	2	20	2	5	6.58	3.27	11.54	7.63	88.07	38	7.97	1.87	12.59	6.45	81.24	39
	2	0.15	0.45	1	1	20	4	20	1.63	0.25	2.25	29.26	65.85	31	1.70	0.17	10.07	7.85	79.13	28
	3	0.05	0.25	2.5	4	3	1	10	2.70	0.39	11.25	8.04	90.42	28	3.49	0.29	12.72	6.86	87.26	35
	4	0.10	0.25	2.5	1	1	4	3	9.84	0.49	12.17	7.47	90.92	15	10.59	0.42	11.66	7.89	91.97	31
	5	0.10	0.45	1.5	3	15	1	25	0.52	0.21	2.37	25.67	60.96	31	0.58	0.13	12.68	7.07	89.66	28
	6	0.05	0.25	3.5	1	10	1	5	8.71	3.46	10.29	8.85	91.06	12	9.56	2.16	10.32	8.47	87.46	39
	7	0.25	0.45	2.5	4	15	4	3	9.77	2.17	12.39	6.60	81.83	31	10.50	1.41	10.61	7.53	79.92	35
	8	0.20	0.35	3.5	2	25	3	25	0.80	0.51	1.48	35.06	51.84	9	1.16	0.51	2.67	26.95	72.07	38
	9	0.01	0.25	1	3	25	4	6	0.81	0.24	4.63	16.61	76.92	30	0.89	0.11	7.19	10.43	74.96	31
	10	0.10	0.45	1	2	1	2	5	3.73	0.48	11.74	7.36	86.36	24	6.63	0.27	11.96	7.64	91.39	33
	11	0.20	0.45	2	4	6	3	20	0.82	0.08	1.52	36.45	55.24	35	0.64	0.10	1.66	34.51	57.38	22
	12	0.01	0.55	1.5	4	21	1	15	1.33	0.86	8.21	8.25	67.78	32	1.55	0.70	9.61	7.84	75.39	37
	13	0.10	0.15	2	1	25	1	20	1.41	1.09	7.54	10.30	77.62	33	1.44	0.81	11.10	7.52	83.46	34
	14	0.10	0.55	3	4	9	4	21	1.18	0.14	2.36	27.15	64.08	35	1.37	0.08	6.81	8.21	55.95	36
	15	0.05	0.15	1	3	1	3	25	0.42	0.01	1.69	37.49	63.37	34	0.41	0.01	1.68	35.79	60.27	34
	16	0.01	0.15	2	4	6	2	1	10.21	2.39	12.37	7.72	95.55	25	10.40	1.58	11.97	8.00	95.75	18
	17	0.25	0.55	3	1	1	3	15	0.46	0.12	0.28	13.38	3.78	9	0.50	0.12	0.35	16.48	5.72	9
	18	0.20	0.45	3	1	15	1	10	2.35	1.58	9.96	7.91	78.79	33	2.87	1.04	10.42	7.58	78.97	33
	19	0.15	0.55	3.5	3	25	2	1	7.08	5.82	7.41	8.27	61.28	40	7.02	3.00	7.68	8.33	64.00	36
	20	0.01	0.05	3	1	20	3	10	0.37	0.00	1.96	34.00	66.75	24	0.82	0.00	5.29	15.38	81.30	21
	21	0.05	0.35	3	3	5	2	20	0.64	0.09	2.40	29.84	71.56	20	0.74	0.03	11.19	7.72	86.32	26
	22	0.01	0.55	2	2	5	4	9	5.03	0.47	10.19	7.02	71.56	33	0.35	6.64	12.50	7.29	91.10	31
Random Guess	23	0.1	0.2	2	1	5	1	5	7.92	3.94	11.98	7.89	94.61	9	11.71	1.72	13.13	7.07	92.80	34
	24	0.05	0.5	0.5	3	2	2	1	1.10	0.31	1.54	46.25	71.32	34	1.25	0.26	1.96	33.54	65.65	25

7.3.2.2 Step Size

To study the effect of step size on SSO performance, each of the 24 initial guesses are assigned with two sets of step size. The first set of step size, s_1 is smaller in magnitude and is taken as [0.05, 0.05, 0.1, 1, 5, 1, 5] for the 7 parameters under study. The second set, s_2 has twice the magnitude of the first set. The details of parameters and the corresponding responses are listed in Table 7.4. If we compare the ER values from the same initial designs for the two step sizes, it is noticed that for the same set of initial guess, a bigger step size may lead to a bigger difference between the best and worst ER in initial design. This bigger difference in initial design indicates that the starting vertices cover a broader region in the parameter space and this helps SSO to go forward in the direction of the optimum, instead of being bounded in a small bad region. The obvious examples are initial guesses numbered 2, 5 and 21. With a small step size, all sets locate the best ER to be around 2.4. While when the step size is doubled, the best ER could be improved to 10.07, 12.68 and 11.19 respectively.

Fig. 7.5 demonstrates the effects of step size on SSO performance. For the same 24 sets of initial guesses and different step sizes, the obtained best ER, E, M_A and the number of vertices required to reach this best response are plotted in Fig. 7.5 (subplots a, b, c and d respectively). With a larger step size, 20 out of the 24 sets (83%) of initial guess will provide better ER (Fig. 7.5(a)), 17 sets (71%) will decrease E (Fig. 7.5(b)), 15 sets (63%) will increase M_A (Fig. 7.5(c)) and 13 sets (54.17%) will decrease the number of vertex moves to reach the best response (Fig.

7.5(d)). Fig. 7.5 shows that step size is important in SSO initial design. For a system without prior knowledge, a bigger step size may be better to start with since the initially designed vertices will cover a broader region in parameter space.

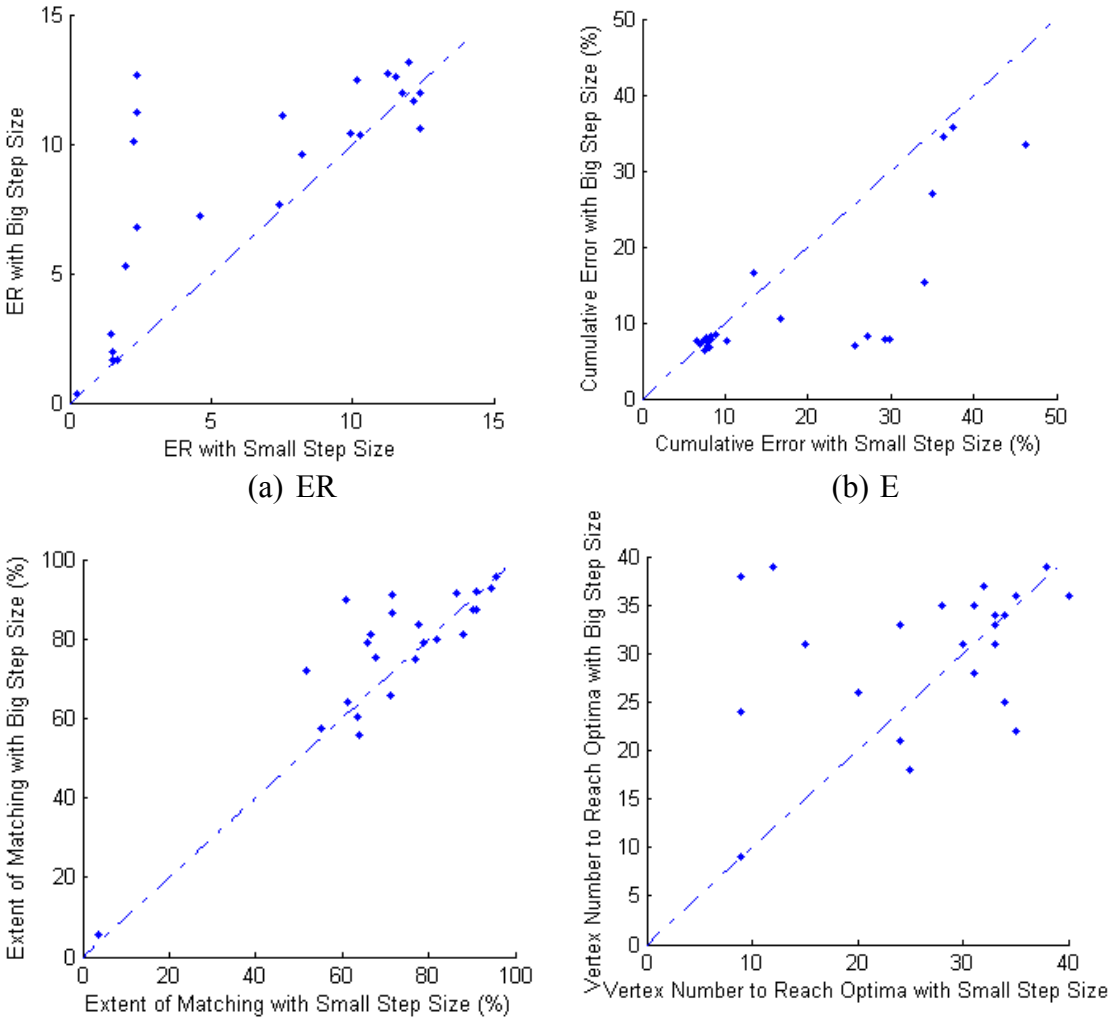

(a) ER (b) E

(c) M_A (d) Number of Vertex to Reach Optima

Figure 7.5. Effect of step size in sequential simplex optimization.

Starting with big step size for random initial guess may be suitable for a system without much prior knowledge. However, for a system where good prior knowledge of optimal parameter region is available, small step size should be applied. For example, the sets numbered 4, 7 and 16 in Table 7.4, the best ERs of initial design

are all above 9.7. This high ER value for the initial design appears to be outcome of an expert estimation of initial guess. All the three sets show that a higher ER can be reached with a smaller step size rather than with large step size. If the initial design vertices are already in the optimal region, a small step size will help to thoroughly search the region and get even better ER response. A big step size may overlook such optimal regions and explore less profitable regions.

Next, the effect of constraints and boundary conditions are investigated.

7.3.2.3 Constraints and Boundary Conditions

Constraints and boundary conditions have to be considered in SSO -- they have to be correctly handled to obtain optimal IA parameters. It is noticed from Table 6.1, that the first 3 parameters (u_1 to u_3) are continuous, while the other 4 parameters (u_4 to u_7) are positive integers (discrete). In SSO movements of reflection, extension and contraction, the new calculated parameters of u_4 to u_7 may often not result in positive integer values. When this happens, the parameters are rounded to the nearest positive integer value. Once a parameter is out of the boundary of parameter space, it will be forced back to the boundary. For example, if the new value for u_5 is calculated to be -1.95, it would be rounded to 1 for the new vertex. Furthermore, when u_4 or u_6 turns out to be 4, the corresponding u_5 or u_7 will be rounded to the nearest positive multiple of 3. These approximations will certainly affect the SSO performance. Even with these approximations and constraints, SSO is still able to come out with “optimal” IA parameters. As shown in Table 7.4, all the results are generated by considering constraints and boundary conditions with necessary approximations.

7.3.2.4 Regions of Good Parameters

The regions of the optimal IA parameters obtained will be compared in this section. As shown in Table 7.4, the studies of SSO with different initial guesses and step sizes have generated several optimal situations (vertices) with high ER. To find out the optimal regions in the parameter space, all the vertices with ER > 11 are plotted, as shown in Fig. 7.6. It is noticed that parameter SE2-Size (u_7) is limited to a small range (from 1 to 4) and SE1-Size (u_5) is confined to the range 4 to 14 (compared to the defined u_7 and u_5 ranges of 1 to 25). The other five parameters cover almost the whole parameter space that is defined in Table 6.1. Fig. 7.6 demonstrates that there are many acceptable good combinations of IA parameters in the parameter space.

With the effect of initial guess, step size, constraints and boundary conditions, SSO is an applicable method to directly search for optimal IA parameters. From Table 7.4, SSO reaches the best ER of 13.13 (Row 23, with initial guess of [0.1, 0.2, 2, 1, 5, 1, 5] and step size of [0.1, 0.1, 0.2, 2, 10, 2, 10]), where the corresponding E and M_A are 7.07% and 92.80% respectively. In Table 7.4, with the 24 sets of initial guess and 2 sets of step size for each set of initial guess, there are total 48 sets of data. 11 sets (22.92%) out these 48 sets can iterate to a better ER than 11.79, the result from the best manual tuned image processing parameters in [31], where $E = 8.0\%$ and $M_A = 94.3\%$. It can be concluded that SSO is a useful approach to directly search for optimal IA parameters. Its shortcoming of attaining the local optima can be overcome by designing several initial guesses.

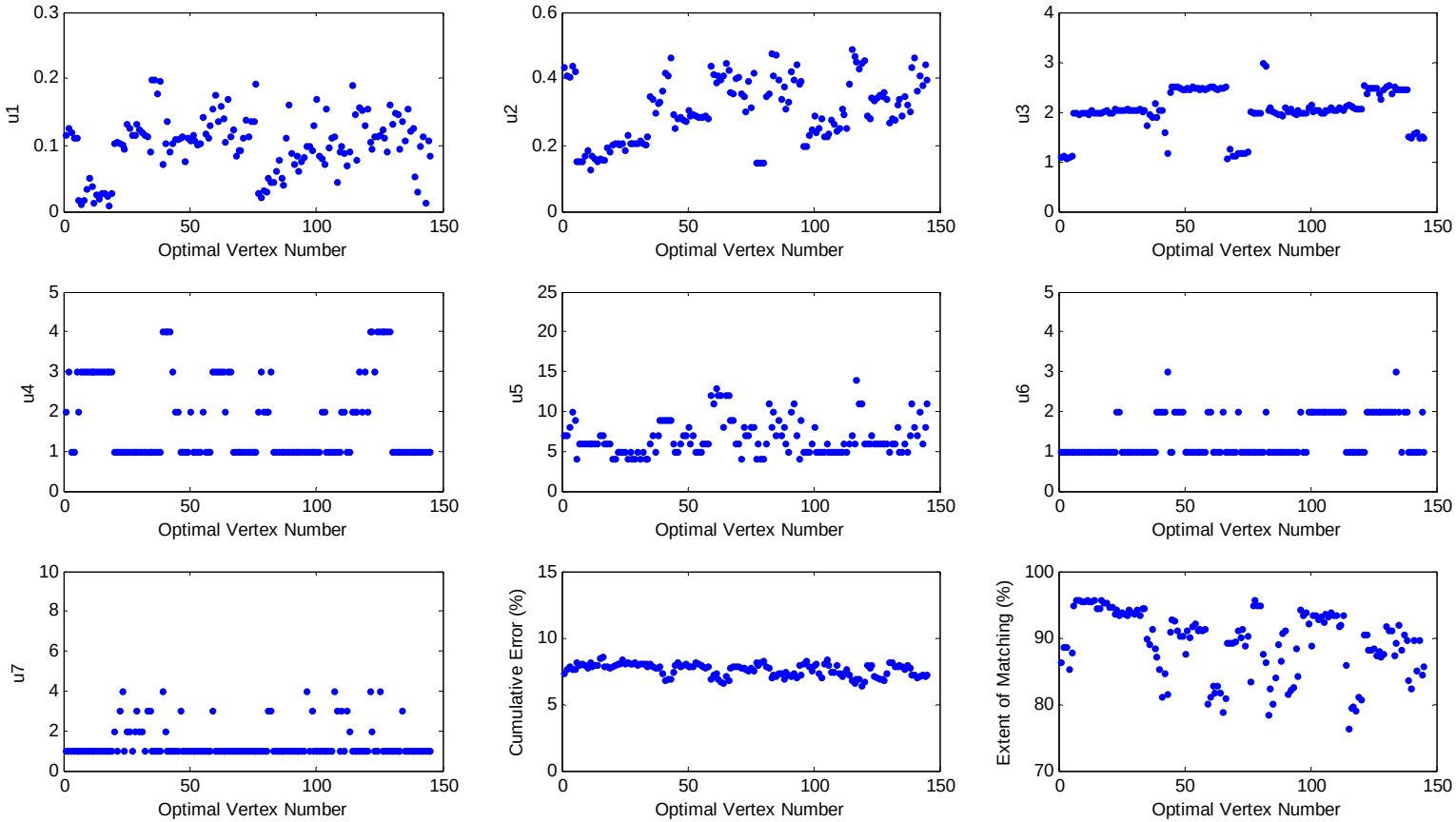

Figure 7.6. IA parameters and responses of all optimal vertexes (With ER>12).

7.3.2.5 Validation of Optimal Parameters Using a New Image Set

With both approaches providing estimation of optimal parameters, the next question is "are they robust?". That is, if the obtained optimal parameters are applied to a new set of images from the same process, are they still optimal or close to optimal parameters? Would the quality of the results change significantly? This is investigated next. As stated in Section 4.3.1, the quality of process images varies with process time (intra-batch variation) and from batch to batch (inter-batch variation) for batch processes. We would like to apply the obtained optimal parameters on a new set of images (2nd set of images) that are acquired from another batch of the same process. From the SSO studies on the 1st set of images, all sets of parameters which yielded ER > 12 are considered as optimal sets of parameters (see Table 7.5) and will be tried on the new set of process images.

In the 2nd set of images, there are 7,878 process images from which 39,031 particles are manually segmented out. Compared to the performance of ER > 12, $6 < E < 8$ and $80 < M_A < 96$ on the first set, the performance with the optimal parameters turns out to be lower: ER drops to a range of 3.5 to 5, with E increasing to between 15 and 20 and M_A decreasing to a 70 – 80 range. When we actually observe the two sets of images, this drop in performance is reasonable. As shown in Fig. 7.7, the first set of images is quite clear with little background noise and it is easy for human and the IA algorithm to segment particles out with a high level of consistency between them. Relatively speaking, the images in the 2nd set have a lot of background noise and it is hard to identify clear boundaries for the particles. This leads to less agreement between IA and human segmentation causing a low ER for

the validation run. Despite the drop in performance on the new set of images, the results are deemed to be good enough for practical application.

Table 7.5 Performance of 1st Set Images' Optimal Parameters on 2nd Set Images

No.	Optimal Parameters							1st Set of Image			2nd Set of Image		
	u1	u2	u3	u4	u5	u6	u7	ER	E	M_A	ER	E	M_A
1	0.03	0.17	2.0	3	6	1	1	12.01	7.96	95.53	4.79	16.37	78.41
2	0.05	0.19	2.0	3	6	1	1	12.37	7.72	95.55	4.85	16.06	77.96
3	0.01	0.17	2.0	3	6	1	1	12.18	7.84	95.47	4.77	16.43	78.31
4	0.02	0.15	2.0	3	6	1	1	12.10	7.91	95.69	4.68	16.72	78.25
5	0.01	0.19	2.0	3	6	1	1	12.11	7.88	95.41	4.87	15.90	77.46
6	0.03	0.18	2.0	3	6	1	1	12.26	7.77	95.33	4.86	15.95	77.45
7	0.09	0.41	1.6	4	9	2	1	12.27	6.91	84.77	3.52	20.35	71.65
8	0.11	0.29	2.4	2	6	1	1	12.17	7.47	90.92	3.87	19.37	75.02
9	0.14	0.40	2.5	3	12	1	1	12.33	6.73	82.91	3.90	18.17	70.91
10	0.11	0.41	2.5	2	8	1	1	12.39	6.60	81.83	3.71	19.00	70.45
11	0.04	0.34	2.0	1	7	1	1	12.17	7.32	89.09	3.74	19.99	74.61
12	0.11	0.38	2.0	1	8	1	1	12.48	6.93	86.50	3.80	19.27	73.25
13	0.16	0.31	1.9	1	6	1	1	12.24	7.41	90.68	4.34	17.37	75.48
14	0.09	0.33	2.1	1	5	1	1	12.50	7.29	91.10	4.62	16.25	75.02
15	0.13	0.25	2.1	1	6	2	1	12.13	7.59	92.09	3.71	20.46	75.88
16	0.08	0.25	2.0	2	5	2	1	12.75	7.33	93.44	4.40	17.55	77.25
17	0.07	0.28	2.1	2	5	2	1	13.13	7.07	92.80	4.57	16.82	76.93
18	0.11	0.28	2.1	1	5	2	4	12.46	7.49	93.32	4.96	15.47	76.76
19	0.05	0.26	2.1	1	5	2	3	12.58	7.46	93.82	4.92	15.63	76.91
20	0.10	0.25	2.1	2	5	2	3	12.74	7.34	93.50	4.88	15.84	77.25
21	0.09	0.31	2.1	2	5	2	1	12.92	7.11	91.85	4.70	16.22	76.18
22	0.07	0.30	2.1	1	6	2	3	12.50	7.36	91.93	4.65	16.36	76.11
23	0.09	0.25	2.0	1	5	2	2	12.23	7.64	93.46	4.47	17.20	76.89
24	0.13	0.45	2.1	3	11	1	1	12.59	6.45	81.24	4.34	16.23	70.42
25	0.16	0.46	2.1	2	6	1	1	12.03	6.72	80.78	4.56	15.27	69.60
26	0.11	0.33	2.5	4	6	2	1	12.40	7.12	88.29	3.83	19.23	73.75
27	0.12	0.35	2.5	4	6	2	4	12.58	7.02	88.35	4.36	17.02	74.24
28	0.12	0.35	2.5	4	6	2	1	12.57	6.95	87.36	3.97	18.47	73.32
29	0.11	0.35	2.4	4	6	2	1	12.63	6.97	88.03	3.95	18.67	73.68
30	0.09	0.36	2.3	4	6	2	1	12.72	6.86	87.26	3.97	18.59	73.79
31	0.16	0.34	2.5	4	6	2	1	12.01	7.30	87.68	3.99	18.35	73.28
32	0.10	0.36	1.6	1	7	1	1	12.68	7.07	89.66	4.14	18.10	75.01
33	0.01	0.38	1.5	1	6	1	1	12.46	7.20	89.64	4.38	17.11	75.00

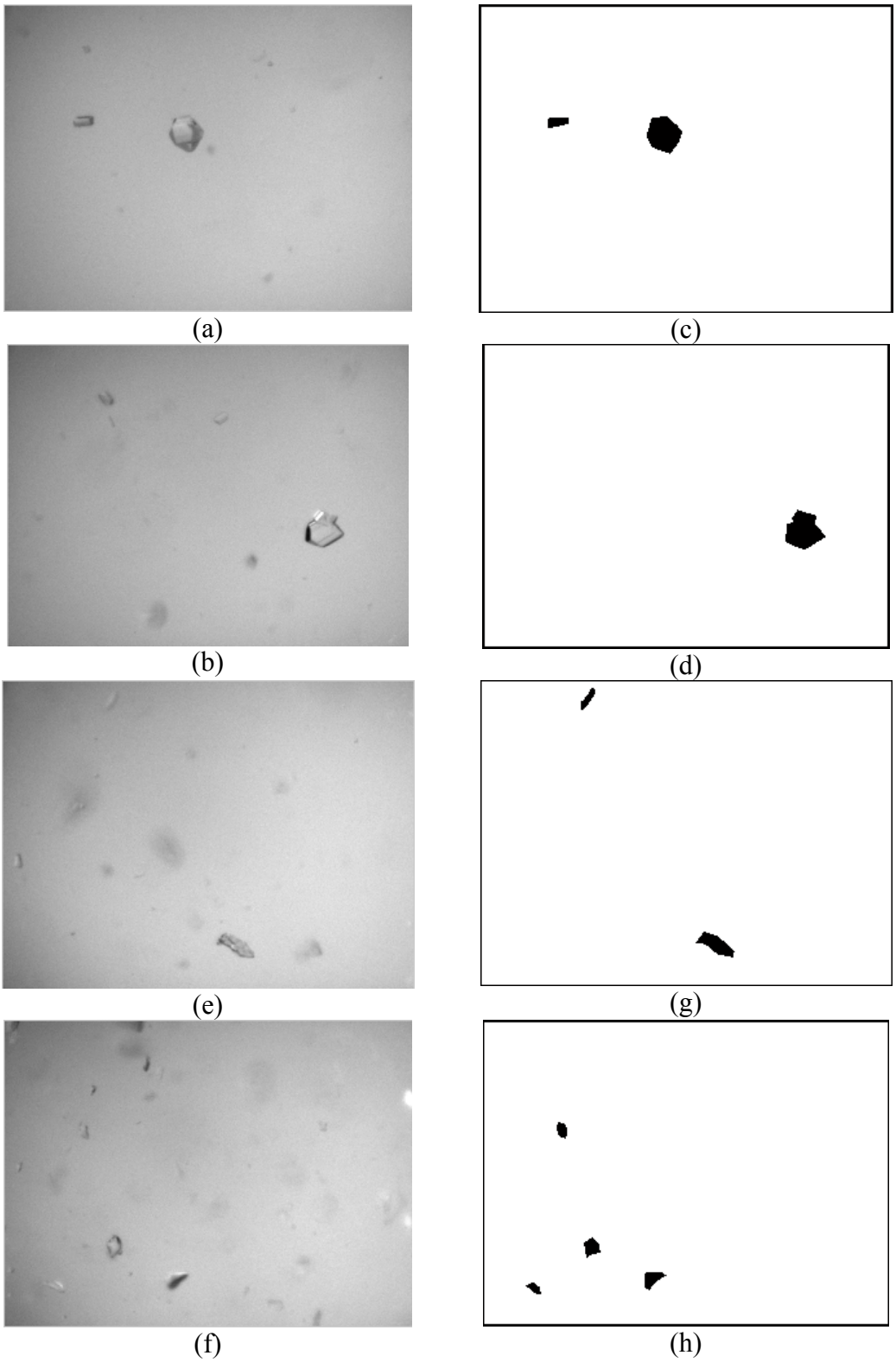

Figure 7.7. Comparison of original image and human segmentation for two image sets. (a-b): original images of 1st image set; (c-d): dorresponding human segmentation of (a-b); (e-f): original images of 2nd image set. (g-h): corresponding human segmentation of (e-f).

To compare IA performance on the two sets of images, we further study the 2nd set of images by applying SSO with the same 23 sets of initial guesses and step sizes as those applied to the 1st set of images. The results obtained with the 2nd set of images (summarized in Table 7.6) are compared to those obtained with the 1st set of images (summarized in Table 7.4). It is noticed that three sets of initial guesses (serial numbers 8, 11 and 17 in Table 7.6) applied to the 2nd set of image converge to a bad point with both small and big step sizes, while one set of initial guess (serial number 15) converges to an unattractive solution with small step size. These sets of initial guesses lead to the similar results as those obtained with the 1st set of images i.e. low ER (high E and low M_A).

The results from other initial guesses are compared. For the 2nd set of images, the obtained optimal ER varies from 2.96 to 6.02, with E varying from 11.47 to 17.24, and M_A varying from 48.84 to 76.47. The required number of vertex explorations to reach the optima varied from 10 to 60. For the 1st set of images, the optimal ER values ranged from 1.68 to 12.72, with E varying from 6.45 to 35.79, and M_A varying from 55.95 to 95.75 and the required number of vertex explorations to reach the optima varied from 9 to 40. It is obvious that with the same initial guess and step size, the results with the 1st set of images are often better than the corresponding results with the 2nd set of images – this further proves the fact that the quality of the 2nd set of images is worse than that of the 1st set of images. The expected performance of optimal IA parameters on the 2nd set of images should be much lower.

Table 7.6: SSO Performance with Different Initial Guess and Step Size (2nd set of images)

	No.	Initial Guess							Step Size [0.05, 0.05, 0.1, 1, 5, 1, 5]						Step Size [0.1, 0.1, 0.2, 2, 10, 2, 10]					
		u1	u2	u3	u4	u5	u6	u7	ER from Initial Design		Best ER Obtained from SSO Iteration				ER from Initial Design		Best ER Obtained from SSO Iteration			
									Best	Worst	ER	E	M_A	Vertex No.	Best	Worst	ER	E	M_A	Vertex No.
Initial Guess from Uniform Design	1	0.25	0.35	2	2	20	2	5	4.14	1.55	5.13	13.39	68.69	45	4.00	1.07	4.97	13.29	66.04	38
	2	0.15	0.45	1	1	20	4	20	2.74	0.03	4.94	12.05	59.48	53	2.84	0.01	6.02	11.47	69.07	43
	3	0.05	0.25	2.5	4	3	1	10	3.93	0.94	4.15	16.18	67.09	53	3.15	0.54	4.47	16.62	74.30	56
	4	0.10	0.25	2.5	1	1	4	3	4.60	0.89	4.85	15.75	76.40	48	3.07	0.48	4.49	15.85	71.23	27
	5	0.10	0.45	1.5	3	15	1	25	0.35	0.04	4.96	14.08	69.75	36	0.45	0.01	4.89	13.53	66.21	41
	6	0.05	0.25	3.5	1	10	1	5	3.18	1.67	4.35	17.01	73.97	52	3.21	1.08	4.34	17.08	74.11	53
	7	0.25	0.45	2.5	4	15	4	3	3.95	2.25	4.15	15.61	64.77	10	3.82	1.74	4.23	15.92	67.32	29
	8	0.20	0.35	3.5	2	25	3	25	0.73	0.11	Converges to ER=0.17				0.22	0.10	Converges to ER=0.17			
	9	0.01	0.25	1	3	25	4	6	1.00	0.16	4.27	13.49	57.63	45	1.00	0.11	5.13	13.06	67.04	60
	10	0.10	0.45	1	2	1	2	5	4.80	0.87	5.44	12.14	66.04	28	4.91	0.34	5.50	12.83	70.58	52
	11	0.20	0.45	2	4	6	3	20	1.43	0.03	Converges to ER = 0.20				0.50	0.03	Converges to ER = 0.20			
	12	0.01	0.55	1.5	4	21	1	15	1.90	1.27	3.86	13.39	51.74	16	2.34	0.64	4.59	14.02	64.36	33
	13	0.10	0.15	2	1	25	1	20	0.37	0.18	4.62	14.08	64.99	40	0.49	0.11	5.36	13.57	72.66	28
	14	0.10	0.55	3	4	9	4	21	1.90	0.02	3.84	16.41	63.01	48	2.03	0.00	3.64	17.24	62.72	33
	15	0.05	0.15	1	3	1	3	25	0.08	0.00	Converges to ER = 0.00				0.10	0.00	5.57	12.88	71.80	32
	16	0.01	0.15	2	4	6	2	1	4.66	0.74	4.75	16.09	76.47	24	4.68	0.44	5.03	14.77	74.33	43
	17	0.25	0.55	3	1	1	3	15	0.54	0.09	Converges to ER = 0.20				0.70	0.09	Converges to ER = 0.21			
	18	0.20	0.45	3	1	15	1	10	2.80	2.13	4.64	14.73	68.32	34	2.88	1.35	4.44	16.09	71.39	28
	19	0.15	0.55	3.5	3	25	2	1	2.46	1.36	3.21	16.20	51.96	45	2.25	1.28	2.96	16.49	48.84	54
	20	0.01	0.05	3	1	20	3	10	0.14	0.04	3.92	16.58	64.96	31	0.30	0.04	4.41	16.80	74.04	48
	21	0.05	0.35	3	3	5	2	20	0.76	0.02	3.61	16.99	61.35	51	0.94	0.00	4.77	15.29	72.91	53
	22	0.01	0.55	2	2	5	4	9	4.38	0.73	5.22	12.95	67.65	37	4.23	0.30	5.35	13.32	71.25	58
Random Guess	23	0.1	0.2	2	1	5	1	5	4.92	2.84	5.37	14.12	75.82	32	5.18	1.65	5.38	13.90	74.83	51

By further examining the results in Tables 7.4 and Table 7.6, several sets of initial guesses (serial numbers 1, 3, 4, 10, 16 and 23) that lead to good IA results on the 1st set of images also lead to optimal results on the 2nd set of images. This certifies that the optimal IA parameters on the 1st set of images are also optimal to the 2nd set of images. Hence, the robustness of the developed approach is verified.

7.3.3 Comparison of the Two Optimization Methods

The results presented earlier show that both integration methods, i.e. model-based optimization with SSO, or adopting designed experimental runs as initial guess for SSO, are capable of systematically finding out optimal sets of parameters. Both integration methods could locate optimal parameter sets with ER greater than 12.5.

The model-based optimization with uniform design approach employed a total 106 runs of experiments to determine and verify the optimal value for the parameters. In UD designs, the experiments cover the full parameter space and there is no need for initial guess. The modeling step clearly relates the input parameters and output response using mathematical relationships, which render them convenient for further analysis. The main disadvantage of this method is at the modeling step. Building reliable and robust models particularly with limited experimental data is always a challenge. When the number of parameters (factors) is increased, the number of experimental runs required for model development will increase as well. Overall, UD is a suitable method to find reasonably good IA parameters and its performance

will depend significantly on the built models.

With proper initial guess, the SSO method is able to locate optimal sets of parameters within a few iterations. Since each step is based on actual "experimental" runs, the obtained results are direct, clear and need no separate validation step. The drawback is that it generates comparatively less process knowledge. Also, SSO is a local optimization method and the initial guesses and choice of step size are very important.

One can envisage ways to integrate the two methods. Combining the two methods will overcome the disadvantages of each individual method and improve the efficiency. As shown in this chapter, SSO can be applied to determine the optimal parameter values from the generated models in the model-based optimization with UD. This is very efficient and saves time especially for complex models. On the other hand, UD can be applied to generate the initial guesses to provide multiple start points for the SSO.

Overall, any of the two optimization methods discussed here or their integration could be employed to systematically locate optimal IA parameters for huge sets of images obtained from crystallization processes. The obtained optimal IA parameters will offer a reliable estimate of the state of the process via on-line image analysis and ensure improved process operation and constant product quality via monitoring and control.

7.4 Conclusion

The integration of two optimization approaches, model-based optimization with uniform design and direct sequential simplex search optimization, have been successfully applied to systematically optimize image processing parameters for a large set of batch process images. Since the quality of images from batch crystallization processes suffers from both intra- and inter-batch variability, automated methods such as those proposed here can be quite useful in identifying the best IA parameters. Our studies show that both the methods considered here are capable of finding optimal sets of IA parameters for use in real-time crystallization applications.

The obtained IA parameters are robust and this implies better image processing results for on-line process monitoring and control. The optimal parameters obtained from one set of process images are able to provide good performance on another set of images that are acquired from another batch of the same process. This indicates that the proposed methodology is highly suited for real-time monitoring and control of crystallization processes.

Chapter 8. Conclusions and Future Works

8.1 Conclusions

On-line monitoring of particle shape and size distribution through image-based approaches is a challenge in the pharmaceutical and fine chemical industries. This thesis focused on improving the accuracy of the results which can be obtained using currently available image processing algorithms. We have shown that there is a noticeable difference between the true particle size as seen under the microscope and that extracted from PVM images even with manual segmentation. PVM images lead to an estimated particle size that is about 11% less than that obtained from microscopy analysis, possibly because of the random orientation of the particles during in-situ imaging. Despite this significant measurement error, it should facilitate particle size identification using PVM because of the numerous benefits and potential advanced control applications that easy, real-time size measurements would entail.

We have also sought to quantify the errors introduced by automated image analysis. Basic image analysis is well-established in literature. However, its accuracy in any application depends significantly on various parameters that have to be pre-specified

by the user. We have used manual segmentation of the image as a basis for evaluating the results from automated image analysis. We have proposed two metrics – extent of matching and cumulative error – to compare automated and manual segmentations. These serve as a quality measure to evaluate the effect of various parameters. Our results show that although all image analysis parameters have some effect, the two structuring elements in morphology operation step are the most important. These determine the shape information of the objects (particles) to be extracted from the image. Our study reveals that, for segmenting needle-shaped MSG particles, the diamond and square are the most suited structuring elements. Further study is required to establish the generality of this conclusion to other systems.

We have also shown that when tuned suitably, automated image analysis can extract particle sizes with high accuracy (about 4-8% error) which is similar to that obtained by manual segmentation. Image analysis using the PVM system is therefore a reasonably accurate approach to track particle growth. At the initial stage of working with a new system, we need to manually segment particles from one experimental run and establish an optimal set of parameters for PVM based image processing. This is achieved by systematically perturbing the IA parameters based on the theory of design of experiments. In production plants where a large number of similar crystallization runs would be carried out, despite the high one-time cost of manual segmentation, the large benefits incurred from a certifiably accurate particle-size distribution available in real-time would make the proposed scheme attractive.

We have shown that a systemic procedure for IA parameter optimization would reduce the parameter optimization effort so as to make it attractive in the first context as well. The integration of two optimization approaches, model-based optimization with uniform design and direct sequential simplex search optimization have been successfully applied to systematically optimize image processing parameters for a large set of batch process images. Since the quality of images from batch crystallization processes suffer from both intra- and inter-batch variability, automated methods such as those proposed here can be quite useful in identifying the best IA parameters. Our studies show that both the methods considered here are capable of finding optimal sets of IA parameters for use in real-time crystallization applications.

The obtained IA parameters are robust and this implies better image processing results for on-line process monitoring and control. The optimal parameters obtained from one set of process images are able to provide good performance on another set of images that are acquired from another batch of the same process. This indicates that the proposed methodology is highly suited for real-time monitoring and control of crystallization processes.

8.2 Future Work

Each image processing methodology has its own advantages and limitations, some are good at eliminating certain types of noise whereas they fail with other types of noise. Any reasonable image processing methodology will accurately segment particles that are clearly imaged. It would be desirable to locate these clearly imaged,

as well as accurately segmented, particles by integrating two or more image processing methodologies. Currently, IA works well to segment single particles that have obvious boundaries, while additional improvement, such as further image enhancement, segment particles from overlapped or aggregated clots by solidity filter or rectangle shrinking methods, is required to segment particles that do not have clear boundaries in the images. This methodology also needs to be improved to process images taken from high solid concentration solutions in crystallization processes. More effort is needed to develop new methodologies for image based sensors, such as manually building a particle template library from a set of training images and using this library to identify particles in future process images. Furthermore, among the available in-situ sensors, each instrument has its advantages and limitations. Hence, calibration for all kinds of sensors is required to get a more accurate in-situ measurement. Once an accurate and reliable imaging sensor is developed, it can be used for closed loop control of particulate processes.

8.2.1 Segment-Based Image Fusion

Each image processing methodology follows a sequence of image processing steps and its success depends on the choice of a number of parameters at each step. The optimal sets of parameters could be manually tuned by intuitively observing the segmentation result, or automatically tuned by quantitatively comparing the segmentation result with that of manual segmentation. Whichever approach is adopted, manpower and time are required. This investment can be significant for a large set of images with different background and quality. Human observation or segmentation for the whole set of images may not be feasible. Thus, new image

processing methodologies that are reliable, robust and require less manual work are desired.

Furthermore, no matter how optimal the parameters are set, each image processing methodology has its advantages and limitations. As already pointed out, some may be good at eliminating certain types of noise while may fail with other types of noise. For example, an image processing methodology may identify the bubbles with bright light reflection as particles, while another image processing methodology may segment the darker noisy background objects as particles. Such false segmentation and identification will certainly affect the accuracy and reliability in characterizing particle size from in-process images. The question is how to make sure the segmented objects are the needed representative particles. A representative particle should be a whole particle with accurate outline and area in the image. Due to the complexity of process images, the typical errors that occur with image analysis include: (i) a big particle being segmented as few small objects, (ii) a few overlapped particles being identified as a big object, (iii) a clear particle being affected by process noise and segmented as an object with irregular shape, and (iv) some bubbles, background and lighting effects may be identified as objects, etc.

When two or more image processing methodologies are applied to process the same set of process images, it is found that they can accurately segment particles that are clearly imaged. However, they may result in different segmentations for noisy objects and particles that do not have clear outlines in the image. As shown in Fig. 8.1, different image processing methodologies (IA and Multivariate Image Analysis (MIA)) may segment different objects from the same process image. Among these

objects, most of them are clear particles, while some objects are particles that could not be clearly imaged and some objects are just noise, bubbles or other uncertainties that should not be accounted for. Nevertheless, both methods could correctly segment out the particles that have clear outline. If an object could be identified by multiple image processing methodologies, it should be a well imaged particle with clear outlines. These particles could be selected as representative particles and they are more reliable in characterizing particle size and shape.

As an immediate future work, we propose to identify the clearly imaged representative particles by fusing the segmentations from different image processing methodologies. More reliable and accurate particle characterization is expected from these representative particles. Two fusion methods, feature-based image fusion (FBF) and region-based image fusion (RBF), are being investigated currently to identify these representative particles. Both fusion methods are developed with 5 sets of sea sand images and further verified with images from MSG seeded batch cooling crystallization. When the fusion results are compared with those of manual segmentation, significant improvement in measurement of PSD and hourly median particle size could be obtained.

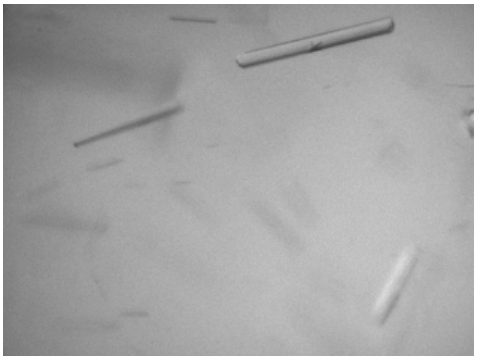

(a) PVM image #20143

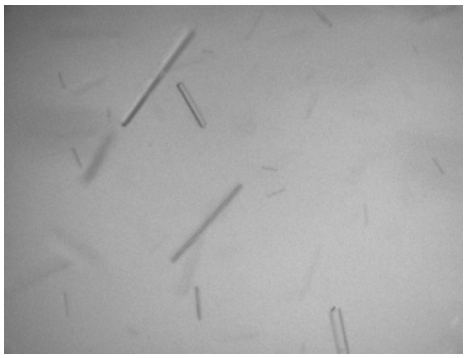

(a') PVM image #19980

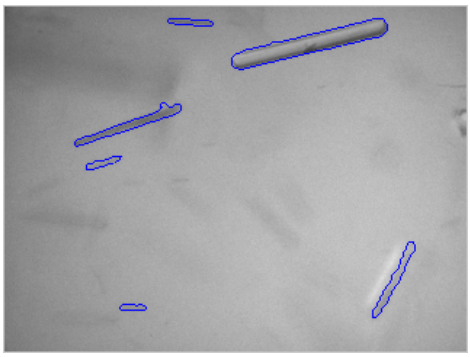

(b) IA segmentation

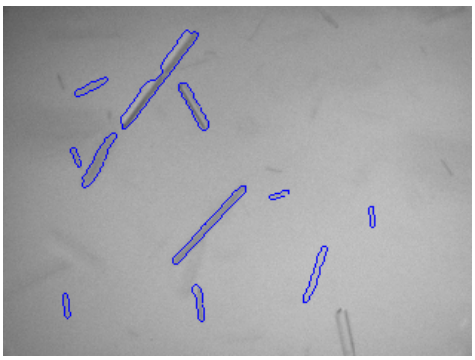

(b') IA segmentation

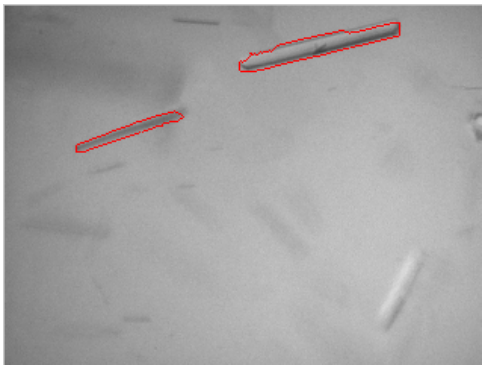

(c) MIA segmentation

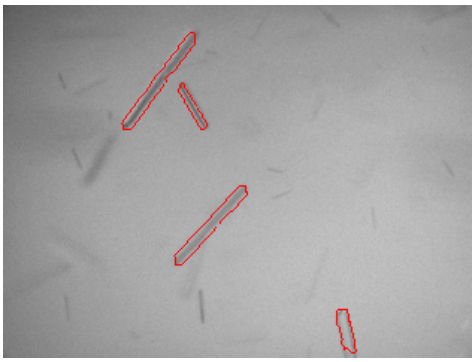

(c') MIA segmentation

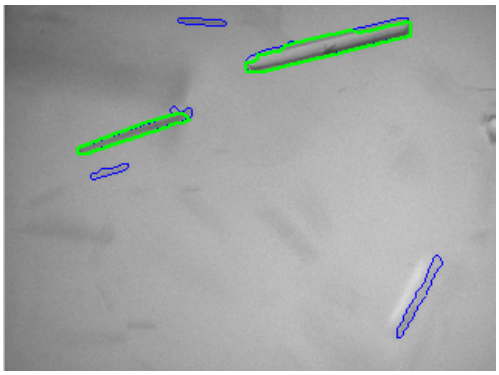

(d) clear particles are identified by both IA & MIA

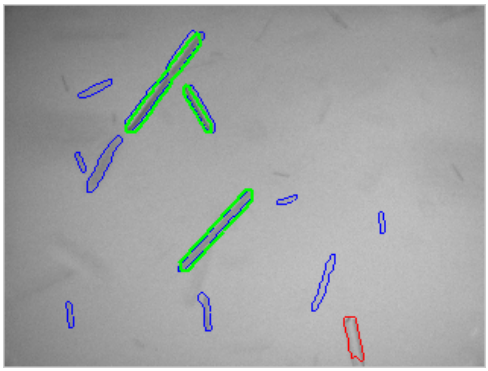

(d') clear particles are identified by both IA & MIA

Figure 8.1. Clearly imaged representative particles can be identified by multiple image processing methodologies.

The estimated PSD from the 5 sets of sea sand images (as described in section 4.2.1) are plotted in Fig. 8.2 (a), (b), (c), (d) and (e) respectively. It is obvious that IA has identified too many small particles and its estimated PSD would not match with that of the template for any of the 5 sets of images. MIA performs better than IA, especially for Set A, the PSD estimated by MIA is comparable with that of the template. While for the other four sets, MIA also identifies too many small particles and its estimated PSDs shows mismatch with those of the templates. However, both fusion results show a great improvement in estimating PSD, where the estimated PSDs are almost the same as those of the templates for all the 5 sets of images. FBF and RBF are capable of improving the accuracy of PSD estimation for all the 5 sets of sea sand images.

From the images acquired from MSG seeded cooling crystallization process (as described in section 4.2.2), PSD estimates obtained at 4-hour intervals by different image processing methodologies are compared with those of Template 2 (as stated in section 6.1), as shown in Fig. 8.3. In the beginning 4 hours of process time, IA, MIA, FBF and RBF could estimate PSD, which match closely with that of Template 2. With advancing process time, there will be more and more big particles, Template 2 will have less and less fraction of small particles in its PSD. It is obvious that IA and MIA are not able to follow this trend, because they always tend to have high fraction of small. However, the FBF and RBF are able to follow Template 2's PSD trend quite well throughout. This result reflects that the two fusion methods are effective to select representative particles from IA and MIA segmentations, which leads to a more accurate PSD estimation.

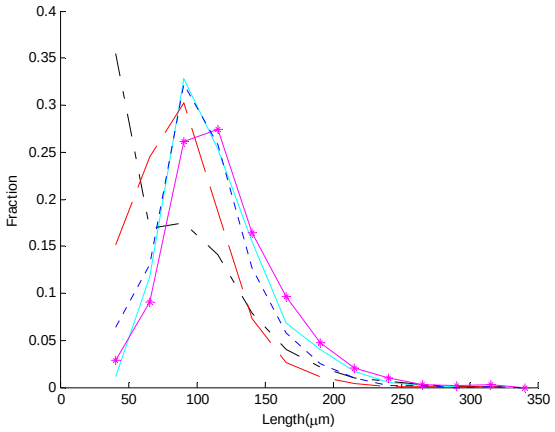

(a) Set A

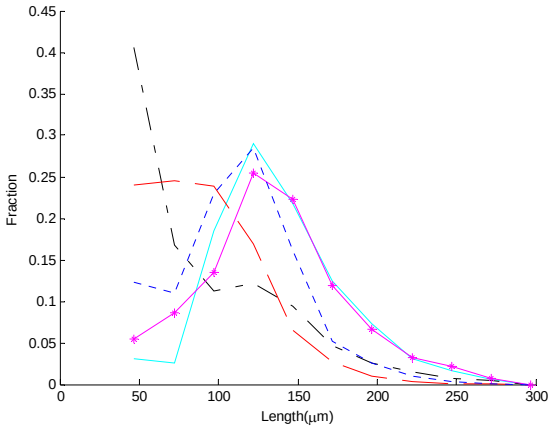

(b) Set B

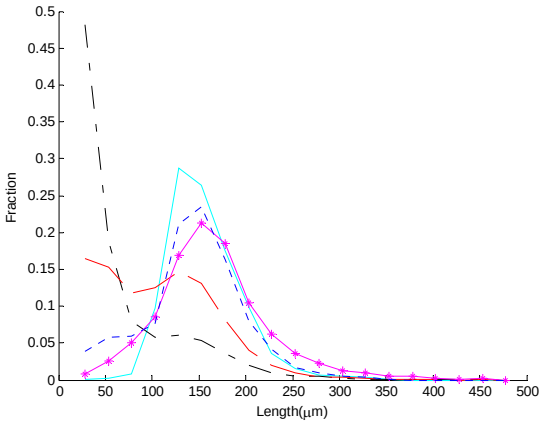

(c) Set C

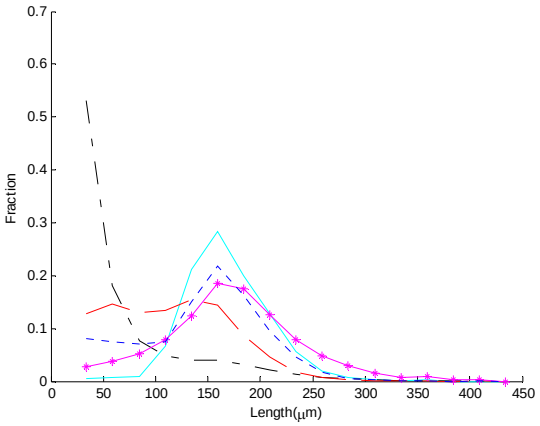

(d) Set D

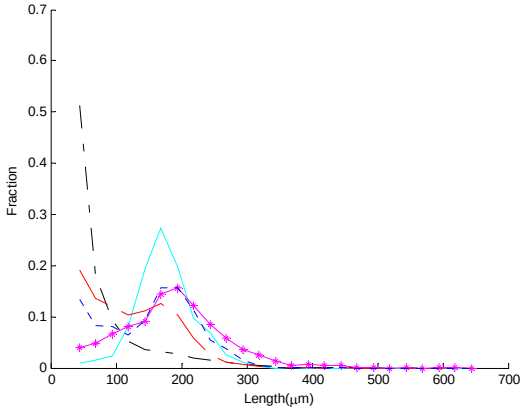

(e) Set E

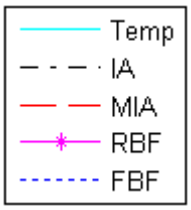

(f) Legend for subplot

Figure 8.2. Estimated PSD for 5 sets of sea sand images.
(a), (b), (c), (d) and (e) demonstrate the estimated PSD for 5 sets of sea sand images. For each set, the PSD estimated by Template, IA, MIA, Region-Based Fusion and Feature-Based Fusion are plotted.

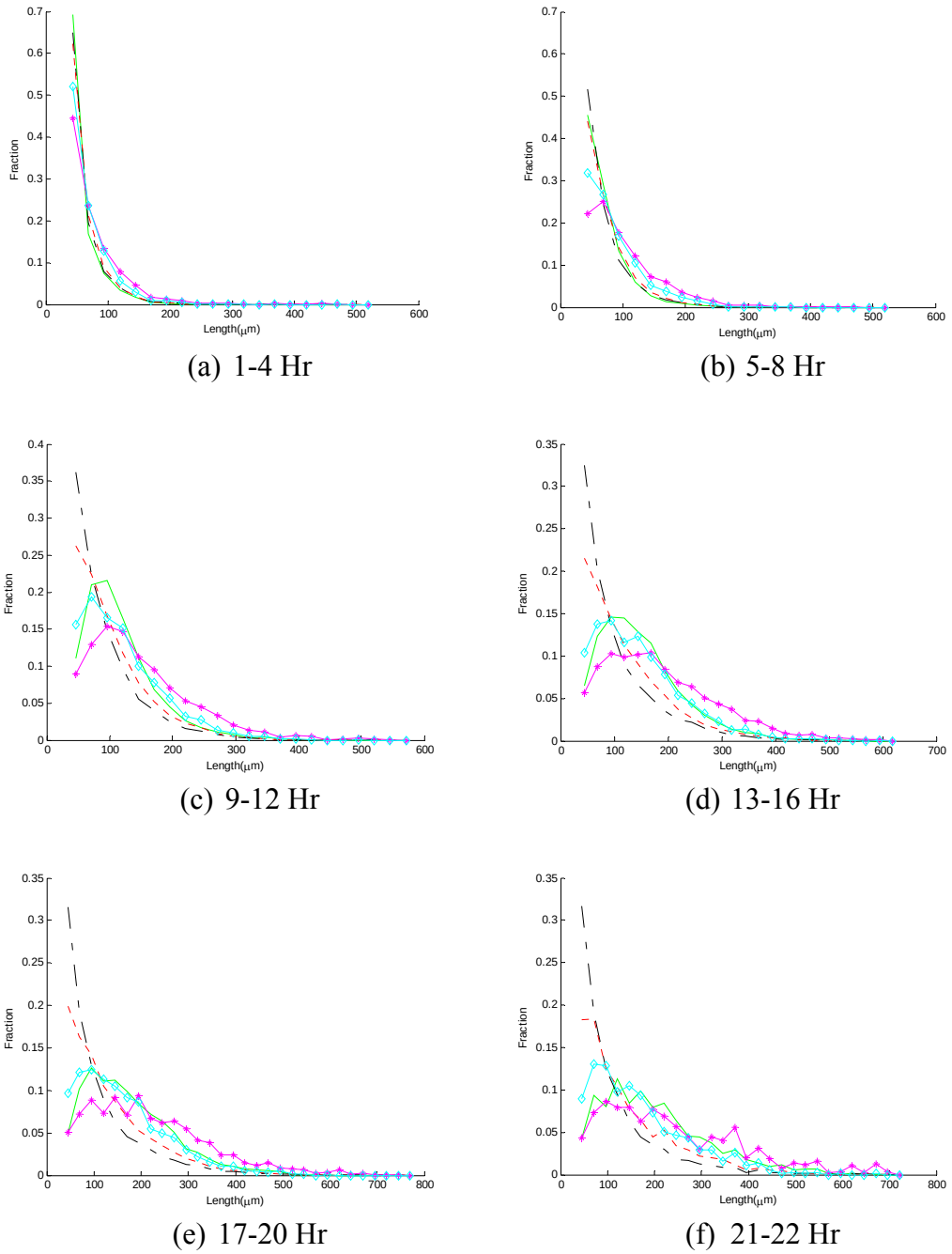

(a) 1-4 Hr (b) 5-8 Hr

(c) 9-12 Hr (d) 13-16 Hr

(e) 17-20 Hr (f) 21-22 Hr

Figure 8.3. Improvement in PSD estimation for MSG seeded cooling crystallization obtained by fusing the segmentations from IA and MIA. Each subplot is for the hours shown in the caption of each subfigure. Legend of each subplot is shown in Fig. 8.2(f).

8.2.2 Further Methods for Particle Segmentation

For clear images in which particles have clear outlines, IA works well to segment out particles. However, the acquired images are with complex situations: i) the particle's outline in the image are usually not so clear, ii) a few particles may overlap or agglomerate together, and iii) process noise and bubbles may affect the quality of PVM images. Under these circumstances, the particles could not be accurately segmented. Further processing is required. We are currently looking on designing a *solidity filter* to get rid of the objects that are not in desired particle shape. After that, a rectangle shrinking approach to cut out the stand out stings to the particle.

Solidity Filter

From the image processing steps described in Section 2.4 and Chapter 3, it is common to obtain a particle's boundary as shown by the blue borders in Fig. 8.4. A convex polygon enclosing it could be obtained as shown by the red borders. Solidity of the identified object is defined as:

Solidity = (Area of Object) / (Area of Convex Polygon)

= (Area included by blue boarder)/(Area included by red border) (8.1)

For a well segmented particle, it is observed that it will have a regular shape and the bounding polygon will fit well. Thus, its solidity value should be quite high. For a badly segmented particle, the bounding polygon cannot fit the object tightly and the solidity value would be low. As shown in Fig. 8.5, (a) and (a') are the original PVM images, (b) and (b') show the segmented particles, (c) and (c') show the segmented

particles with solidity value greater than 0.8. It can be observed that the particles with irregular shape are ignored and will not be considered for further processing. Further work is needed to see if the use of solidity filter provides more accurate PSD.

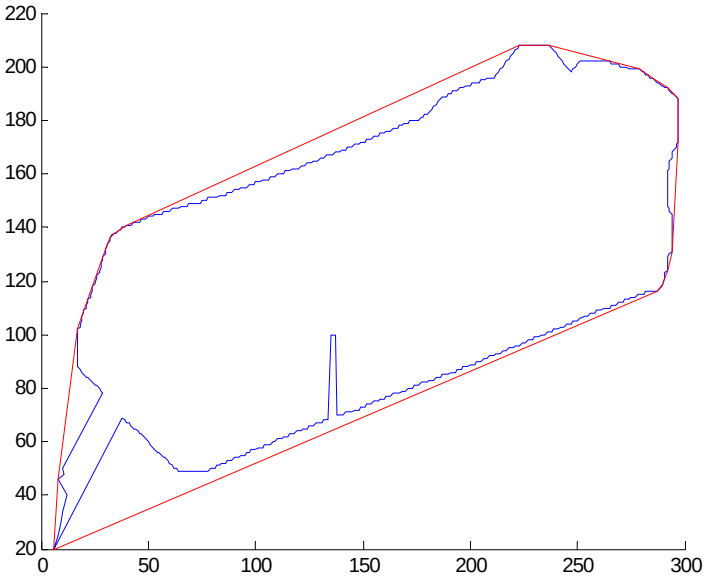

Figure 8.4. The segmented particle & its boundary box.

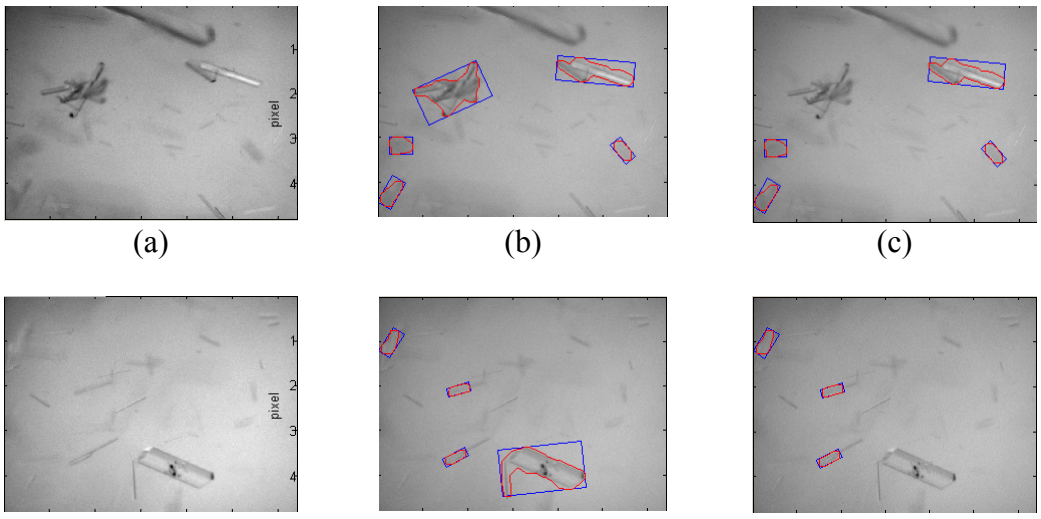

Figure 8.5. Application of solidity filter to ignore particles with irregular shapes. (a) and (a') are the original PVM images; (b) and (b') show the segmented particles; (c) and (c') show the segmented particles with solidity value greater than 0.8.

Shrink Bounding Box

Another common problem in particle segmentation is that an excess part, such as an extra sting, is attached to the particle (See Fig. 8.6(a)). To handle this type of segmentation artifacts, we would like to shrink the bounding rectangle to make it a better fit to the shape of a single particle and cut out the excess part.

(a) Original segmented particle with sting

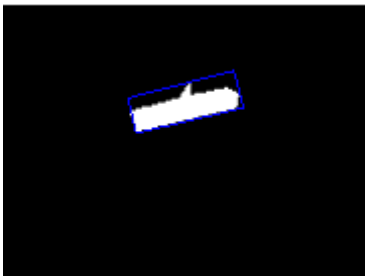

(b) Original segmented particle fit to a bounding box

(b) Rotate image (a) to make the major axis of the particle align with the horizontal direction

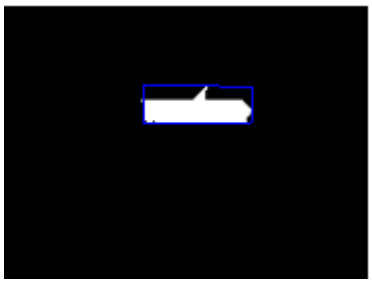

(d) Rotate image (b) to make particle in horizontal direction

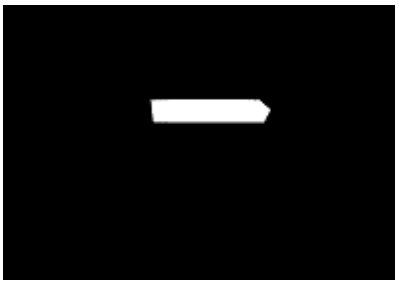

(e) Shrink bounding box to cut out the sting on the particle

Figure 8.6. Single particle segmentation by shrinking bounding box.

In this approach, the image is rotated to make sure that the major axis of the particle being processed is parallel to x-axis. Then each pixel inside the rectangle bounding

box is scanned line by line and the number of pixels in each line labeled as being occupied by particle is recorded. If the number is lower than the threshold limit, this line should be deleted from the object area. This step is repeated until all the lines are scanned. Fig. 8.6(b) shows the original noisy particle and its bounding box, after rotation (Fig. 8.6(c)), and deleting the lines whose percentage of object pixels to background pixels is equal or less than 10% (Fig. 8.6(d)). The final result is shown in Figure 8.6(e).

8.2.3 Improving the Methodology to Analyze Complex Images

PVM images taken from high solid concentration crystallization processes may exhibit non-uniform background and contain highly aggregated particles that are difficult to recognize. The background "noise" may also be high. Figure 8.7 gives samples of such images. The first image has many long needle shaped crystals that are highly aggregated; the image does not have a high object-to-background contrast and it is hard to segment the crystals out. The second image has a very dark and blur red background and a few clear crystals in light colour can be identified. The third image also has many long needle-shaped crystals, but it is relatively easier to segment the crystals out compared to image 1 because image 3 has a relatively high object-to-background contrast, the needle-shaped crystals are not as long as those in image 1 and the crystals are not highly aggregated. The forth image depicts a polymorph transition process from diamond-shaped crystals to needle-shaped crystals, and this will cause difficulties in recognizing particles in different shapes since the morphology operation identifies particles according to the pre-defined shape of an object.

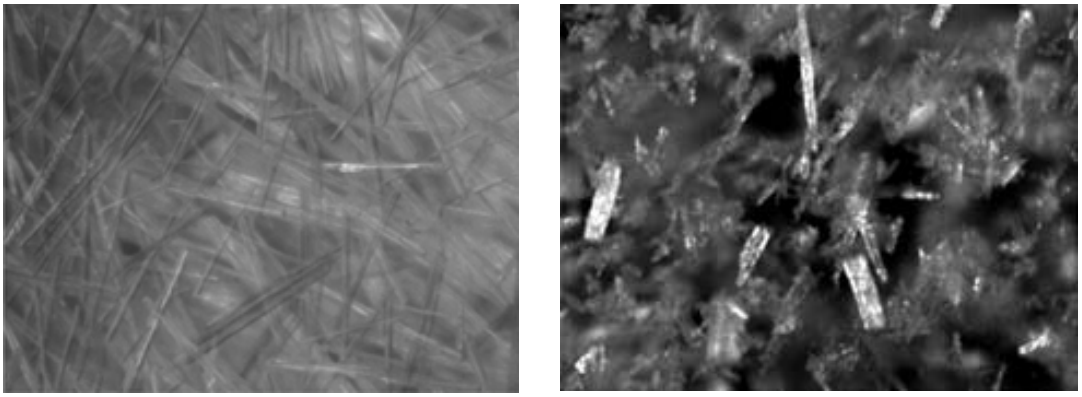

(a) Image 1 (b) Image 2

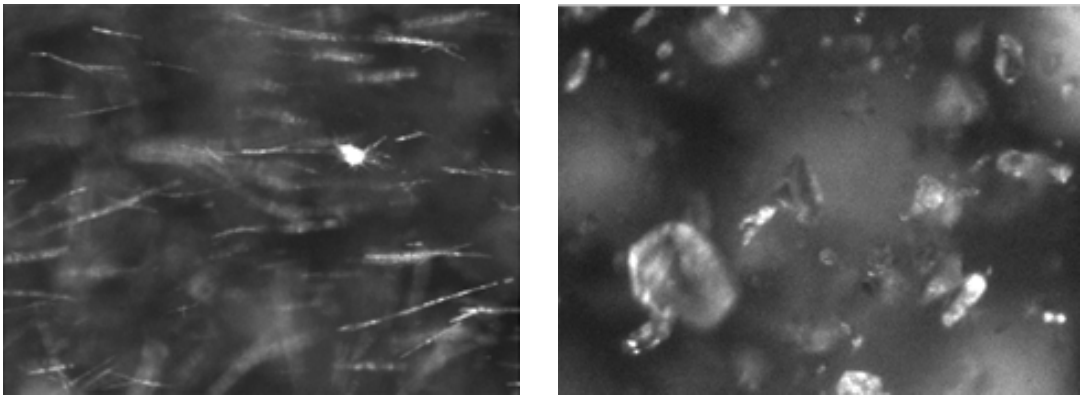

(c) Image 3 (d) Image 4

Figure 8.7. Samples for 4 sets of complex images.

By fine tuning the IA parameters, IA can process the type of images that are similar to image 2, 3 and 4 to segment particles, as shown in Fig. 8.8. However, it fails for image 1 due to the low object-to-background contrast and high aggregation of solid crystals.

Observing image 1, there are many long needle-shaped crystals and the main idea is to find all lines in the images by Hough transform and cluster the parallel lines that fall within a short distance. Figure 8.9 shows an example of each step in this method. Canny edge detection is first applied to find the clear boundaries, Hough transform is then applied to find all the lines and finally line clustering is used to segment long lines. There are some difficulties in this method, such as defining the distance

between two lines to decide if they should be clustered together. In some cases, the distance between two lines belonging to the same particle is longer than the distance between two lines belonging to two different particles and this will cause either over-clustering or under-clustering. In some images, the clear crystals are not identified while artifacts are sometimes identified as crystals. The step causing this mistaken identification is the Hough transform, which transforms the edge information into distance and angle. Further work is needed to develop a practical method for this kind of images.

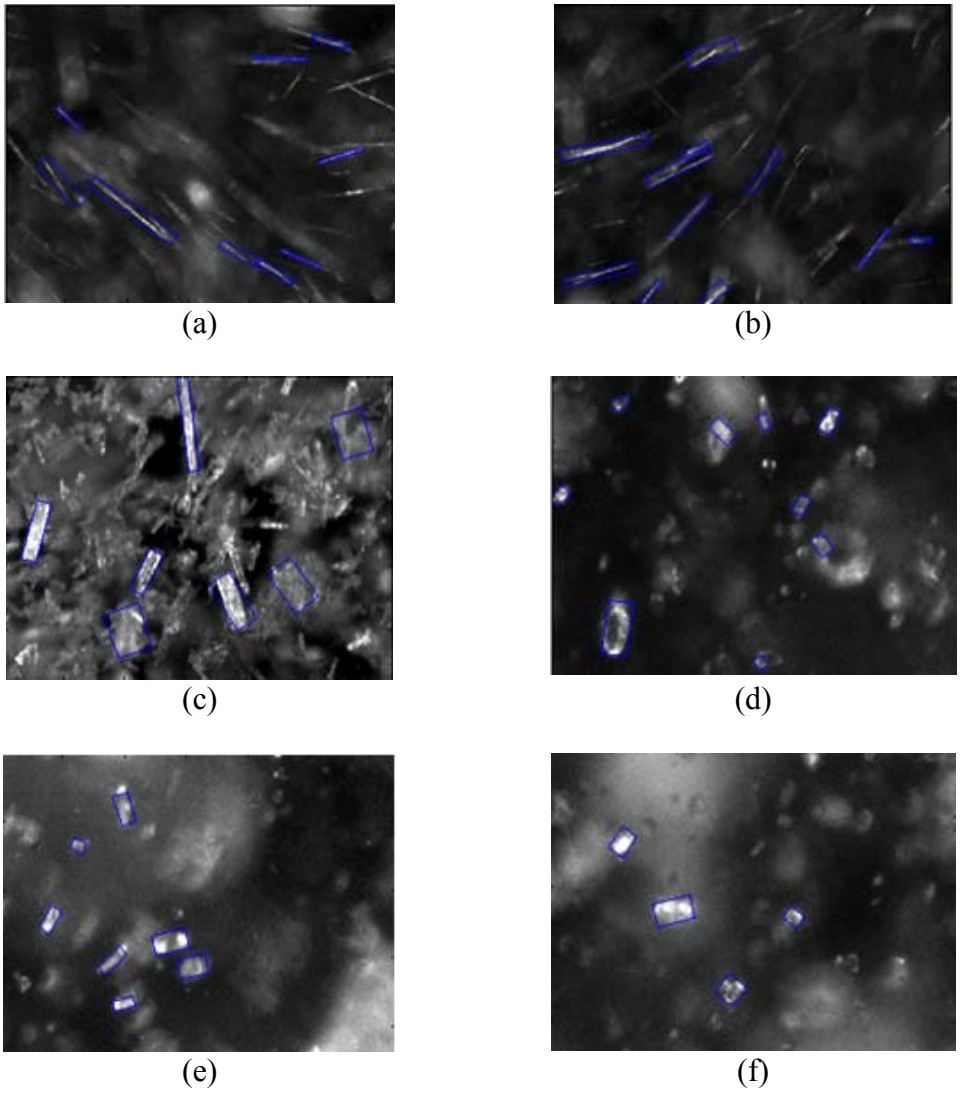

Figure 8.8. IA segments particles from the type of images that are similar to images 2, 3 & 4 in Fig. 8.7.

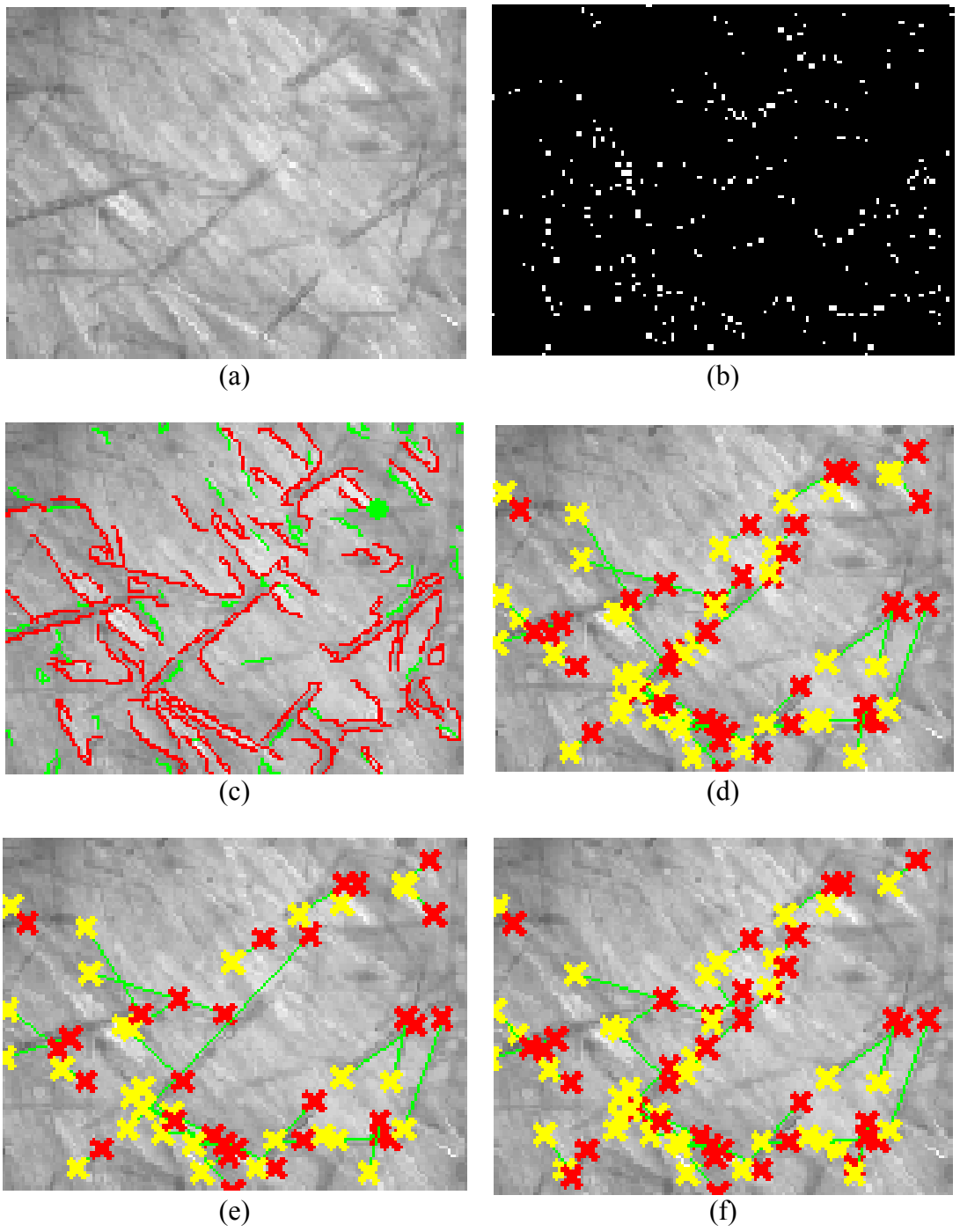

Figure 8.9. Identify long needle-shape particles by finding lines.
(a) original image; (b) edge detection; (c) boundary; (d) lines identified by Hough transform; (e) clustered lines; (f) segmented particles.

8.2.4 Calibrating the Measurements of Microscope, FBRM and PVM

Both PVM and FBRM are applied to the experiments conducted in chapter 4. PVM and microscope measurements of 5 sets of sea sand samples in DI water are also compared. There is some difference among the measurements since the measuring methods and conditions are different. FBRM measures particle chord length and the difference between chord length and actual particle size depend on particle shape. PVM measures particle size and shape, but the sampling rate and representation of particles will affect its accuracy. Microscope measures both particle shape and size with higher accuracy, but most often is used offline and it has to be manually operated. It is required to calibrate the measurements of microscope, FBRM and PVM, so that the on-line measurements with FBRM and PVM can be accurate and reliable.

8.2.5 New Methodology: Using Manually Built Templates

Currently published methodologies of image based sensors are quite specific to certain systems. Thus, they can only be used to analyze images with high-aspect-ratio crystals. Methods still need improvement to be able to analyze more complex images with overlapped or aggregated particles.

In future, it may be worthwhile to develop a template based method to be used as a general methodology to identify particles from on-line images. A template library could be built by manually identifying particles from a series of test experimental

images. The manually built template library could function as training data for pattern recognition to identify particles from images for future crystallization processes. The more particles there are in the library, the better it will be for pattern recognition and PSD estimation in future rans. Hopefully, this methodology can identify particles even in challenging systems (e.g. when solid concentration is high).

8.2.6 Closed Loop Control of Crystallization Processes Using Image-Based Sensors

Currently, image based sensors are commonly used for process monitoring or open loop process control. Monitoring particle polymorphic transformation using image based sensors is one of the most common applications in particulate processes.

As future work, one might pursue closed loop control of particulate processes by quantifying the particle size and shape distributions online. A schematic diagram of this is as shown in Fig. 4.2. Product quality variables, such as particle shape, size and size distribution, would be the controlled variables. Temperature, pressure, super-saturation, flow rate for continuous or semi-batch process, cooling rate for cooling crystallization, etc. would be the manipulated variables.

Data driven approaches have been very successful in the chemical and related industries to monitor processes, detect abnormalities and pinpoint problem sources. Based on the data of past crystallization experiments, one can develop monitoring systems that are capable of detecting the process fault(s) early and identify the fault

components so that an early control decision can be made. A reliable monitoring system can increase product quality, reduce product cost and improve overall business productivity. Development of such systems based on data from traditional and image based sensors would be very interesting and useful for crystallization processes. Multiway principal component analysis may be used in this regard.

Bibliography

Adar, F., Naudin, C. & Whitley, A., (2004), Case studies in the application of Raman microscopy. Raman Technology for Today's Spectroscopists, June 2004, 22-29.

Alatalo, H., Kohonen, J., Qu, H., Hatakka, H., Reinikainen, S.-P., Louhi-Kultanen, M. & Kallas, J., (2008), In-line monitoring of reactive crystallization process based on ATR FTIR and Raman spectroscopy. Journal of Chemometrics, 22, 644-652.

Aldridge, P. K., Evans, C. L., Ward, H. W., II, and Colgan, S. T., (1996), Near-IR detection of polymorphism and process-related substances. Anal. Chem., 68, 997-1002.

Al-Zoubi, N., Koundourellis, J. E. & Malamataris, S., (2002), FT-IR and Raman spectroscopic methods for identification and auantitation of orthorhombic and monoclinic paracetamol in powder mixes. Journal of Pharmaceutical and Biomedical Analysis, 29, 459-467.

Barrett P., B. Smith, J. Worlitschek, V. Bracken, B. O'Sullivan, and D. O'Grady, (2005), A review of the use of process analytical technology for the understanding and optimization of production batch crystallization processes. Org. Process Res. Dev., 9, 348-355

Barrett, P. & Glennon, B., (2002), Characterizing the metastable zone width and solubility curve using lasentec FBRM and PVM. Chemical Engineering Research and Design 80, 799-805.

Birch M., S. J. Fussell, P. D. Higginson, N. McDowall, and I. Marziano, (2005), Towards a PAT-based strategy for crystallization development. Org. Process Res. Dev., 9, 360-364.

Borissova, A., Khan, S., Mahmud, T., Roberts, K. J., Andrews, J., Dallin, P., Chen, Z-P. & Morris, J., (2009), In situ measurement of solution concentration during the batch cooling crystallization of L-glutamic acid using ATR-FTIR spectroscopy coupled with chemometrics. Crystal Growth & Design, 9(2), 692-706.

Bovik, A., (2000), Handbook of image and video processing. Academic Press, 45-50.

Braatz, R. D., (2002), Advanced control of crystallization processes. Annual Reviews in Control 26, 87-99.

Bugay, D.E., (2001), Characterization of the solid-state: spectroscopic techniques. Advanced Drug Delivery Reviews 48, 43-65.

Bujak, B. & Bottlinger, M., (2008), Three-Dimensional measurement of particle shape. Part. Part. Syst. Charact., 25, 293-297.

Calderon De Anda, J., Wang, X. Z., Lai, X. & Roberts, K. J., (2005a), Classifying organic crystals via in-process image analysis and the use of monitoring charts to follow polymorphic and morphological changes. Journal of Process Control 15, 785-797.

Calderon De Anda, J., Wang, X. Z., Lai, X., Roberts, K. J., Jennings, K. H., Wilkinson, M. J., Watson, D. & Roberts, D., (2005b), Real-time product morphology monitoring in crystallization using imaging technique. AIChE Journal 51, 1406-1414.

Calderon De Anda, J., X. Z. Wang & K. J. Roberts, (2005c), Multi-scale segmentation image analysis for the in-process monitoring of particle shape with batch crystallisers. Chemical Engineering Science 60, 1053-1065.

Campbell Roberts, S. N., Williams, A. C., Grimsey, I. M. & Booth, S. W., (2002), Quantitative analysis of mannitol polymorphs. FT-Raman spectroscopy. Journal of Pharmaceutical and Biomedical Analysis, 28, 1135-1147.

Canny, J., (1986), A computational approach to edge detection. IEEE Transaction on Pattern Analysis and Machine Intelligence, 8(6), 679-698.

Carlsohn, M. F., (2005), Spectral imaging in real-time – Imaging principles and applications. Real-Time Imaging, 11, 71-73.

Chaudhuri, D. & Samal, A., (2007), A simple method for fitting of bounding rectangle to closed regions. Pattern Recognition 40 (2007), 1981-1989.

Chen, H. & Wu, C., (2004), An algorithm of image processing for underwater range finding by active triangulation. Ocean Engineering, 31, 1037-1062.

Chen, Z-P., Morris, J., Borissova, A., Khan, S., Mahmud, T., Penchev, R. & Roberts, K.J., (2009), On-line monitoring of batch cooling crystallization of organic compounds using ATR-FTIR spectroscopy coupled with an advanced calibration method. Chemometrics & Intelligent Laboratory Systems, 96, 49-58

Chesi, G., (2009), Camera Displacement via constrained minimization of the algebraic error. IEEE Trans. Pattern Analysis and Machine Intelligence, 31, 370-375.

Darakis, E., Khanam, T., Rajendran, A., Kariwala, V., Naughton, T. J. & Asundi, A. K., (2010), Microparticle characterization using digital holography. Chemical Engineering Science, 65, 1037-1044.

Dellamonica, D. Jr., Silva, P. J. S., Humes, C., Hirata, N. S. T. & Barrera, J., (2007), An exact algorithm for optimal MAE stack filter design. IEEE Trans. Image Processing, 16, 453-462.

Duda, R., & Hart, P., (1972), Use of the Hough trnasformation to detect lines and curves in pictures. Commun. ACM, 15-1:11-15.

Eggers, J., Kempkes, M. & Mazzotti, M., (2008), Measurement of size and shape distributions of particles through image analysis. Chemical Engineering Science 63(22), 5513-5521.

Eggers. J., Kempkes, M., Cornel, J., Mazzotti. M., Koschinski, I. & Verdurand, E., (2009), Monitoring size and shape during cooling crystallization of ascorbic acid. Chemical Engineering Sciences 64(1), 163-171.

Findlay, W. P. & Bugay, D. E., (1998), Utilization of Fourier Transform-Raman spectroscopy for the study of pharmaceutical crystal forms. Journal of Pharmaceuticla and Biomedical Analysis, 16 921-930.

Franco, O., Reck, G., Orgzall, I., Schulz, B. W. & Schulz, B., (2003), Characterization of a new non-centrosymmetric polymorph of Diphenyl-1, 3, 4-Oxadiazole. Journal of Molecular Structure, 649, 219-230.

Fujiwara, M., Chow, P. S., Ma, D. L. & Braatz, R. D., (2002), Paracetamol crystallization using laser backscattering and ATR-FTIR spectroscopy: metastability, agglomeration and control. Cryst. Growth Des., 2, 363-370.

Gonzalez, R.C. & Woods, R.E., (1992), Digital image processing, Addison-Wesley, Reading, MA.

Gonzalez R.C., & Woods, R.E., (2001), Digital image Processing, 2nd Edition, Prentice Hall.

Gonzalez, R. C., Woods, R. E. & Eddins S. L., (2004), Digital image using Matlab processing, Pearson Prentice Hall, USA.

Haleblian, J. & McCrone, W., (1969), Pharmaceutical applications of polymorphism. J. Pharm. Sci. 58(8), 911-929.

Heath, A. R., Fawell, P. D., Bahri, P. A. & Swift, J. D., (2002), Estimating average particle size by focused beam reflectance measurement (FBRM). Part. Part. Syst. Charact. 19, 84-95.

Hogan, S. E. and Buckton, G., (2001), The application of near infrared spectroscopy and dynamic vapor sorption to quantify low Amorphous contents of crystalline lactose. Pharmaceutical Research, 18(1), 112-116.

Hojjatoleslami, S.A., & Kittler, J., (1998), Region growing: a new approach, IEEE Transactions on Image Processing 7(7), 1079-1084

Hukkanen, E. J. & Braatz, R. D., 2003, Measurement of particle size distribution in suspension polymerization using in situ laser backscattering. Sensor and Sctuators B 96, 451-459.

Kamoun, A., Jaziri, M. & Chaaouni, M., (2009), The use of the simplex method and its derivatives to the on-line optimization of the parameters of an injection moulding process. Chemometrics and Intelligent Laboratory Systems, 96, 117-122.

Kempkes, M., Eggers, J. and Mazzotti, M., (2008), Measurement of particle size and shape by FBRM and in situ microscopy. Chemical Engineering Science, 63(19), 4656-4675.

Kempkes, M., Vetter, T. & Mazzotti, M., (2010), Measurement of 3D particle size distributions by stereoscopic imaging. Chemical Engineering Sciences 65, 1362-1373.

Kenny, F. J., (1997), Design of Experiments techmiques solve difficult production problem. Scientific Computing & Automation, July (1997), 21-24.

Langkilde, F. W., Sjoblom, J., Tekenbergs-Hjelte, L. & Mrak, J., (1997), Quantitative FT-Raman analysis of two crystal forms of a pharmaceutical compound. Journal of Pharmaceutical and Biomedical Analysis, 15, 687-696.

Larsen, P.A., Patience, D. B. & Rawlings, J. B. (2006a), Industrial crystallization process control. IEEE Control Systems Magazine, 26(4):70-80.

Larsen, P.A., Rawlings, J.B. & Ferrier, N.J. (2006b), An algorithm for analyzing noisy, in situ images of high-aspect-ratio crystals to monitor particle size distribution. Chemical Engineering Science 61, 5236-5248.

Larsen, P.A., Rawlings, J.B. & Ferrier, N.J. (2007), Model-based object recognition to measure crystal size and shape distributions from in situ video images. Chemical Engineering Sciences 62, 1430-1441.

Larsen, P. A. & Rawlings, J. B., (2009), The potential of current high-resolution imaging-based particle size distribution measurements for crystallization monitoring. AICHE Journal, 55(4), 896-905.

Lewiner F., Klein, J. P., Puel, F. & Fevotte G., (2001), On line ATR FTIR measurement of supersaturation during solution crystallization processes, calibration and applications on three solute/solvent systems. Chemical Engineer Sciences, 56, 2069-2084.

Li, R. F., Renchev, R., Ramachandran, V., Roberts, K. J., Wang, X. Z., Tweedie, R. J., Prior, A., Gerritsen, J. W. & Hugen, F. M., (2008), Particle shape characterisation via image analysis: from laboratory studies to in-process measurements using an in situ particle viewer system. Organic Process Research & Development, 12, 837-849.

Li, R. F., Thomson, G. B., White, G., Wang, X. Z., Calderon De Anda, J. & Roberts, K. J., (2006), Integration of crystal morphology modeling and on-line shape measurement. AIChE Journal, 52(6), 2297-2305.

Liang, Y., Fang, K. & Xu, Q., (2001), Uniform design and its applications in chemistry and chemical engineering. Chemometrics and Intelligent Laboratory Systems, 58, 43-57.

Liotta, V. & Sabesan, V., (2004), Monitoring and feedback control of supersaturation using ATR-FTIR to produce an active pharmaceutical ingredient of a desired crystal size. Org. Process Res. Dev., 8, 488-494.

Lucas, Y., Domingues, A., Driouchi, D. & Treuillet, S., (2006), Design of experiments for performance evaluation and parameter tuning of a road image processing chain. EURASIP Journal on Applied Signal Processing, 1-10.

Luner, P. E., Majuru, S., Seyer, J. J. & Kemper, M. S., (2000), Quantifying crystalline form composition in binary powder mixtures using near-infrared reflectance spectroscopy. Pharmaceutical Development and Technology, 5(2), 231-246.

Ma, C. Y., Wang, X. Z. & Roberts, K. J., (2007), Multi-dimensional population balance modeling of the growth of rod-like L-glutamic acid crystals using growth rates estimated from in-process imaging. Advanced Powder Technol., 18(6), 702-723.

Mao, S. & Kanungo, T., (2001), Empirical performance evaluation methodology and its application to page segmentation algorithms. IEEE Trans. Pattern Analysis and Machine Intelligence, 23, 242-256.

Martin, D., Fowlkes, C., Tal, D. & Malik, J., (2001), A database of human segmented natural images and its application to evaluating segmentation algorithm and measuring ecological statistics. In Proc. 8th Int'l Conf. Computer Vision, 416-423.

Matsopoulos, G. K., Mouravliansky, N. A., Delibasis, K. K. & Nikita, K. S., (1999), Automatic retinal image registration scheme using global optimization techniques. IEEE Trans. Information Technology in Biomedicine, 3, 47-60.

Morel, S. & Adar, F., (2005), Refined raman spectroscopy bringing new insight into industrial processes. Optics & Photonics News, June 2005, 42-46.

Moynihan, H. A. & O'Hare, I. P., (2002), Spectroscopic characterisation of the monoclinic and orthorhombic forms of paracetamol. International Journal of Pharmaceutics, 247, 179-185.

Murphy, B. M., Prescott, S. W. & Larson, I., (2005), Measurement of lactose crystallinity using Raman spectroscopy. Journal of Pharmaceutical and Biomedical Analysis, 38, 186-190.

Myerson, A.S., (2002), Handbook of industrial crystallization, Butterworth-Heinemann.

Nere, N. K., Ramkrishna, D., Parker, B.E., Bell III, W.V., and Mohan, P., (2007), Transformation of the chord-length distributions to size distributions for nonspherical particles with orientation bias. Ind. Eng. Chem. Res., 46, 3041-3047.

O'Brien, L. E., Timmins, P., Williams, A. C. & York, P., (2005), Use of in situ FT-Raman spectroscopy to study the kinetics of the transformation of carbamazepine polymorphs. Journal of Pharmaceutical and Biomedical Analysis 36 (2005) 335-340.

Ono, T., ter Horst, J. H., & Jansens, P. J., (2004), Quantitative measurement of the polymorphic transformation of L-Glutamic acid using in-situ Raman spectroscopy. Crystal Growth & Design, 4(3), 465-469.

Patience, D. B., (2002), Crystal engineering through particle size and shape monitoring, modeling and control. University of Wisconsin-Madison, PhD Thesis.

Patience, D. B. & Rawlings, J. B., (2001), Particle-shape monitoring and control in crystallization processes. AIChE Journal, 47, 2125-2130.

Pelletier, M. J., (2003), Quantitative analysis using Raman spectrometry. Focal Point, 57(1).

Pirzadeh, H., (1999), The rotating calipers as a tool in computational geometry. McGill University, Canada. Master thesis.

Pollanen, K., Hakkinen, A., Reinikainen, S. P., Louhi Kul Tanen, M. & Nystrom, L., (2005), ATR-FTIR in monitoring of crystallization processes: comparison of indirect and direct OSC methods, Chemometrics and Intelligent Laboratory Systems, 76, 25-35.

Pratiwi, D., Fawcett, J. P., Gordon, K. C. & Rades, T., (2002), Quantitative analysis of polymorphic mixtures of ranitidine hydrochloride by Raman spectroscopy and principle components analysis. European Journal of Pharmaceutics and Biopharmaceutics, 54, 337-341.

Pratt, W.K., (1991), Digital image processing, 2nd ed., Wiley, New York.

Qu, H., Louhi-Kultanen, M. & Kallas, J., (2006), In-line image analysis of the effects of additives in batch cooling crystallization. Journal of Crystal Growth, 289, 286-294.

Quirk, M. & Serda J., (2002), Semiconductor manufacturing technology, Prentice Hall.

Ramtanen, J., Wikstrom, H., Rhea, F. E. & Taylor, L. S., (2005), Improved understanding of factors contributing to quantification of anhydrate/hydrate powder mixtures. Applied Spectroscopy, 59(7), 942-951.

Rao, R. K., Tun, K. & Lakshminarayanan, S., (2009), Genetic programming based variable interaction models for classification of process and biological systems. Industrial and Engineering Chemistry Research, 48, 4899-4907.

Rosenfeld, A., & Kak, A.C., (1982), Digital picture processing, 2nd ed., Vol. 1, Academic Press.

Ruf, A., Worlitschek, J. & Mazzotti, M., (2000), Modeling and experimental analysis of PSD measurements through FBRM, Particle and Particle Systems Characterization, 17(4), 167-179.

Samant, K. D. & O'Young, L., (2006), Understanding crystallization and crystallizers. Chemical Engineering Progress, 102 (10), 28-37.

Sarkar, D., Doan, X. T., Zhou, Y. & Srinivasan, R., (2009), In-situ particle size estimation for crystallization processes by multivariate image analysis. Chemical Engineering Science, 64, 9-19.

Sasic, S., Clark, D. A., Mitchell, J. C. & Snowden, M. J., (2005), Analyzing Raman maps of pharmaceutical products by sample-sample two-dimensional correlation. Applied Spectroscopy, 59(5), 630-638.

Schőll, J., Bonalumi, D., Vicum, L., & Mazzotti, M., (2006), In situ monitoring and modeling of the solvent-mediated polymorphic transform of L-glutamic acid. Crystal Growth & Design, 6(4), 881-891.

Scholl, J., Vicum, L., Muller, M. & Mazzotti, M., (2006b), Precipitation of L-glutamic acid: determination of nucleation kinetics. Chemical Engineering and Technology, 29(2), 257-264.

Scott, D. M. & McCann H., (2005), Process imaging for automatic control. Taylor & Francis.

Scott, E. U., (2005), Computer imaging: digital image analysis and processing. Taylor & Francis.

Simon, L. L., Nagy, Z. K. & Hungerbuhler, K., (2009a), Endoscopy-Based in situ bulk video imaging of batch crystallization processes. Organic Process Research & Development. Special Issue on Polymorphism and Crystallization 13, 1254-1261.

Simon, L. L., Nagy, Z. K. & Hungerbuhler, K., (2009b), Comparison of external bulk video imaging with focused beam reflectance measurement and ultra-violet visible spectroscopy for metastable zone identification in food and pharmaceutical crystallization processes. Chemical Engineering Sciences 64, 3344-3351.

Simon, L. L., Oucherif, K. A., Nagy, Z. K. & Hungerbuhler, K., (2010a), Bulk video imaging based multivariate image analysis, process control chart and acoustic signal assisted nucleation detection. Chemical Engineering Science 65, 4983-4995.

Simon, L. L., Oucherif, K. A., Nagy, Z. K. & Hungerbuhler, K., (2010b), Histogram matching, hypothesis testing and statistical control chart assisted nucleation detection using bulk video imaging for optimal switching between nucleation and seed conditioning steps. Industrial & Engineering Chemistry Research 49, 9932-9944.

Starbuck, C., Spartalis, A., Wai, L., Wang, J., Fernandez, P., Lindemann, C. M., Zhou, G. X. & Ge, Z., (2002), Process optimization of a complex pharmaceutical polymorphic system via in situ Raman spectroscopy. Crystal Growth & Design, 2(6), 515-522.

Stephenson, G. A., Forbes, R. A. and Reutzel-Edens, S. M., (2001), Characterization of the solid state: quantitative issues. Advanced Drug Delivery Reviews 48, 67-90.

Taner, M. T. & Sezen, B., (2007), Taguchi's experimental design method on improvement of medical image quality. Leadership in Health Services, 20, 42-51.

Togkalidou, T., Tung, H. H., Sun, Y. K., Andrews, A. & Braatz, R. D., (2002), Solution concentration prediction for pharmaceutical crystallization processes using robust chemometrics and ATR FTIR spectroscopy. Org. Process Res. Dev., 6, 317-322.

Toussaint, G. T., (1983), Solving geometric problems with the rotating calipers. Proceedings of IEEE MELECON'83, Athens, Greece.

Trivedi, Y. C. & Kurz, L., (1992), An experimental design approach to image enhancement. IEEE Trans. Systems, Man and Cybernetics, 22, 805-813.

Vehring, R., (2005), Red-excitation dispersive Raman spectroscopy is a suitable Technique for solid-state analysis of respirable pharmaceutical powders. Applied Spectroscopy, 59(2), 286-292.

Verran, G. O., Mendes, R. P. K. & Dalla Valentina, L. V. O., (2008), DOE applied to optimization of aluminum alloy die castings. Journal of Materials Processing Technology, 200, 120-125.

Wall, M. H., De Noble, L. & Hartman, R., (2005), Raman microanalysis in the forensic laboratory: identification and characterization of suspect solids, liquids, and powders. Spectroscopy, special issues, Jun 2, 2005.

Walters, F. H., Parker, Jr. L. R., Morgan, S. L. & Deming, S. N., (1999), Sequential Simplex Optimization. Multisimplex AB, Sweden.

Wan, J., Wang, X. Z. & Ma, C. Y., (2009), Particle shape manipulation and optimization in cooling crystallization involving multiple crystal morphological forms. AICHE Journal, 55(8), 2049-2061.

Wang, W., (2006), Image analysis of particles by modified Ferret method – best-fit rectangle. Powder Technology 165, 1-10.

Wang, X. Z., Calderon De Anda, J. & Roberts, K. J., (2007), Real-time measurement of growth rates of individual crystal facets using imaging and image analysis a feasibility study on needle-shaped crystals of L-glutamic acid. Chemical Engineering Research and Design, 85(A7): 921-927.

Wang, X. Z., Roberts, K. J. & Ma, C., (2008), Crystal growth measurement using 2D and 3D imaging and the perspectives for shape control. Chemical Engineering Science 63, 1173-1184.

Wanibe, Y. & Itoh, T., (1998), New quantitative approach to powder technology. John Wiley & Sons.

Website: http://www.math.hkbu.edu.hk/UniformDesign, 2004.

Webster, S. & Baldwin, K. J., (2005a), Raman spectroscopy for pharma. Part1: principles and applications. Pharmaceutical Technology Europe. Cleveland: Jun 2005, 17(6), 46-51.

Webster, S. & Baldwin, K. J., (2005b), Raman spectroscopy for pharma. Part II: Raman as a PAT tool. Pharmaceutical Technology Europe. Cleveland: Aug 2005, 17(8), 30-35.

Welch, A., Hallett, W., Marsden, P. & Bromiley, A., (2003), Accurate attenuation correction in PET using short transmission scans and consistency information. *IEEE Trans. Nuclear Science,* 50, 427-432.

Wikstrom, H., Lewis, I. R. & Taylor, L. S., (2005), Comparison of sampling techniques for in-line monitoring using Raman spectroscopy. Applied Spectroscopy, 59(7), 934-941.

Wilkinson, M. J., Jennings, K. H. & Hardy, M., (2000), Non-invasive video imaging for interrogating pharmaceutical crystallization. Microscopy and Microanalysis 6 (Supplement), 996-997.

Worlitschek, J., (2003), Monitoring, modeling and optimization of batch cooling crystallization. Swiss Federal Institute of Technology Zurich, PhD thesis.

Wu, W., Shaw, P., Ruan, J., Spence, F. J. & Wildsmith, S. E., (2005), Experimental designs for optimisation of the image analysis process for cDNA microarrays. Chemometrics and Intelligent Laboratory Systems, 76, 175-184.

Xia, Z., Huang, X., Zhou, X., Sun, Y., Ntziachristos, V. & Wong, S. T. C., (2008), Registration of 3-D CT and 2-D flat images of mouse via affine transformation. IEEE Trans. Information Technology in Biomedicine 12, 569-578.

Yamashita, F., Itoh, T., Yoshida, S., Haidar, M. K. & Hashida, M., (2010), A novel multi-dimensional visualization technique for understanding the design parameters of drug formulations. Computers and Chemical Engineering, 34, 1306-1311.

Yocky, D. A. & Jakowatz, Jr. C. V., (2007), Shift-scale complex correlation for wide-angle coherent cross-track SAR stereo processing. IEEE Trans. Geoscience and Remote Sensing, 45, 576-583.

Yu, H. & MacGregor, J. F., (2003), Digital imaging for online monitoring and control of industrial snack food processes. Ind. Eng. Chem. Res., 42, 3036-3044.

Yu, L. X., Lionberger, R. A., Raw, A. S., D'Costa, R., Wu, H. & Hussain, A. S. (2004). Applications of process analytical technology to crystallization process. Advanced Drug Delivery Reviews, 56, 349-369.

Yu, Z. Q., Chow, P. S. & Tan, R. B. H., (2006a), Application of attenuated total reflectance-fourier transform infrared (ATR-FTIR) technique in the monitoring and control of anti-solvent crystallization. Ind. Eng. Chem. Res., 45, 438-444.

Yu, Z. Q., Chow, P. S. & Tan, R. B. H., (2006b), Seeding and constant-supersaturation control by ATR-FTIR in anti-solvent crystallization, Org. process Res. Dev, 10, 717-722.

Zhang, Y., (1996), A survey on evaluation methods for image segmentation. Pattern Recognition, 29, 1335-1346.

Zhang, Y., (2006), A summary of recent progress for segmentation evaluation. Advances in Image and Video Segmentation. ISBN: 1-59140-753-2, 423-440.

Zhou, Y., Doan, X.T. & Srinivasan R., (2007), On-line monitoring of particle shape and size distribution in crystallization processes through image analysis. 17th European Symposium on Computer Aided Process Engineering, ESCAPE 17, T2-504.

Zhou, Y., Srinivasan, R. & Lakshminarayanan, S., (2009), Critical evaluation of imaging based techniques for real-time crystal size measurements. Computers & Chemical Engineering, 33, 1022-1035.

Zuiderveld, K., (1994), Contrast limited adaptive histogram equalization. Chapter VIII.5, Graphics Gems IV. P.S. Heckbert (Eds.), Cambridge, MA, Academic Press, 1994, pp.474-485.

Appendix A List of Publications

Zhou, Y., Srinivasan, R. & Lakshminarayanan, S., (2009), Critical evaluation of imaging based techniques for real-time crystal size measurements. Computers & Chemical Engineering, 33, 1022-1035

Sarkar, D., Doan, X. T., **Zhou, Y**. & Srinivasan, R., (2009), In-situ particle size estimation for crystallization processes by multivariate image analysis. Chemical Engineering Science, 64, 9-19.

Zhou, Y., Lakshminarayanan, S. & Srinivasan, R., Optimization of image processing parameters for large sets of in-process video microscopy images acquired from batch crystallization processes: combination of uniform design and simplex search. Chemometrics and Intelligent Laboratory Systems. Accepted.

Zhou, Y., Srinivasan, R. & Lakshminarayanan, S., In situ particle size estimation by fusing multiple image-based techniques. In preparation.

Zhou, Y., Doan, X. T. & Srinivasan, R., Real-time imaging and product quality characterization for control of particulate processes. Joint 16th ESCAPE and 9th PSE: Computer-Aided Chemical Engineering 21A, W. Marquardt and C. Pantelides (Eds), 775-780. Elsevier, Garmish-Partenkirchen, 2006.

Doan, X. T., **Zhou, Y.** & Srinivasan, R., Integrating multi-variate image analysis and artificial intelligence techniques with PVM for in-line crystal size and shape measurements. AIChE Annual Meeting, San Francisco, 301aa, Nov., 2006.

Zhou, Y., Doan, X. T. & Srinivasan, R., On-Line Monitoring of Particle Shape and Size Distribution in Crystallization Processes through Image Analysis. T2-504, ESCAPE, Bucharest, Romania, 2007.

Zhou, Y., Srinivasan, R. & Lakshminarayanan, S., Quantitative large-scale validation of image-based sensors for online particle size characterization during crystallization. AIChE Annual Meeting, Philadelphia, PA, 16-21 Nov., 2008.

Zhou, Y., Lakshminarayanan, S. & Srinivasan, R., Particle size distribution estimation through image-based sensors: sequential simplex optimization for selection of optimal parameters. AIChE Annual Meeting, 83i, Nashville, TN, 8-13 Nov., 2009.

Sarkar, D., **Zhou Y.**, Lakshminarayan, S. & Srinivasan, R., Validation of a population balance model of a batch crystallization process using particle size distributions from image-based sensors. ESCAPE 19, 2009.

Zhou, Y., Srinivasan, R. & Lakshminarayanan, S., Image-based approach for real-time particle size estimation. PSE ASIA 2010, P160, Singapore, 25-28 July, 2010.

Zhou, Y., Srinivasan, R. & Lakshminarayanan, S., Estimate particle size distribution by image-based sensors: integrating multiple image segmentation. 7th European Congress of Chemical Engineering 7 & 19th International Congress of Chemical and Process Engineering CHISA 2010, P5. 136, pp 1180, 28 August – 1 September 2010, Prague, Czech Republic.

Zhou, Y., Srinivasan, R. & Lakshminarayanan, S., Real-time particle size estimation by image-based methods: integrating multiple image segmentations.

Particulate Process in the Pharmaceutical Industry III. Engineering Conferences International. Gold Coast, Australia, 24-29 July 2011. Accepted.